

**MICRODROPLETS: CHEMISTRY, APPLICATIONS AND  
MANIUPULATION USING IONIZATION SOURCES AND MASS  
SPECTROMETRY**

by

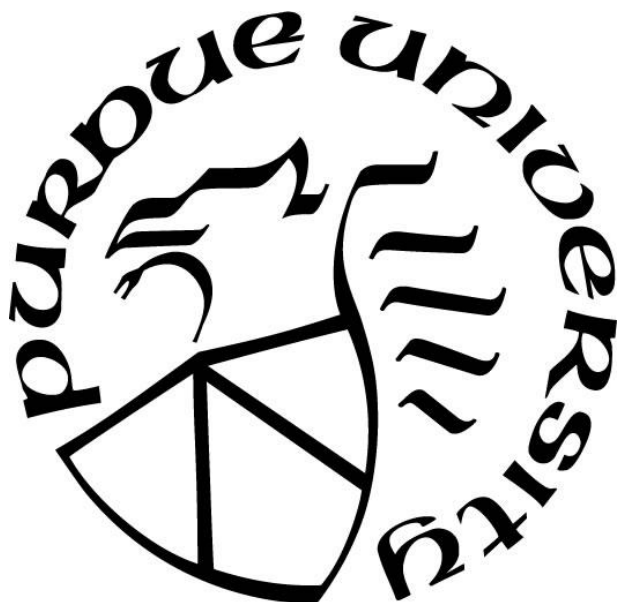
**Kiran Iyer**

**A Dissertation**

*Submitted to the Faculty of Purdue University*

*In Partial Fulfillment of the Requirements for the degree of*

**Doctor of Philosophy**



Department of Chemistry

West Lafayette, Indiana

December 2019

**THE PURDUE UNIVERSITY GRADUATE SCHOOL  
STATEMENT OF COMMITTEE APPROVAL**

**Dr. R. Graham Cooks, Chair**

Department of Chemistry

**Dr. David H. Thompson**

Department of Chemistry

**Dr. Hilikka I Kenttämää**

Department of Chemistry

**Dr. Julia Laskin**

Department of Chemistry

**Approved by:**

Dr. Christine Hrycyna

*Dedicated to everyone who has made me a better scientist and a better person*

## ACKNOWLEDGMENTS

The work presented in this dissertation is a testament to the exponential value of hard work, a supportive work environment, family and friends. Firstly, I am incredibly grateful to my family for their constant support and encouragement. The value of hard work and resilience was instilled in me at a very young age by my parents, Shobha and Raju and these are values I continue to uphold even today. I am incredibly grateful to Ashok, who has been my biggest cheerleader through the entire process of graduate school and in life. I am also indebted to my brother Vivek for his constant support.

Graduate school is not an easy process. Thank you to my lifelong friends Nidhi Jacob, Vinod Vasudevan and Akhil Sanjay Rao for believing that I could follow through with my decision to come to graduate school. This journey would not be the same without the friendships I made along the way. To Emily Haynes, Keelan Trull and Jonathan Fine – thank you for being my sounding board and my pillars in graduate school.

I would like to thank my research advisor R. Graham Cooks, for not only providing me with an opportunity to work in Aston Labs, but also being an excellent mentor and guide. I have learnt a lot under his tutelage, and I am forever grateful.

I owe a great deal to the numerous collaborators that I have had the opportunity to work with at AbbVie Inc, specifically Nari Talaty and Andrew Bogdan and at Agilent Technologies Inc., specifically Shane Tichy.

I am extremely lucky to have developed close ties to many people at Aston Labs. I am grateful to Michael Wleklinski for all the initial training and teachings. A big thank you Adam Hollerbach, Ryan Bain, Patrick Fedick, Christopher Pulliam, Harrison S.Ewan and Brett M. Marsh who have contributed greatly to my research. I would also like to thank Dalton Snyder, Robert Schrader, Lucas Szalwinski, David Logsdon, Yangjie Li, Zhuoer Xie and Grace O. Capek.

A big thank you to Brandy McMasters for her incredible help that has been extremely valuable to me.

I would also like to thank my committee members Professor David H. Thompson, Professor Hilka I Kenttämä and Professor Julia Laskin for all the help and guidance they have provided me throughout this process.

## TABLE OF CONTENTS

LIST OF TABLES .....	9
LIST OF FIGURES .....	10
ABSTRACT .....	14
CHAPTER 1. INTRODUCTION .....	15
1.1 Overview .....	15
1.2 Electrospray ionization .....	15
1.2.1 History and fundamentals .....	15
1.3 Desorption electrospray ionization (DESI).....	17
1.4 Reaction acceleration in microdroplets.....	17
1.5 Manipulation of microdroplets and ions in air.....	18
CHAPTER 2. MULTISTEP FLOW SYNTHESIS OF DIAZEPAM GUIDED BY DROPLET- ACCELERATED REACTION SCREENING WITH MECHANISTIC INSIGHTS FROM RAPID MASS SPECTROMETRY ANALYSIS .....	20
2.1 Introduction.....	20
2.2 Experimental.....	21
2.2.1 Reagents.....	21
2.2.2 NMR analysis .....	21
analyzed using a Bruker AV-III-500-HD NMR spectrometer. ....	22
2.2.3 Mass spectrometry.....	22
2.2.4 Quantitative MS analysis.....	22
2.2.5 ESI experiments.....	22
2.2.6 Leidenfrost experiments .....	22
2.2.7 Microfluidic experiments.....	23
2.2.8 Microfluidic synthesis of N-(2-Benzoyl-4-chlorophenyl)-2-halo-N-methylacetamide (3) .....	23
2.2.9 Microfluidic synthesis of Diazepam (4) from N-(2-Benzoyl-4-chlorophenyl)- 2- chloro-N-methylacetamide (3A).....	23
2.2.10 Microfluidic synthesis of Diazepam (4) from 5-Halo-2-(methylamino)- benzophenone (1).....	24

2.2.11 Batch Synthesis of N-(2-Benzoyl-4-chlorophenyl)-2-chloro-N-methylacetamide (3A).	24
2.3 Results and Discussion	25
2.3.1 N-Acylation reaction screen	25
2.3.2 Cyclization reaction screen	27
2.3.3 Continuous diazepam synthesis	30
2.4 Conclusions	33
CHAPTER 3. ACCELERATED MULTI-REAGENT COPPER CATALYZED COUPLING REACTIONS IN MICRODROPLETS AND THIN FILMS	34
3.1 Introduction	34
3.1.1 Reagents	35
3.1.2 Electrospray experiments	35
3.1.3 Paper spray experiments coupled with atmospheric pressure chemical ionization (APCI)	36
3.1.4 ESI experiments for offline collection (C-O coupling)	36
3.1.5 ESI experiments for offline collection (C-N coupling)	37
3.1.6 Bulk/batch experiments	37
3.2 Results and Discussion	38
3.2.1 C-O coupling	38
3.2.2 C-N coupling	40
3.3 Conclusions	44
CHAPTER 4. REACTION ACCELERATION IN ELECTROSPRAY DROPLETS: SIZE, DISTANCE AND SURFACTANT EFFECTS	45
4.1 Introduction	45
4.2 Experimental	46
4.2.1 Microscopy	46
4.2.2 Nanospray measurements of reaction acceleration	47
4.3 Results and Discussion	48
4.3.1 Microscopy-distance experiments	48
4.3.2 Microscopy – surfactant experiments	48
4.3.3 Effect of Tip Size, Concentration, and Surfactants on Reaction Acceleration	49

4.4	Applications of ambient focusing in reaction acceleration.....	60
4.5	Conclusions.....	61
CHAPTER 5. SCREENING OF THE SUZUKI CROSS-COUPLING REACTION USING DESORPTION ELECTROSPRAY IONIZATION IN HIGH-THROUGHPUT AND IN LEIDENFROST DROPLET EXPERIMENTS .....		62
5.1	Introduction.....	62
5.2	Experimental.....	67
5.2.1	Chemicals .....	67
5.2.2	Plate preparation for DESI-MS imaging .....	67
5.2.3	DESI-MS screening.....	67
5.2.4	Leidenfrost droplets.....	68
5.2.5	Mass spectrometry.....	69
5.2.6	Results and discussion.....	69
5.3	Conclusions.....	79
CHAPTER 6. ION MANIPULATION IN AIR USING 3D-PRINTED ELECTRODES.....		81
6.1	Introduction.....	81
6.2	Experimental.....	82
6.2.1	Focusing electrode designs .....	82
6.2.2	3D-printing .....	83
6.2.3	IonCCD current measurements.....	84
6.2.4	SIMION simulations.....	84
6.2.5	Mass spectrometry.....	85
6.3	Results and discussion .....	85
6.3.1	Conic section electrodes .....	85
6.3.2	Aperture electrodes.....	88
6.3.3	Complex electrodes .....	90
6.3.4	SIMION simulations.....	92
6.3.4.1	Conical section electrodes.....	92
6.3.4.2	Apertures.....	93
6.3.4.3	Complex electrodes.....	94
6.3.5	Rationalization of results: Focusing mechanism .....	95

6.4	Conclusions.....	98
CHAPTER 7.	Future directions .....	99
7.1	Relating droplet size to reaction acceleration .....	99
7.2	Ion manipulation in air.....	100
REFERENCES	.....	101
VITA.....	.....	111
PUBLICATIONS.....	.....	112

## LIST OF TABLES

Table 2.1 Acceleration factors for the n-acylation reaction in the synthesis of diazepam .....	29
Table 3.1 Systems explored for the C-N coupling reaction between 3-iodopyridine and methanesulfonamide .....	42
Table 3.2 Substrate scope – relative abundance (R.A) yields of different substrates used for C-O and C-N coupling using 3-iodopyridine .....	44
Table 4.1 Concentration effects on conversion ratio of various phenylhydrazine + isatin solutions .....	52
Table 4.2 Bulk reaction of phenylhydrazine (100 mM) + Isatin (3 mM) with and without surfactant. Note the lower initial and final conversion ratios for the reaction with surfactant.....	53
Table 5.1 Acceleration Factors for Different Substrates Reacting with 4-Hydroxyphenylboronic Acid in Leidenfrost Droplets .....	74
Table 5.2 Product to reagent ratios for the Leidenfrost system (two and 10-minute time points), bulk - room temperature and refluxed and the DESI-MS system.....	76
Table 5.3 Approximate acceleration factors for different substrates reacting with 4-hydroxyphenylboronic acid in DESI-MS microdroplets <sup>a</sup> .....	79

## LIST OF FIGURES

Figure 1.1 Depiction of the process of electrospray ionization (ESI).....	16
Figure 2.1 <sup>1</sup> H NMR of N-(2-benzoyl-4-chlorophenyl)-2-chloro-N-methylacetamide .....	25
Figure 2.2 N-Acylation screen. Synthesis of <b>3</b> using bromoacetyl chloride – comparison of spray and flow in toluene and acetonitrile.....	27
Figure 2.3 Methylene proton <sup>1</sup> H NMR signals of the S <sub>N</sub> 2 and N-acylation product mixture. ....	28
Figure 2.4 <sup>1</sup> H NMR of [7].....	29
Figure 2.5 <sup>13</sup> C NMR of [7].....	30
Figure 2.6 Cyclization reaction screen. Synthesis of diazepam, comparing ACN (left) and toluene (right) solvents in spray, Leidenfrost, and flow reactions using bromoacetyl chloride.....	31
Figure 2.7 Reactor schematic for continuous diazepam synthesis. ....	32
Figure 3.1 Apparatus for (a) electrospray, (b) paper spray and (c) scale up (C-O coupling only).....	37
Figure 3.2 Mass spectra for C-O coupling (a) and C-N coupling (b) – comparison of bulk/batch mode (2 min), electrospray (2 min) and paper spray (2 min) .....	39
Figure 3.3 MS/MS spectra for ions corresponding to <i>m/z</i> 124 .....	40
Figure 3.4 MS/MS spectra for ions corresponding to <i>m/z</i> 173 .....	40
Figure 3.5 <sup>1</sup> H NMR of the C-O coupling product (using ethanol as the reagent) – offline collection using ES .....	41
Figure 3.6 High-resolution MS of the bulk reaction using ethanesulfonamide as the starting reagent showing the radical cation of the pyridylsulfonamide as the major reaction product .....	43
Figure 3.7 <sup>1</sup> H NMR of C-N coupling product – offline collection using ES. Solvent: Methanol-d <sub>4</sub> .....	43
Figure 4.1 Super resolution microscopy images of 100 μM Rhodamine B in 9:1 methanol:glycerol droplets produced by nESI at distances (a) 9 mm and (b) 3 mm. Corresponding diameter distributions for (c) 9 mm and (d) 3 mm are also shown.....	49
Figure 4.2 Effect of surfactant on droplet size distribution of a solution containing 100 μM Rhodamine B in 9:1 methanol:glycerol and (a) no surfactant, (b) 0.1 mM surfactant, (c) 1 mM surfactant, and (d) 10 mM surfactant. All experiments were performed using a 20-ms pulse duration and 20-μm nESI tip placed at a distance of 5 mm from the ITO coverslip .....	50

Figure 4.3 (a) Representative mass spectrum of phenylhydrazine+isatin reaction mixture shown at distances of 1 cm and 5 cm. Effect of (b) tip size (see legend) (c) 10, 50, and 100 mM phenylhydrazine concentrations (shown in legend) with constant isatin concentration and (d) different surfactant concentration (shown in legend) on conversion ratio as a function of emitter to MS distance. Note that the data in panels (b) and (c) were recorded with a 5- $\mu$ m emitter. Isatin concentration was 3 mM in all measurements here. Methanol was the solvent..... 51

Figure 4.4 (a) Model of droplet with surface (dark blue) and bulk (light blue) volumes and differing surface and bulk concentrations (molecules represented by orange circles). (b) Relationship between droplet diameter and surface to bulk concentration ratio for a constant concentration of 100 mM solute. Droplet drawings show how volume and concentrations change with diameter. (c) Calculated droplet diameter as a function of droplet flight time. (d) Surface to volume ratio as a function of droplet flight time for different droplet sizes. (e) Surface to bulk concentration ratio for different solute concentrations in a 500-nm diameter droplet. Droplet drawings show the effect of solute concentrations schematically ..... 57

Figure 4.5 (a) Evolution of surface area with droplet fission event. The surface area at droplet creation is 1. (b) Fission event as a function of droplet flight time for 19 mN/m and 22 mN/m surface tensions ..... 59

Figure 5.1 Photograph of the desorption electrospray ionization (DESI) setup ..... 65

Figure 5.2 Plate layout for methyl orange and reaction mixtures (right). Biomap images of methyl orange ( $m/z$  304) array showing the reproducibility of the pinning tool (left). Plates are 127  $\times$  85 mm ..... 70

Figure 5.3 Leidenfrost apparatus ..... 70

Figure 5.4 Reagent layout on the final reaction plate for the Suzuki reaction (right). Each pair of rows contains a different set of starting reagents in replicates. Rows A and B correspond to wells containing 3-bromopyridine (1a), rows C and D contain 3-iodopyridine (1b), rows E and F contain 3-chloropyridine (1c), rows G and H contain 3-bromoquinolin (6a), rows I and J contain 3-iodoquinoline (6b), rows K and L contain 3-chloroquinoline (6c), rows M and N contain 3-bromo-5-methylpyridine (4a), and rows O and P contain 3-bromo-2,6-dimethylpyridine (4b). White squares contain methyl orange as the positional marker. All reaction wells contain reagent 4-hydroxyphenylboronic acid (2) and catalyst but differ in the bases added. Columns 1–6 contain DBU, columns 7–12 contain EtOK, columns 15–18 contain EtONa and columns 19–24 have no base. DESI imaging heat map of the reaction plate for various products (left)—4-(pyridin-3-yl)phenol (3) at  $m/z$  170 (rows A–F), 4-(quinolin-3-yl)phenol (7) at  $m/z$  220 (rows G–L), 4-(5-methylpyridin-3-yl)phenol (5a) at  $m/z$  184 (rows M–N), and 4-(2,6-dimethylpyridin-3-yl)phenol (5b) at  $m/z$  198 (rows O–P). Each product was individually searched by the product  $m/z$  and then the data were overlaid onto a single figure ..... 71

Figure 5.5 Mass spectra for the Suzuki cross-coupling reaction between 3-bromopyridine (**15**) with 4-hydroxyphenylboronic acid (**18**) from the DESI-MS experiment (left). Mass spectra for the Suzuki cross-coupling reaction between 3-bromopyridine (**15**) with 4-hydroxyphenylboronic acid (**18**) from the Leidenfrost experiment (right). Blue: mass spectrum of the reaction using EtOK as the base. Red: mass spectrum of the reaction using EtONa as the base. Green: mass spectrum of the reaction using DBU as the base. Purple: mass spectrum of the reaction without any base added. The “-Et” label in the mass spectra refers to ethoxylated peaks..... 72

Figure 5.6 MS/MS confirmation of 4-(pyridin-3-yl)phenol (**19**)..... 73

Figure 6.1 (A) Conic section electrodes (50 mm long) in cylindrical, conical and ellipsoidal geometries. (B) Cylindrical electrode showing the holes on the side spaced 5 mm apart and having diameters of ~ 1 mm to allow for the placement of a nanoelectrospray emitter. (C, D, E) Curved, chicane, and straight complex electrodes (openings here are 20 mm). ..... 83

Figure 6.2 Ellipsoidal electrode setup. Note that a flashlight is used to illuminate the holes on the outside of the electrode. .... 86

Figure 6.3 Cross sectional beam images recorded with an IonCCD camera for the conical (A), cylindrical (B), and ellipsoidal (C) focusing electrodes. nESI sprayer was held at 4.5 kV while the focusing electrode was held at 3kV. (D) Ion beam cross section at 5 mm for each electrode. (E) Summary of focusing data for each electrode and emitter distance recorded in these experiments. .... 87

Figure 6.4 (A) Mass spectra showing profiles of a mixture of TAA salts. Top blue – Mass spectrum of the sample at 2 inches. Bottom red – Mass spectrum of the sample at 60 cm.(B) Mass spectra showing profiles of a mixture of TAA salts using focusing electrodes (Hole 1) at a distance of 60 cm. Top blue ellipsoidal, middle red – conical, bottom green – cylindrical. The nESI emitter is held at 3 kV while the focusing electrodes were held at 2 kV ..... 89

Figure 6.5 Mass spectra showing profiles of a mixture of TAA salts using focusing electrodes (Hole 1, nearest to the exit of the electrode) which is at a distance of 24 inches from the MS. Top blue – ellipsoidal, middle red – conical, bottom green – cylindrical. The nESI emitter is held at 4 kV while the focusing electrodes were held at 2 kV ..... 90

Figure 6.6 Non-conductive apertures: (A). IonCCD Intensity of nESI plume. (B-E) - Ion CCD images of beam focus through 15 mm (B), 12 mm (C), 9 mm (D) and 3 mm (E) apertures. Note the differing color and axes scales for each figure. .... 91

Figure 6.7 Summary of all conductive aperture ion beam data obtained from IonCCD images. For representative IonCCD images, see figure S3. .... 92

Figure 6.8 IonCCD images of ion beam focus through (Left) curved complex electrode, (Middle) chicane complex electrode, and (Top) straight complex electrode. Top images correspond to initial float voltage of 3 kV, while bottom corresponds to initial float voltage of 4 kV. .... 93

Figure 6.9 Additional SIMION simulation traces. Top: Cone (3 kV) potential, 25 mm emitter position SIMION trace. Middle: cone (3 kV) 5 mm emitter position SIMION trace. Bottom: Aperture (1.5 kV) with emitter (2 kV) SIMION trace. Parameters used for ion generation are as described in the experimental section. .... 94

Figure 6.10 A. Profiles of simulations of an ion packet focus through a 15 mm aperture held at the indicated voltages using an emitter voltage of 2 kV. B. Simulations of ion packet focus through a 15 mm aperture held at 1 kV with the emitter held at the indicated voltage. .... 95

Figure 6.11 SIMION ion trajectories through (A) curved, (B) chicane, and (C). straight versions of complex electrodes. (D-E) profiles of the ion distributions for each electrode geometry, (E) shows up close distributions of the curved and chicane electrodes. In all cases, ions are generated from the left and move towards the right through the electrodes ..... 96

Figure 6.12 0 V (left), 2500 V (middle), and 5000 V (right) initial ion energy trajectories..... 97

Figure 6.13 Simulations of ions traveling through the curved electrode in the presence of atmospheric gas (left) and in vacuum (right). The direction of ion travel is from the bottom right opening of the electrodes. Note that ions are not transmitted to the exit when collisions are not present. .... 98

## ABSTRACT

There is widespread use of ionization sources (ambient and non-ambient) for a variety of applications. More recently, charged microdroplets generated by electrospray ionization and paper spray have been used to conduct chemistry at faster rates compared to bulk volumes. Uncharged droplets such as those generated by the Leidenfrost technique have also been used to explore chemistry and study the degradation of drugs in an accelerated manner. These microdroplets serve as reaction vessels in which in which some reactions are known to occur at accelerated rates. Such chemistry can be particularly useful in pharmaceutical settings to rapidly synthesize small amounts of materials in relatively short amount of time. Additionally, microdroplets may also be used to perform high throughput screening analysis. While several parameters influencing the rate of reaction in microdroplets have been explored (such as spray distance and reagent concentration), the mechanism of reaction acceleration has not been probed to a significant extent. A major portion of my dissertation describes the use of charged and uncharged microdroplets to perform quick chemistry, guide microfluidic synthesis of drugs such as diazepam, perform scale up of copper catalyzed C-O and C-N coupling reactions and screen reaction conditions for pharmaceutically relevant reactions such as the Suzuki cross-coupling reaction. Additionally, work discussed here also describes development and use of existing techniques such as structured illumination microscopy to measure droplet sizes, explore the role of distances on droplet size, and study the effect of surfactants on the rate of reactions in microdroplets generated by nano-electrospray ionization. A mathematical model to understand the mechanism of increased reaction rates in microdroplets has also been presented. Additionally, this dissertation also describes ways to manipulate ions in air using various designs of 3D-printed electrodes that operate with DC potentials only and which can be easily coupled with nano-electrospray ionization sources to transmit ions over long distances.

# CHAPTER 1. INTRODUCTION

## 1.1 Overview

There has been a widespread use of ionization sources for a variety of applications.<sup>1-4</sup> While ionization sources (ambient and non-ambient) assist in generating microdroplets and eventually bare ions, they can also be exploited to study chemical reactions.<sup>5</sup> A myriad of techniques utilizing mass spectrometry (MS) and microdroplets has been used in the recent past to study chemical reactions in droplets, explore reactivity, assist in route planning, reagent selection and high throughput screening. Most of these techniques utilize electrospray ionization (ESI) to generate microdroplets in which chemistry can be explored. While many reactions have been studied and reaction acceleration for these reactions has been demonstrated in microdroplets, mechanistic studies are still underway to completely understand the nature of these droplets. Various factors are at play and can influence the rate of product formation in confined volumes. Droplet size, reagent concentration, the presence of a surfactant and the operating distance between the ionization source and the instrument, can all affect reaction acceleration. Additionally, there are several different methods to generate droplets and “confined volumes” or compartments to enhance product formation for various chemical reactions with different factors influencing product formation.<sup>6,7</sup> Some of these systems include Leidenfrost droplets<sup>8</sup> and thin films generated by drop casting.<sup>9</sup>

## 1.2 Electrospray ionization

### 1.2.1 History and fundamentals

Electrospray ionization (ESI) is a soft ionization technique developed by John Fenn and coworkers at Yale University.<sup>10, 11</sup> The researchers showed that ESI-MS could be used to ionize large biomolecules with little fragmentation.<sup>12</sup> Additionally, they demonstrated easy coupling of the ESI-MS interface with liquid chromatography (LC) making ESI-MS usage ubiquitous.<sup>13</sup> Traditionally, ESI is performed using a sharp emitter (e.g. fused silica) containing the analyte solution to which DC potentials are applied. The resultant high potential causes the formation of a Taylor cone due to ion formation, charge separation and eventual repulsion. The charged microdroplets formed from the Taylor cone eventually undergo Coulombic fission and evaporation

to produce dry or bare ions. This happens when the repulsive forces in the droplet overcome the surface tension of the droplet, known as the Rayleigh limit.<sup>14</sup> An illustration depicting the process of ESI is shown in Figure 1.1. There are two main schools of thought to explain the mechanism of ion formation from droplets.<sup>15</sup> The first model, the ion evaporation model (IEM) states that initial droplets formed from the emitter undergo Coulombic fission to generate progeny droplets and lightly solvated ions. The progeny droplets then undergo evaporation to produce bare ions. The second model, the charge residue model (CRM) explains the formation of ions from larger molecules such as proteins. Briefly, the model states that droplet evaporation leaves charges behind which are then transferred to the analyte to form an ion. Recently, a third model, the chain elongation model (CEM) has been proposed to explain the behavior of elongated chains such as polymers.<sup>16, 17</sup> The model proposes that part of a chain escape the droplet surface and moves into the gas phase with some charge. Eventually the rest of the chain escapes from the droplet.

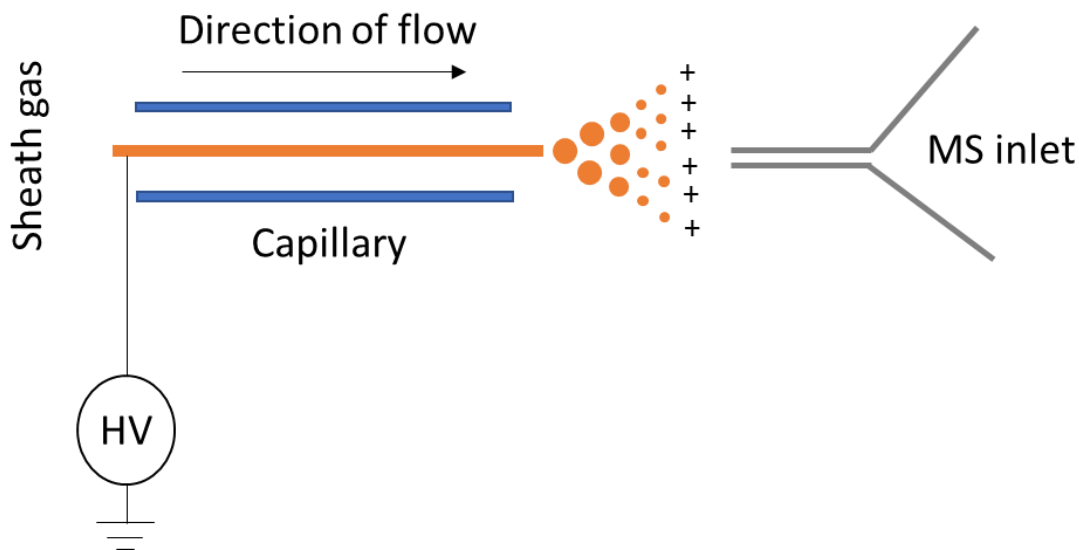


Figure 1.1 Depiction of the process of electro-spray ionization (ESI)

Ionization efficiency is an important factor to consider when using ESI. The ability to form bare ions or gas phase ions from charged microdroplets is called ionization efficiency and greatly depends on the nature of the solvent used. It is important that the high voltages used in ionization experiments be enough to overcome the high surface tensions of the solvent being used for the experiment. Initial designs of ESI emitters involved approximately 200  $\mu\text{m}$  wide blades made of

stainless steel.<sup>10</sup> Further optimization of these designs was made by Mann *et.al*<sup>18</sup> with the use of glass capillaries of much smaller diameters (1-5  $\mu\text{m}$ ) as emitters. This technique widely used today is called nano-electrospray ionization (nESI). nESI uses much lower sample volumes compared to traditional ESI methods. nESI also eliminates the use of a heated sheath gas to assist desolvation and operates at flow rates of about 20 nL/min. In addition to nESI, there are a variety of ionization sources, some of which are considered ambient ionization techniques, since the ionization occurs at atmospheric pressure and temperature and or no sample preparation required. Some of the more popular ambient ionization sources include desorption electrospray ionization (DESI),<sup>1</sup> and direct analysis in real time (DART).<sup>19</sup> Some other variants of ambient ionization techniques include paper spray (PS),<sup>20</sup> extractive and electrospray ionization (EESI).<sup>21</sup> PS utilizes a paper substrate that is cut to a sharp tip, to which voltage (3-5 kV) is applied. The applied voltage creates an electrospray plume from the tip of the paper.

### **1.3 Desorption electrospray ionization (DESI)**

DESI, one of the first ambient ionization mass spectrometric techniques was developed in 2004.<sup>1</sup> DESI uses a primary ESI plume which generates primary droplets which are directed to a surface from which the analyte is desorbed, creating secondary droplets which then enter the MS for analysis. DESI has been shown to be extremely useful as a surgical assessment tool to rapidly analyze cancerous tissue samples and improve patient outcomes. More recently, DESI-MS has been used as a screening tool<sup>22</sup> to screen reaction mixtures and well at rates that approach  $10^4$  reactions per hour. The use of DESI-MS as a high throughput method utilizes automated liquid handling systems, robotic pin tools and in-house software that is capable of generating a reactivity heat map to guide synthesis and structural confirmation.

### **1.4 Reaction acceleration in microdroplets**

A variety of spray based ionization techniques have been used to create microdroplets which act as vessels in which it is possible to perform accelerated chemical reactions.<sup>6, 7, 23, 24</sup> The inspiration to perform chemical reactions in confined volumes can be drawn from the chemistry of life itself, which occurs in spatially limited volumes such as cells. Similarly, a variety of chemical reactions

are also reported to widely occur at the air-water interface e.g. aerosols.<sup>25, 26</sup> There have been several studies that report the use of confined volumes and interfaces to perform such chemistry. In 2006, the Eberlin transacetalization reaction was performed in electrospray generated droplets.<sup>27</sup> Although the yield was modest, there was evidence of increased reaction rates in microdroplets when compared to their bulk counterparts. Early work (2011) using DESI to generate microdroplets has shown to increase the rate of hydrazone formation when Girard's reagent T was sprayed on a surface containing cortisone.<sup>5</sup> Work done by Muller *et al.*<sup>6</sup> shows the use of an ESI variant (operated in online and offline modes) to demonstrate the acceleration of the Claisen-Schmidt condensation reaction. In the offline experiment, the researchers used a modified ESI setup involving the multiplexing of four electrospray sources that was used to spray the reaction mixture onto glass wool. This setup enabled scale-up and milligrams of product could be collected. Subsequent work done by various researchers have shown that a variety of organic reactions and biomolecule synthesis can be accelerated in microdroplets.

The increase in reaction rates have been attributed to a variety of factors such as decreasing droplet size with distance, interfacial effects, changes in local concentration and pH. Over time, a variety of techniques have been used to generate confined volumes or microdroplets and confined volumes such as levitated droplets,<sup>8</sup> thin film formation,<sup>9</sup> biphasic systems<sup>23</sup> and other spray based techniques.<sup>28</sup> Additionally, work is also being done tangentially to understand the mechanism of reaction acceleration in droplets. Studies to understand mechanisms have been targeted to measuring droplet sizes,<sup>29-31</sup> understanding factors that can affect droplet size and finding ways to manipulate them,<sup>32</sup> reagent distribution on surfaces and understanding the role of the interface in reaction acceleration.<sup>31, 33, 34</sup>

## **1.5 Manipulation of microdroplets and ions in air**

Once microdroplets are formed from electrospray sources, they undergo evaporation to produce bare ions.<sup>11</sup> While these ions are generated at atmospheric pressure, they propagate to the vacuum region of the mass spectrometer where most of the focusing and analysis occurs. The collection efficiency of most mass spectrometric instruments is <0.1%.<sup>35, 36</sup> This is mainly due to the dispersed nature of the electrospray plume and the small sampling orifices in most instruments. Additionally, increased distances are needed for effective desolvation of microdroplets to produce

“dry” ions or these sources must be accompanied by a heated sheath gas. While ion funnels may assist in solving this problem, they operate under pressures of 0.1 to 30 torr and often require complex RF voltages to function.<sup>36</sup> While vacuum conditions in the mass spectrometer allow for minimum collisions with background gas molecules, the need for pumps and vacuum equipment places an obstacle to the development of newer instruments especially miniaturized mass spectrometers.<sup>37</sup> So far, little has been done to create avenues to manipulate ions in air to improve transmission to the MS. Researchers, including the Cooks’ lab have reported the use of several devices such as apertures and plastic devices to focus ions.<sup>38,39</sup> The focusing effects can be as large as 10x when combined with nanospray emitters. 3D-printing techniques have also been used to rapidly prototype various devices such as rings and bent electrodes to focus ions into spots.<sup>38</sup>

## CHAPTER 2. MULTISTEP FLOW SYNTHESIS OF DIAZEPAM GUIDED BY DROPLET-ACCELERATED REACTION SCREENING WITH MECHANISTIC INSIGHTS FROM RAPID MASS SPECTROMETRY ANALYSIS

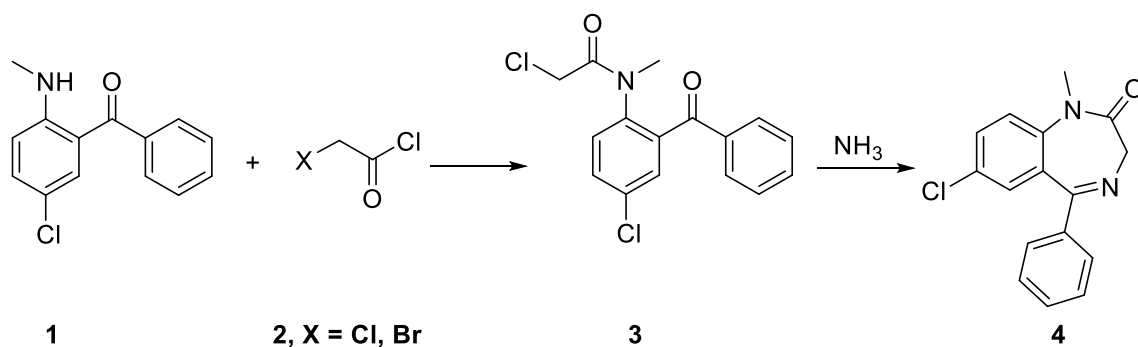
Portions of this chapter have been published in the journals: European Journal of Organic Chemistry and Organic Process Research and Development as the following articles:

1. Wleklinski, M., Falcone, C. E., Loren, B. P., Jaman, Z., Iyer, K., Ewan, H. S., Hyun, S.-H., Thompson, D. H. and Cooks, R. G. (2016), Can Accelerated Reactions in Droplets Guide Chemistry at Scale? *Eur. J. Org. Chem.*, 2016: 5480–5484.
2. Iyer, K.†, Ewan, H.S,† Hyun, S.-H, Wleklinski, M., Cooks, R. G., Thompson, D. H.(2017), Multistep Flow Synthesis of Diazepam Guided by Droplet-Accelerated Reaction Screening with Mechanistic Insights from Rapid Mass Spectrometry Analysis. *Org. Process Res. Dev.* 2017, 21, 1566-1570

### 2.1 Introduction

The potential for the efficient synthesis of active pharmaceutical ingredients (APIs) through continuous flow chemistry continues to draw interest from a broad range of disciplines throughout academia and industry<sup>40-44</sup>. Mass spectrometry (MS) has proven to be a useful tool in reaction monitoring (kinetics and outcome).<sup>45</sup> MS also helps in identifying reactive intermediates and hence in understanding the mechanistic details of a chemical reaction<sup>46</sup>. Additionally, MS can be used to study chemical reactions in droplets.<sup>47</sup> Previous studies have shown that several chemical reactions are accelerated in microdroplets formed by electrospray ionization (ESI) relative to corresponding bulk reactions.<sup>33, 48</sup> This acceleration is due, in part, to solvent evaporation and its effect on reagent concentration at the interface.<sup>49</sup> This rapid method of reaction screening can be useful in guiding microfluidic reactions and in scale up. An alternative way of generating microdroplets for studying chemical reactions is by employing the Leidenfrost effect. This effect occurs when a solution is dropped onto a heated surface such as a glass petri dish which is held at a temperature higher than the boiling point of the solvent used. As the droplet approaches the heated surface, the solvent layer at the bottom begins to evaporate, and a layer of insulating vapor is formed around the droplet. This prevents rapid evaporation of the solvent and causes the droplet to levitate.<sup>50</sup> Although the droplets that are formed by this technique are larger than ESI droplets, they have some of the same properties; therefore, reactions in these droplets can also be a useful tool in guiding microfluidic transformations. In the present study, we use the synthesis of diazepam (Scheme 2.1) as a model

system to showcase how the droplet screening demonstrated by Wleklinski et al.<sup>51</sup> guided the continuous synthesis of diazepam. Since a key step in this pathway involves N-acylation, these observations may have a more general bearing on N-acylation reactions and in the synthesis of common bioactive molecules<sup>52</sup>. Although microdroplet conditions do not always directly translate into microfluidic scale conditions, this method can serve as a rapid yes/no prediction tool for the likelihood of a productive microfluidic reaction. Flow chemistry systems, coupled with online monitoring by ESI-MS, enable rapid screening of reaction conditions with real-time feedback. Not only does this allow for facile and efficient synthesis of active pharmaceutical ingredients (APIs), but it also brings an opportunity for new insights into reaction pathways and byproduct formation. Diazepam may be obtained in two synthetic steps, starting from the N-acylation reaction of 5-chloro-2-(methylamino)benzophenone **1** with 2-haloacetyl chloride **2** giving amide **3**. Subsequent treatment with ammonia then results in cyclization, giving diazepam **4** (Scheme 2.1). For each reaction screened in droplets or examined in flow reaction systems, the outcome was immediately ascertained by ESI-MS analysis.



Scheme 2.1 Proposed pathway for the continuous synthesis of diazepam

## 2.2 Experimental

### 2.2.1 Reagents

Reagents were purchased from Sigma Aldrich and used without further purification

### 2.2.2 NMR analysis

NMR samples were prepared by microscale SiO<sub>2</sub> column chromatography. Samples were

analyzed using a Bruker AV-III-500-HD NMR spectrometer.

### **2.2.3 Mass spectrometry**

Mass spectral analysis was performed using an LTQ ion trap mass spectrometer (Thermo Fisher Scientific, San Jose, CA) with nano-ESI (nESI) emitters which were made using borosilicate glass pulled to a ca. 1-3  $\mu\text{m}$  diameter. A spray voltage of  $\pm 2.0$  kV voltage was used for all analyses. All product samples (spray, Leidenfrost, and flow reactions) were diluted 1:100 with ACN prior to analysis, unless otherwise noted. The distance between the nESI tip and the MS inlet was kept constant at ca. 1 mm.. Positive-ion mode was used for all chemical analyses, unless otherwise noted. Product ion (MS/MS) spectra were recorded using collision-induced dissociation (CID) with a normalized collision energy of 25 (manufacturer's unit).

### **2.2.4 Quantitative MS analysis**

An MS based calibration curve was made from mixtures of  $0$ ,  $1 \times 10^{-7}$ ,  $1 \times 10^{-6}$ ,  $2.5 \times 10^{-6}$ , and  $8 \times 10^{-6}$  M diazepam with  $3.88 \times 10^{-6}$  M diazepam-d<sub>3</sub>. Each measurement was performed in triplicate using nESI. Crude reaction samples were quantified by first diluting an appropriate amount ( $\times 10\ 000$  typically) and then adding the same amount of internal standard. Each crude sample was diluted in duplicate and analyzed by nESI.

### **2.2.5 ESI experiments**

Experiments were performed by spraying the reaction mixture directly onto glass wool using a home-built ESI source. Reagents **1** and **2** were premixed at concentrations of 100 mM and 200 mM, respectively, and loaded into a syringe and controlled using a syringe pump at 10  $\mu\text{L}/\text{min}$ . Nitrogen was used as the sheath gas at 100 psi and an external voltage of 5kV was applied to the emitter. The total spray time was 10 min. After 10 min, the glass wool was washed with ACN and the extracted residue was analyzed by nESI-MS. After MS analysis, the washed material was drawn back into the syringe and mixed with ammonia in methanol and then electrosprayed onto glass wool in a similar manner to synthesize diazepam.

### **2.2.6 Leidenfrost experiments**

Leidenfrost experiments were carried out on a hot plate with a heat setting of 540  $^{\circ}\text{C}$  (although the droplet temperature was much lower). Reagents **1** and **2** were premixed and loaded into a Pasteur pipet. The reaction mixture was then dropped onto a glass Petri dish that was placed on the hot

plate. The reaction mixture was added in aliquots over a time period of about two minutes, after which the mixture was collected from the surface using a Pasteur pipet and then analyzed by MS after diluting two-fold

### **2.2.7 Microfluidic experiments**

All microfluidic reactions were carried out using a Chemtrix Labtrix S1 system, equipped with 3223 or 3224 reactor chips.

### **2.2.8 Microfluidic synthesis of N-(2-Benzoyl-4-chlorophenyl)-2-halo-N-methylacetamide (3)**

Solutions 100 mM 5-halo-2- (methylamino)benzophenone (1 eq.) and 200mM haloacetylchloride (1 eq.) in toluene, ACN, DMF, or NMP were prepared. In the DMF reaction screen, 500 mM solutions were used; in the NMP reaction screens, 250 mM solutions of benzophenone and 500 mM (2 eq.) chloroacetyl chloride were used. A syringe was loaded with each of these two solutions and positioned on the first two inlets of a 10  $\mu$ L Labtrix 3223 chip. A third syringe was loaded with toluene and positioned on the third port of the same chip as a diluent. The reaction was flowed with 30, 60, and 180 s residence times at temperatures of 50, 100, and 150  $^{\circ}$ C. Samples were collected and immediately analyzed by nESI-MS (1  $\mu$ L of each sample was diluted with 99  $\mu$ L of ACN, then loaded into a glass electrospray tip for analysis). Samples were saved and stored at  $-20$   $^{\circ}$ C.

### **2.2.9 Microfluidic synthesis of Diazepam (4) from N-(2-Benzoyl-4-chlorophenyl)- 2-chloro-N-methylacetamide (3A).**

A 250 mM solution of N-(2-benzoyl-4-chlorophenyl)-2-chloro-N-methylacetamide (1 eq.) was prepared. Syringes were loaded with the prepared solution and with 7 N ammonia in methanol (7 eq.) and positioned on the first two inlets of a 10  $\mu$ L Labtrix 3223 chip. A third syringe was loaded with NMP and positioned on the third port of the same chip as a diluent. The reaction was flowed with 30, 60, and 180 s residence times at temperatures of 50, 100, and 150  $^{\circ}$ C. Samples were collected and immediately analyzed by nESI-MS (1  $\mu$ L of each sample was diluted with 99  $\mu$ L of ACN, then loaded into a glass electrospray tip for analysis). Samples were saved and stored at  $-20$   $^{\circ}$ C

### **2.2.10 Microfluidic synthesis of Diazepam (4) from 5-Halo-2-(methylamino)-benzophenone (1).**

Solutions (100 mM) of 5-halo-2- (methylamino)benzophenone (1 eq.) and 200 mM haloacetyl chloride (2 eq.) in toluene or ACN were prepared. Syringes were loaded with the prepared solutions and with 7 N ammonia in methanol (7 eq.). The syringes containing 5-halo-2-(methylamino)-benzophenone and haloacetyl chloride were positioned on the first two inlets of a 10  $\mu$ L Labtrix 3223 chip. The mixture was flowed into a second 15  $\mu$ L Labtrix 3224 chip through the first inlet. A syringe containing toluene, NMP, or ACN was positioned at the second inlet of the 3224 chip to dilute the reaction 4-fold. The syringe containing 7 N ammonia in methanol was positioned at the third inlet of the 3224 chip. A final syringe containing toluene, NMP, or ACN was positioned at the final inlet of the 3224 chip, flowing at a low flow rate of solvent to help avoid fouling at the outlet. The reaction was flowed with residence times of 1 + 0.32 s and 2 + 0.62 s (chip 1 + chip 2) and temperatures of 75  $^{\circ}$ C in chip 1 and 100, 110, 120, or 140  $^{\circ}$ C in the second chip. Samples were collected and immediately analyzed by nESI-MS (1  $\mu$ L of each sample was diluted with 99  $\mu$ L of ACN, then loaded into a glass electrospray tip for analysis). Samples were saved and stored at  $-20$   $^{\circ}$ C.

### **2.2.11 Batch Synthesis of N-(2-Benzoyl-4-chlorophenyl)-2-chloro-N-methylacetamide (3A).**

Chloroacetyl chloride (0.39 mL, 4.9 mmol, 1 eq.) was added to a solution of 5-chloro-2-(methylamino)benzophenone (1.2 g, 4.9 mmol) in 100 mL NMP (50 mM). The reaction was heated to 90  $^{\circ}$ C for 40 min. The solution was then concentrated in vacuo, and the product was isolated via SiO<sub>2</sub> column chromatography in 68% yield. The structure was confirmed by <sup>1</sup>H NMR (Figure 2.1).

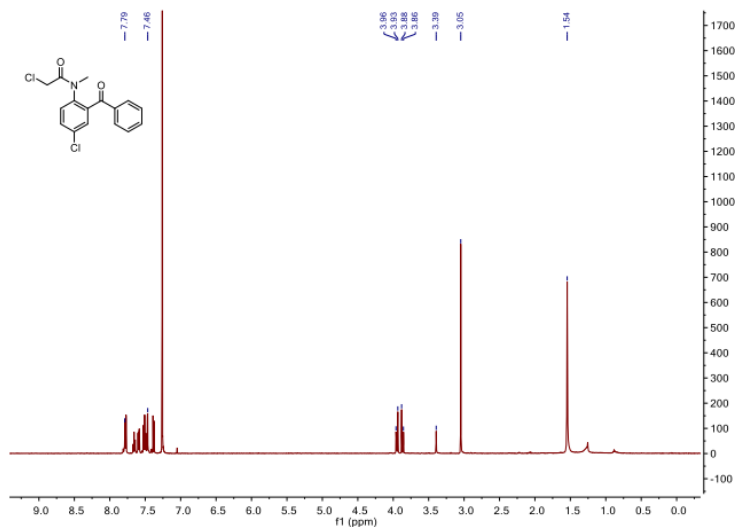


Figure 2.1  $^1\text{H}$ NMR of N-(2-benzoyl-4-chlorophenyl)-2-chloro-N-methylacetamide

## 2.3 Results and Discussion

### 2.3.1 N-Acylation reaction screen

Reaction screening began with examination of the N-acylation step in droplets generated by ESI Leidenfrost droplets, bulk, and flow reaction systems. Initial ESI spray (offline) reaction screening across several solvents [dimethylacetamide (DMA), tetrahydrofuran (THF), dimethylformamide (DMF), acetonitrile (ACN), N-methylpyrrolidone (NMP), and toluene] revealed significant acceleration in ACN ( $\sim 35\times$ ) and toluene ( $\sim 100\times$ ) relative to a 30-minute screen of the reaction in bulk at the same initial concentrations (Figure 2.2, Table 2.1). Although the spray experiment was performed in different solvents, the final extraction before analysis was done in ACN for all experiments. The screening of flow reaction conditions for the first step also began with a solvent screen. NMP and DMF performed poorly, giving limited conversion and significant impurities. N-acylation occurred rapidly and with good conversion in toluene, whereas in ACN, the formation of side products (**5**, **7**) arising from the  $\text{S}_{\text{N}}2$  reaction pathway was observed (Figure 2.2). In addition to solvents, temperatures and residence times were varied. With increasing temperature, in most cases, conversion was poorer due to increasingly prevalent side reactions. By exchanging chloroacetyl chloride for bromoacetyl chloride, we obtained evidence of an alternative reaction pathway (previously reported by Wlekinski et al.).<sup>51</sup> The molecular weight of the expected product of this N-acylation reaction using bromoacetyl bromide is 367; however, we saw an additional

peak at  $m/z$  322. This corresponds to a loss of bromine rather than chlorine, as expected from N-acylation. A mixture of the  $S_N2$  and N-acylation products (from the flow experiment) was isolated by column chromatography, and though they could not readily be separated from one another NMR analysis showed two distinct sets of peaks at 3.7 and 3.9 ppm, corresponding to the methylene protons of the N-acylation and  $S_N2$  products, respectively (Figure 2.3). Guided by these observations regarding the mechanism of the reaction where one solvent favored the more desired pathway and products, we determined that toluene was the optimal solvent for the continuous synthesis of diazepam. In addition to this  $S_N2$  product, we also observed a peak at  $m/z$  288 in our flow experiments, consistent with ring closure to produce a seven-membered lactone. We propose that this  $m/z$  288 compound (mol. wt. 287) is a result of an initial  $S_N2$  reaction, followed by nucleophilic attack by the carbonyl on the acyl chloride to form the seven-membered ring.  $^1H$  and  $^{13}C$  NMR analysis confirmed this proposed structure (Figure 2.4, Figure 2.5 respectively). This result suggests that the selection of reaction solvent and halide can be used to exert control over the reaction outcome in a microfluidic system. It is noteworthy that these alternative outcomes were observed in the microfluidic experiment but were absent in the corresponding droplet experiments. We believe that this is due to the high temperature and pressure conditions accessible in microfluidic reactions, but absent in droplet reactions, making alternative reaction pathways with higher energy requirements more likely.

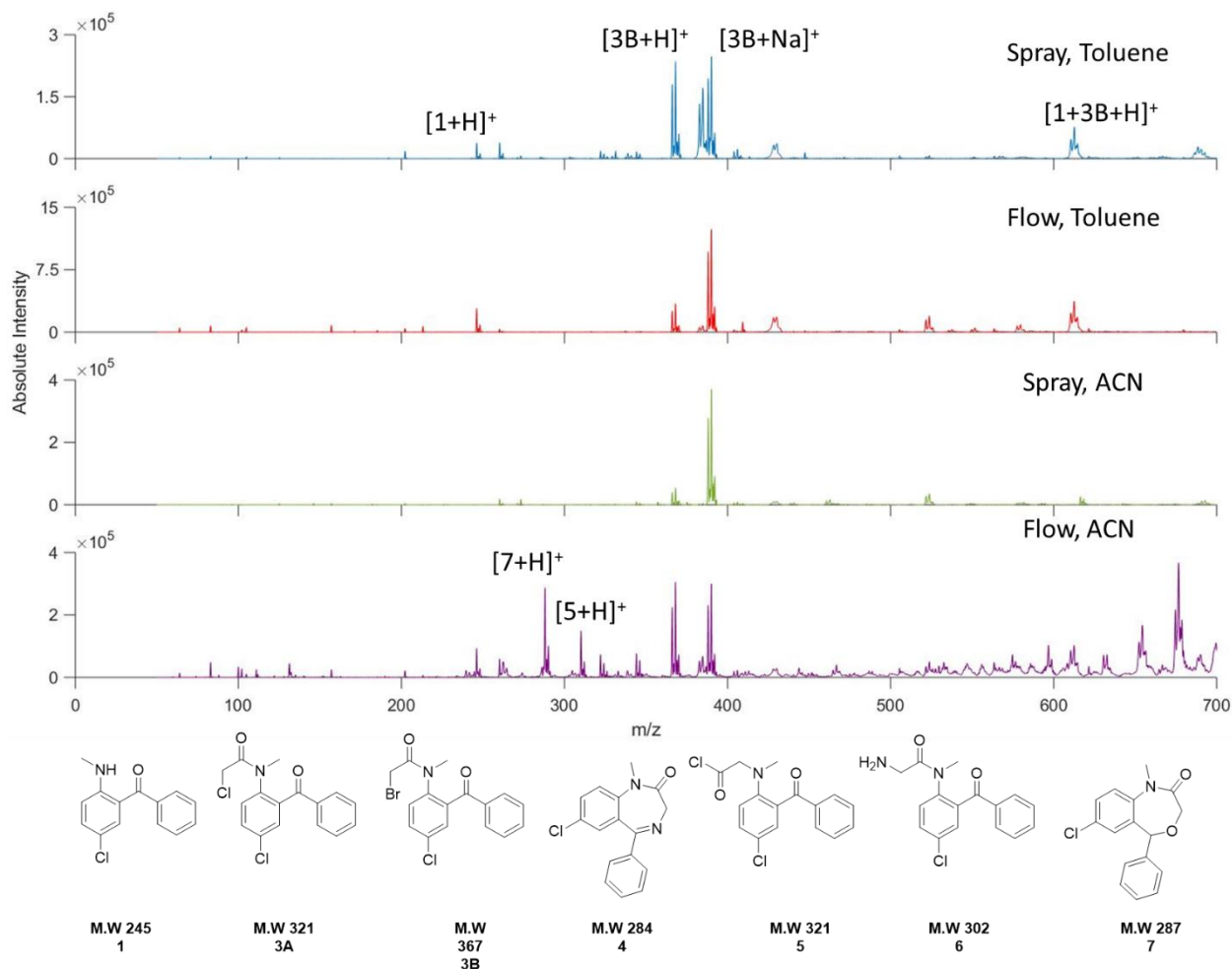


Figure 2.2 N-Acylation screen. Synthesis of **3** using bromoacetyl chloride – comparison of spray and flow in toluene and acetonitrile

### 2.3.2 Cyclization reaction screen

Previous screening of the cyclization reaction space revealed that a greater concentration of ammonia was required to form diazepam in Leidenfrost droplets (Figure 2.6). Reaction acceleration was observed in these droplet reactions, and they corroborated the microfluidic screen. A microfluidic screen of the second step from the N-acylation product **3A**, prepared previously, was carried out prior to attempting both steps in continuous flow. The solvent screen was limited by the low solubility of the chloro version of the intermediate (previously prepared in batch). For each solvent, varying temperatures and residence times were screened. The material was insoluble at a target concentration of 250  $\mu\text{M}$  in ACN and toluene but dissolved well in NMP at this concentration. Fortunately, a good conversion to diazepam was observed in NMP.

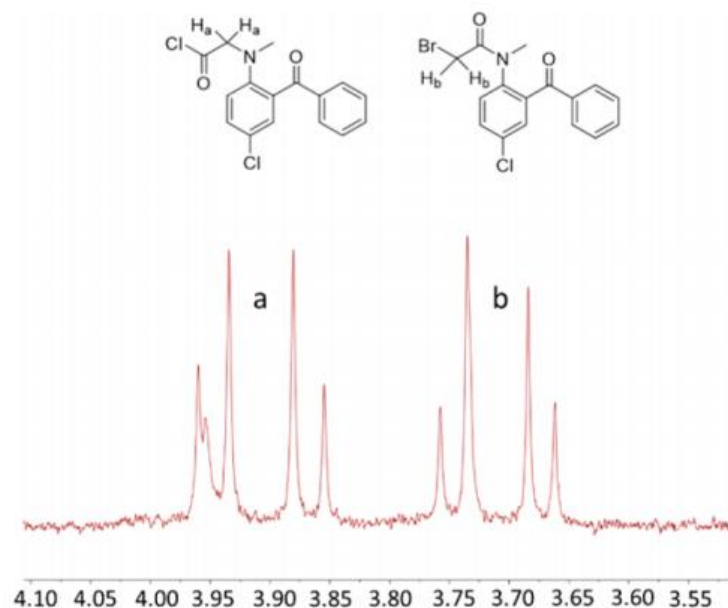


Figure 2.3 Methylene proton  $^1\text{H}$  NMR signals of the  $\text{S}_{\text{N}}2$  and N-acylation product mixture.

Another interesting observation when studying this step was the appearance of a peak at  $m/z$  303. We anticipated that this might represent a substitution of nitrogen at the methyl position. Due to the appearance of this peak in the MS at lower temperatures and residence times, and disappearance at higher temperatures, we also believed that it might be an intermediate in the diazepam synthesis. LC-MS analysis revealed that, despite the previous MS observation, the quantity of this  $m/z$  303 material remained relatively constant throughout the temperature and residence time screen, even as the quantity of diazepam steadily increased. This could be in part due to high ionization efficiency of the  $m/z$  303 material drowning out the signal from other compounds present in the reaction mixture. This  $m/z$  303 material (6) is believed to be a previously reported hydrolysis product of diazepam.<sup>53</sup>

Table 2.1 Acceleration factors for the n-acylation reaction in the synthesis of diazepam

Solvent	Starting material	Acceleration factors <sup>a</sup>	
		ESI spray	Leidenfrost
Acetonitrile	Chloroacetyl chloride	35	25
	Bromoacetyl chloride	29	25
Toluene	Chloroacetyl chloride	97	14
	Bromoacetyl chloride	38	34

<sup>a</sup> Acceleration factors reported in Table 2.1 are apparent acceleration factors given by the ratio of the mass spectrometry signals for the products relative to the starting materials (i.e., the conversion ratio) in the micro droplets relative to the bulk. This is not the same as the ratio of the rate constants for the two media.

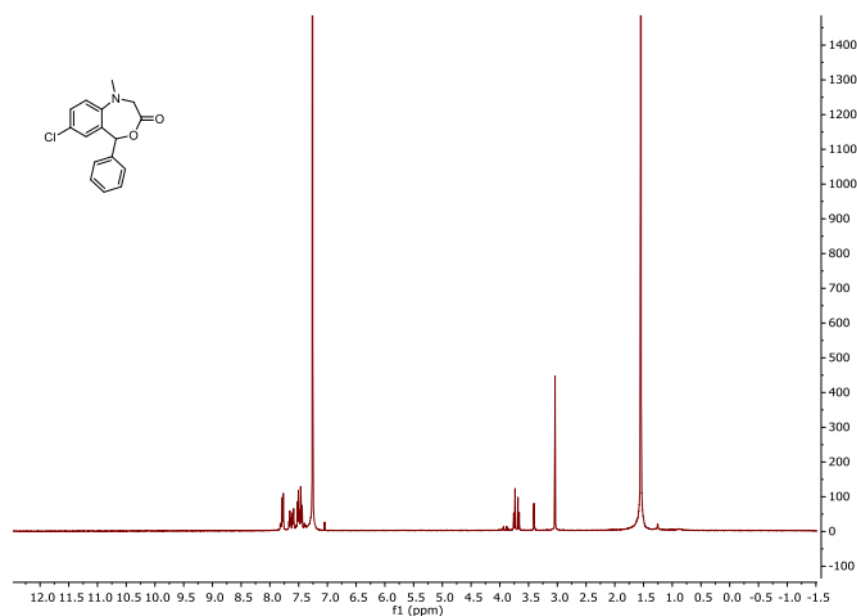


Figure 2.4 <sup>1</sup>H NMR of [7].

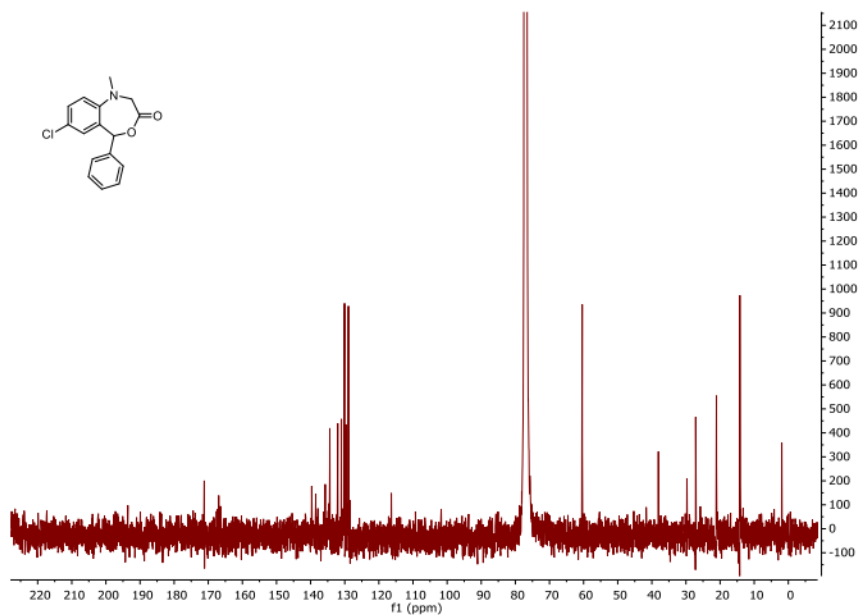


Figure 2.5  $^{13}\text{C}$ NMR of [7].

### 2.3.3 Continuous diazepam synthesis

On the basis of these observations, we were able to develop a more complete understanding of the possible outcomes of each synthetic step of our synthetic route to diazepam. These possible reaction pathways are summarized in Scheme 2.2. Guided by this knowledge from our screening, we next attempted to optimize the synthesis of diazepam in two continuous steps. We used a two-chip reactor system to allow for finer control of temperature and residence time in each chip. The first chip combined 5-chloro-2-(methylamino)benzophenone and haloacetyl chloride in a 1:2 ratio, respectively (Figure 2.7, R1 and R2), before dilution of the resultant N-acylation product mixture (R3) with methanol and subsequent addition of ammonia/ methanol (R4) in a 7-fold excess in the second chip. Solvent screening was again limited by solubility, particularly upon addition of ammonia/methanol in the second step. To alleviate this problem, a dilution step after the first reaction step was incorporated to improve solubility. Good solubility was achieved using toluene for the first step and diluting 1:4 with methanol or NMP. The use of ACN in the first step and for dilution was also effective. As in the previous flow reaction screens, we varied temperature and residence time, as well as the selection of bromo- vs chloroacetyl chloride.

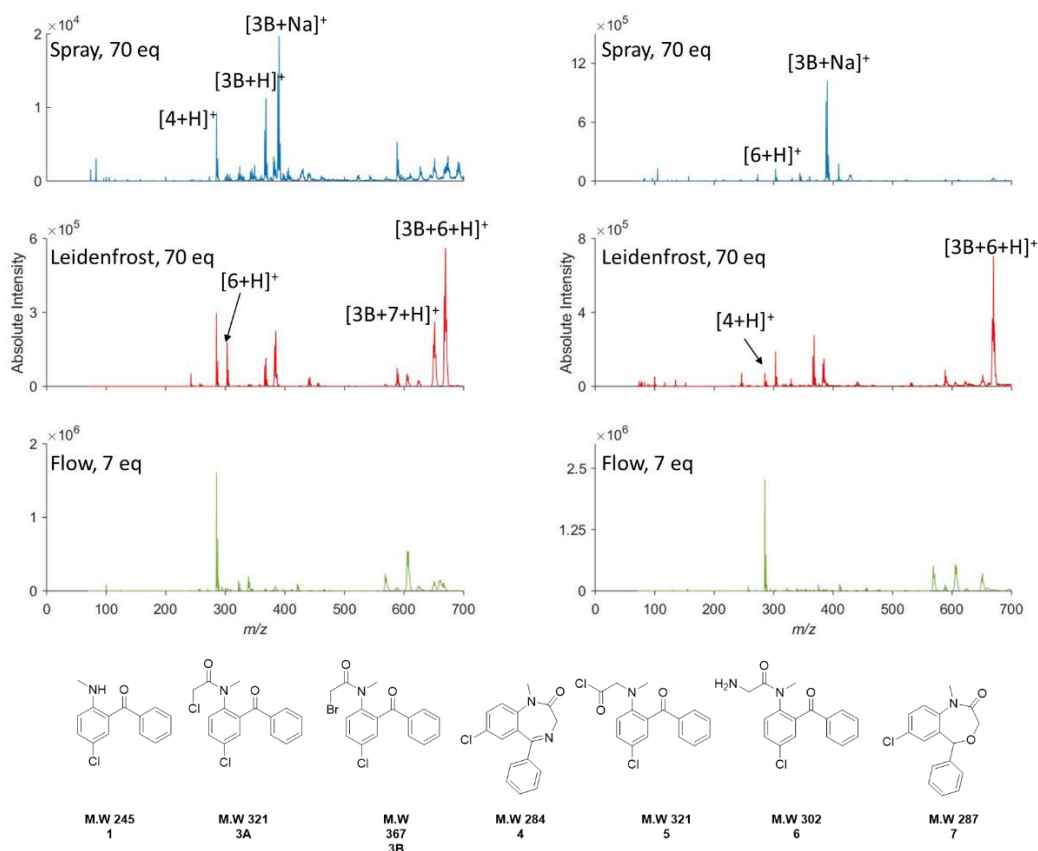
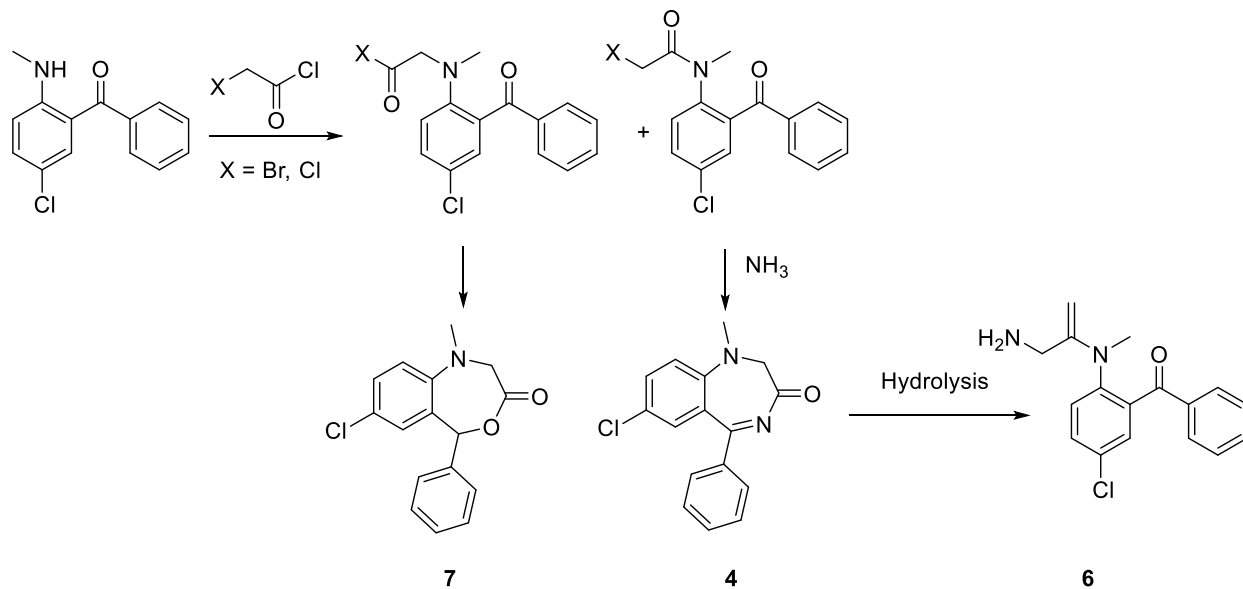


Figure 2.6 Cyclization reaction screen. Synthesis of diazepam, comparing ACN (left) and toluene (right) solvents in spray, Leidenfrost, and flow reactions using bromoacetyl chloride

The results of this screen seemed to corroborate our previous observations, with bromoacetyl chloride resulting in some  $S_N2$  product, particularly in ACN. Furthermore, the overall conversion from the intermediate to diazepam was higher when bromoacetyl chloride was used. Yields for each reaction were determined using a quantitative ESI-MS/MS method. The optimum result was achieved using bromoacetyl chloride in the toluene/methanol solvent system, which yielded diazepam in 100% yield, based on our ESI-MS quantitation method. This was also the optimal solvent system in Leidenfrost and spray microdroplets.



Scheme 2.2 Reaction pathway to diazepam and its by-products formed during continuous flow reaction

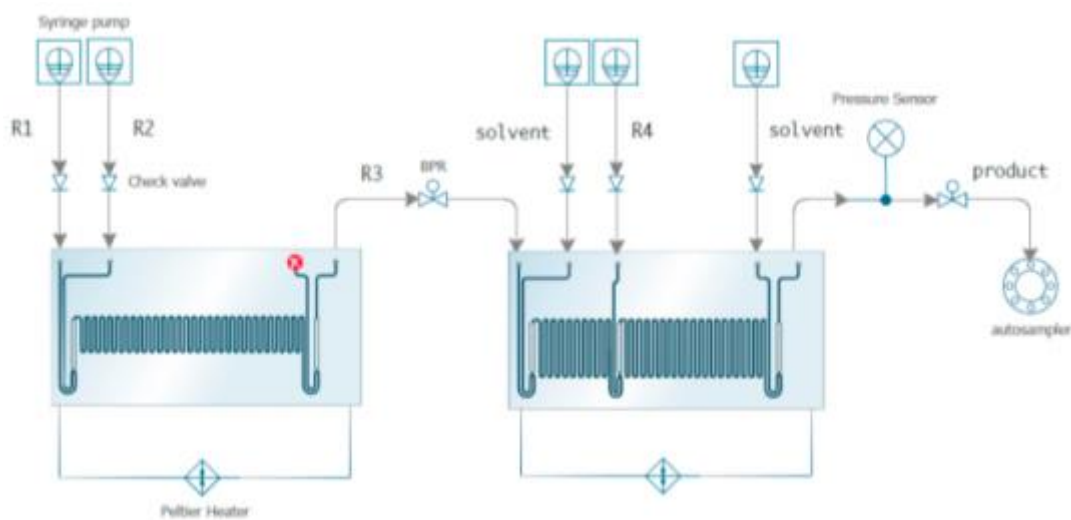


Figure 2.7 Reactor schematic for continuous diazepam synthesis.

## 2.4 Conclusions

This study, using the diazepam synthesis as a model reaction, demonstrates the ability of MS analysis and droplet reactions to guide microfluidic synthesis. MS can be used not only as an analytical tool but can also serve as a quick way to predict reactivity and guide microscale synthesis. The use of spray and Leidenfrost droplet reactions as a screening step to guide the larger scale microfluidic screening proved a useful tool in predicting the overall outcome of a reaction. While some nuances observed in flow reactions were not observed in droplet experiments, these experiments still consistently provided a yes/no indication of the viability of a reaction. Further, we have demonstrated the continuous synthesis of diazepam in two steps in a microfluidic flow reactor. Our synthesis features the use of a mixed solvent system, as well as two microfluidic chips in sequence, allowing for optimized temperature control at each step. Additionally, we have identified previously unknown reaction pathways. These results showcase the possibility for microfluidic synthesis coupled with rapid ESI-MS analysis to identify previously unknown reaction pathways and optimize continuous synthesis of APIs.

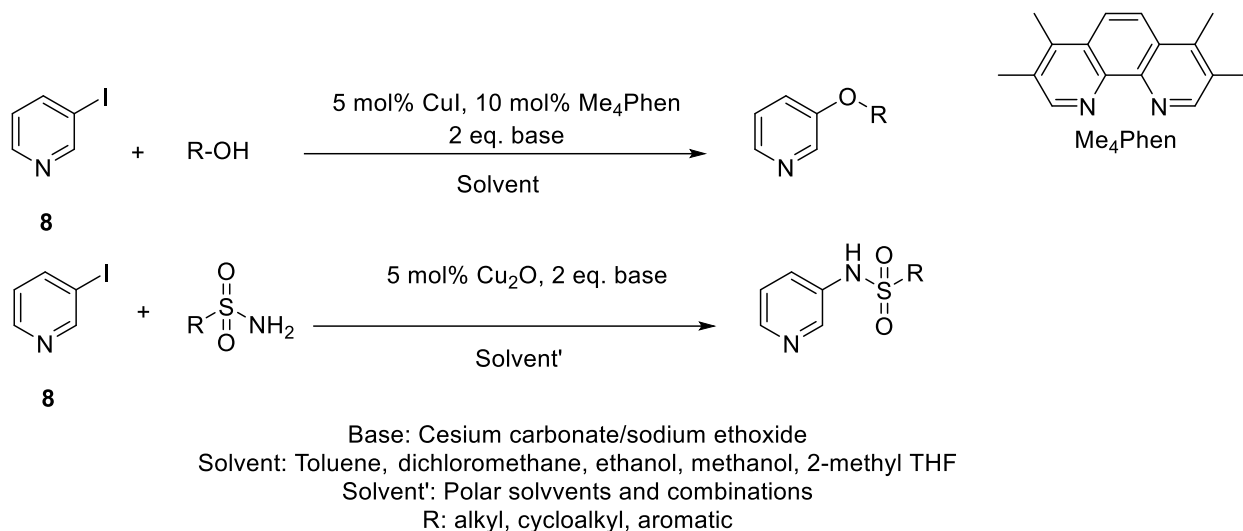
## CHAPTER 3. ACCELERATED MULTI-REAGENT COPPER CATALYZED COUPLING REACTIONS IN MICRODROPLETS AND THIN FILMS

Portions of this work have been published in the journal: Reaction Chemistry and Engineering as the article: “Iyer, K., Yi, J., Bogdan, A., Talaty, N., Djuric, S. W., Cooks, R. G. (2018), Accelerated multi-reagent copper catalyzed coupling reactions in micro droplets and thin films. *React. Chem. Eng.*, 2018, 3, 206”

### 3.1 Introduction

Acceleration of chemical reactions is a valuable tool in the chemical industry for decreasing reaction time, enhancing over-all process efficiency and throughput, and reducing costs.<sup>5, 54</sup> Recently, microdroplets, generated by electrospray ionization (ESI), have been shown to represent media in which many reactions are strongly accelerated.<sup>28, 33, 48, 49, 51, 55</sup> Rate acceleration has been attributed to the reduced activation energy associated with partially desolvated reagents at the interfaces;<sup>33</sup> in confined volume systems the increased surface area-to-volume ratios can make inter-facial reactivity the dominant feature. Changes in pH and reagent concentration upon solvent evaporation also affect reaction rates. A study by Lee et al. has described the development of a droplet array platform that can aid in the control of concentration in a single droplet.<sup>56</sup> In addition to ESI, other ambient ionization methods that can be used to generate micro-droplets include paper spray (PS) and atmospheric-pressure chemical ionization (APCI). In this study, we report the acceleration of two coupling reactions (Scheme 3.1) using ES and PS. Sub-sequent scale-up and product collection in the 20–50 mg scale using ES is also demonstrated for both reactions. Coupling of C–N, C–O, C–S and C–C bonds is widely used in organic synthesis. Earlier studies have shown that these reactions typically require catalytic conditions and stoichiometric amounts of metals such as copper salts or palladium as catalysts.<sup>57-62</sup> Copper is lighter and cheaper than palladium and is hence the preferred catalyst for these couplings.<sup>61, 63-66</sup> Much effort has been devoted to using catalytic copper under milder conditions of pressure and temperature.<sup>67-71</sup> In the present study, we report significant acceleration of both types of coupling reactions, with product being detected almost immediately in the droplets that are generated by spraying. By contrast, the corresponding bulk reactions took 24 – 30 hours to complete. To test the generality of the findings, several experimental setups were used to generate microdroplets for reaction acceleration. All

reagents were handled under nitrogen, but the reaction solution was simply sprayed under ambient conditions.



Scheme 3.1 C-O coupling and C-N coupling using 3-iodopyridine with an alcohol or sulfonamide as reagents

### 3.1.1 Reagents

Reagents were purchased from Sigma Aldrich (Milwaukee, WI) and used without any further purification.

### 3.1.2 Electrospray experiments

Configuration of the reaction apparatus is shown in Figure 3.1 (a). A small piece of KimWipe (1cm x 1cm) was rolled and plugged into one end of a borosilicate glass capillary (Sutter Instrument, Novato, CA, O.D.:1.5mm, I.D.:0.86mm). This was placed into a round bottom flask along with a magnetic stirrer with the KimWipe plug at the bottom of the flask. For the C-O coupling reaction, 1.5 mM of alcohol, 0.050 mM of copper(I) iodide, 0.10 mM of 3,4,7,8-tetramethyl-1,10-phenanthroline (Me4Phen) and 1.5 mM of base was placed in the round bottom flask. The solvent used was toluene. For the C-N coupling reaction, 1.5 mM of the sulfonamide, 2mM of the base and 0.020 mM of copper(I) oxide was placed in the flask. The solvent used was THF: Water (3:1). The flask was sealed with a rubber septum. A ~15 cm long fused silica capillary (Polymicro Technologies, Phoenix, AZ, O.D.: 360 $\mu$ m, I.D.: 100 $\mu$ m) was passed through the septum with the aid of a precision needle until it reached the borosilicate glass capillary. The other

end of the fused silica was positioned in front of the MS inlet with the aid of a second precision needle. The flask was then connected to a nitrogen supply where the flow was set to 1L/min. The positive pressure of nitrogen helps the reaction mixture flow through the fused silica capillary. The first minute or so is used to make sure that we have a stable spray from the fused silica capillary. This can be done by observing spectra online or by illuminating the spray with the aid of a laser pointer. Both methods were employed to confirm the presence of a steady spray. Once the spray was found to be steady, 1.0 mM of 3-iodopyridine in 1.5 ml of toluene (for C-O coupling) and 3-iodopyridine in THF:water (3:1) (for C-N coupling) was added to the flask with the help of a syringe. A voltage of +3 kV was applied to the precision needle and spectra were recorded using an LTQ ion trap mass spectrometer (Thermo Fisher Scientific, San Jose, CA)

### **3.1.3 Paper spray experiments coupled with atmospheric pressure chemical ionization (APCI)**

Configuration of this reaction setup is shown in Figure 3.1 (b). The reactants were mixed the same stoichiometric amounts as in the ES experiments. The resultant reaction mixture was filtered and loaded into a syringe that was used to spray the reaction mixture onto a small (about 1 cm on a side) equilateral triangle cut from Whatman Chromatography paper (Cat No. 3001-861, Buckinghamshire, UK). A voltage of +7kV was applied to the paper and a flow rate of 20 $\mu$ L/min was used. When paper spray was used in conjunction with APCI, the setup was just slightly modified to include a silver APCI needle right in front of the paper spray plume. The APCI needle was held at a voltage of +3kV for all experiments.

### **3.1.4 ESI experiments for offline collection (C-O coupling)**

Configuration of the ES apparatus is shown in Figure 3.1 (c). The reagents were mixed and loaded onto a Hamilton syringe and operated with the aid of a Hamilton syringe pump. The flow rate was kept constant at 30  $\mu$ L/min. The collection surface was a grounded 20 ml scintillation vial. The scintillation vial was cooled in a mixture of dry ice and acetone during collection to prevent evaporation of the collected product. An external power supply was used to apply voltage (+5 kV) to the needle.

### 3.1.5 ESI experiments for offline collection (C-N coupling)

The ES setup used for offline collection of the C-N coupling product is very similar to what is shown in Figure 1a. the setup shown is slightly modified to include two additional fused silica lines and hence aid in multiplexing. The collection surface used was glass wool that was contained in a 20 ml Falcon tube (Fisher Scientific, New Hampshire, USA). An external power supply was used to apply voltage (+4 kV) to the fused silica lines. The total spray time was 40 min.

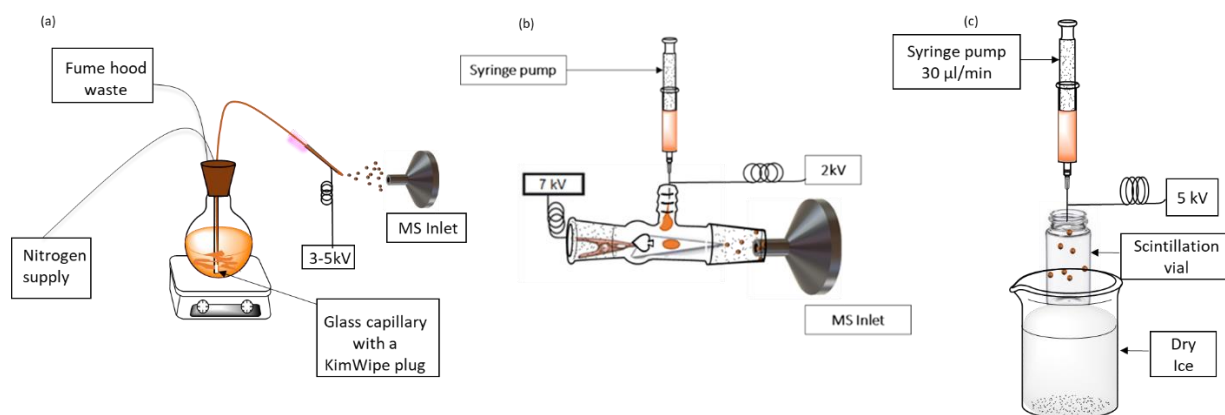


Figure 3.1 Apparatus for (a) electrospray, (b) paper spray and (c) scale up (C-O coupling only)

### 3.1.6 Bulk/batch experiments

Bulk experiments were performed by placing stoichiometric amounts of reagents in a closed round bottom flask. The C-O coupling reaction (using ethanol and 3-iodopyridine) was carried out at 90°C for 12 hours. The reaction mixture was diluted with ethyl acetate, washed with saturated brine and dried over sodium sulfate. Reduced pressure distillation was used for purifying the product. The C-N coupling reaction (using different sulfonamides and 3-iodopyridine) was carried out in a closed system at to 130°C for 30 hours. The reaction mixture was allowed to cool and diluted the methanol. The extract was dried over anhydrous sodium sulfate and the solvent was removed under reduced pressure. The crude product was then loaded onto a column and purified. All products were characterized using  $^1\text{H}$  NMR spectroscopy.

## 3.2 Results and Discussion

### 3.2.1 C-O coupling

First, we explored the C–O coupling reaction between 3-iodopyridine and various alcohols. The base used for the C–O coupling reaction was cesium carbonate and the solvent was toluene. Online MS using ES (Figure 3.1 (a)) and PS (Figure. 3.1 (b)) showed product a minute after beginning to spray the reaction mixture when using ethanol as the coupling partner (Figure 3.2 (a)). It is to be noted that the first minute is used in stabilizing the spray from the positively pressurized reaction vessel before adding the 3-iodopyridine to the reaction flask. The accelerated reactions occur in the sprayed droplets in the case of electrospray and/or the thin film deposited on the paper substrate in the case of paper spray. In contrast, the bulk reaction does not show any product formation when analyzed using nano-electrospray ionization (nESI); in fact, the bulk reaction required close to 30 hours and 80–130 °C for completion. The spray volumes and voltages used in nESI are smaller than those used in ESI and the short distance over which nESI droplets travel does not allow for acceleration. The time difference (30 h vs. 1 min) corresponds to an acceleration factor of several orders of magnitude in droplets when compared to the bulk reaction. Formation of product was confirmed by recording MS/MS when selecting the ions,  $m/z$  124, corresponding to the protonated ether (Figure 3.3). Sodium ethoxide was chosen as a base for this reaction since it showed greater conversion efficiency than cesium carbonate which has been used in previously reported studies.<sup>70</sup> Cesium carbonate also posed solubility problems which was overcome by using sodium ethoxide. Sodium ethoxide was hence chosen for scale up over cesium carbonate. PS was also explored for reaction acceleration. PS is also an ambient ionization technique like ES in which reagents are dropped onto a piece of triangular paper. As the solvent evaporates, a thin film is formed on the paper and when a potential is applied, a spray is generated from the tip of the paper. Although acceleration was observed, PS is not amenable to scale up since the paper does not maintain its integrity for long periods of spray duration. Hence PS was not explored for offline collection and scale up but was instead used as an additional analytical method to demonstrate reaction acceleration. The setup for ES scale up is shown in Fig. 3.1 (c). A grounded scintillation vial (20 ml) was used as the collecting surface.

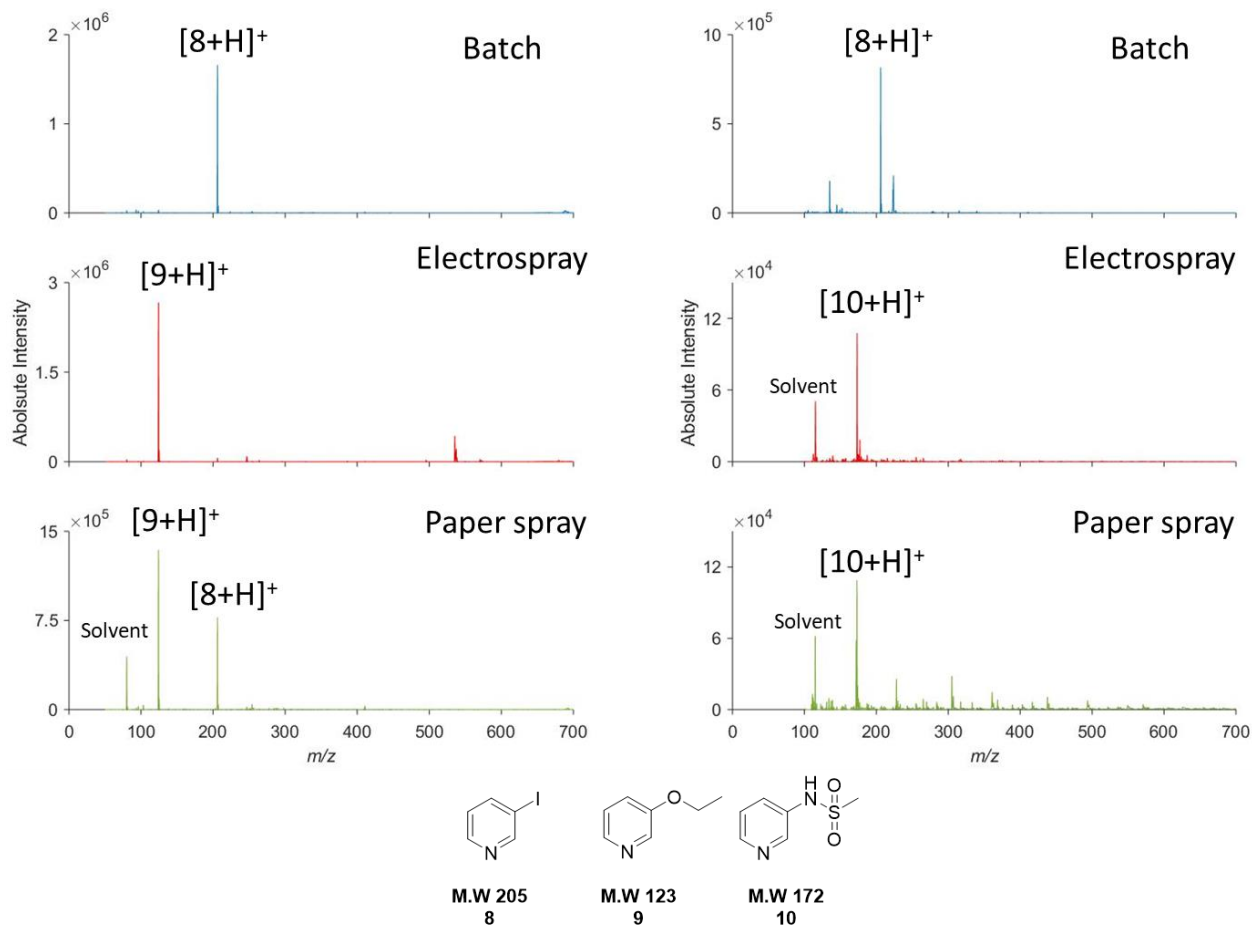


Figure 3.2 Mass spectra for C-O coupling (a) and C-N coupling (b) – comparison of bulk/batch mode (2 min), electro spray (2 min) and paper spray (2 min)

The scintillation vial was cooled in dry ice during collection to minimize loss of the volatile product. The collected product was rinsed with deuterated chloroform and characterized by NMR (Figure 3.4). Quantitation was performed by adding an internal standard (1,3,5- trinitrobenzene) to the rinse. The production rate was found to be 55 mg/35 minutes and the yield was a modest 45%. Further multiplexing should improve efficiency. In addition to ethanol, other reagents were explored for reaction acceleration. The MS conversions (product ion abundances vs. total of products and reagents) of these substrates are reported in Table 3.1. The trend observed with the different reagents agrees with the trends seen in bulk reactions. Primary alcohols show higher yields when compared to secondary and tertiary alcohols due to steric effects. Hence accelerated reactions using ES can also be used as predictors of successful route in route scouting as a yes/no

tool for these types of coupling reactions. This application is one of the more important ways of employing the acceleration effect as previously demonstrated by Wleklinski et al.<sup>51</sup>

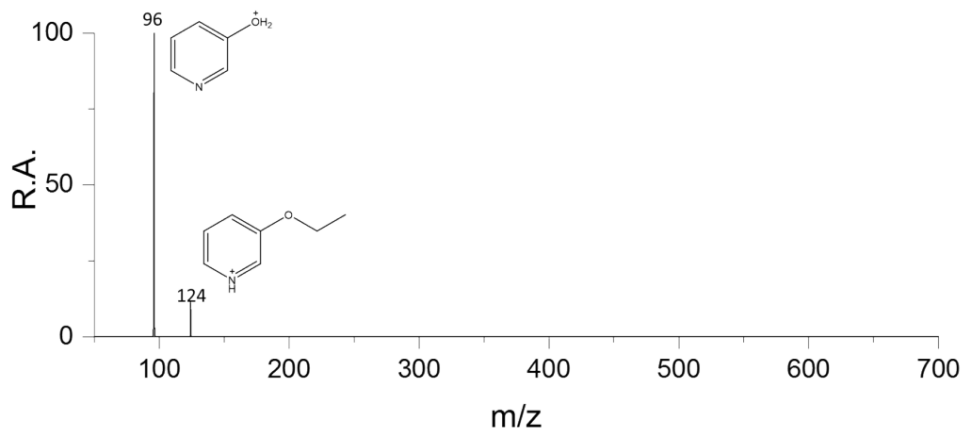


Figure 3.3 MS/MS spectra for ions corresponding to  $m/z$  124

### 3.2.2 C-N coupling

We explored C–N coupling using 3-iodopyridine and various sulfonamides. Online MS using ES (Figure 3.1 (a)) shows product formation within the first minute of spraying the reaction mixture (Figure 2 (b)). Again, the first minute or so is used for spray stabilization and to prime the lines. Product formation was confirmed by performing an MS/MS scan (Figure 3.4).

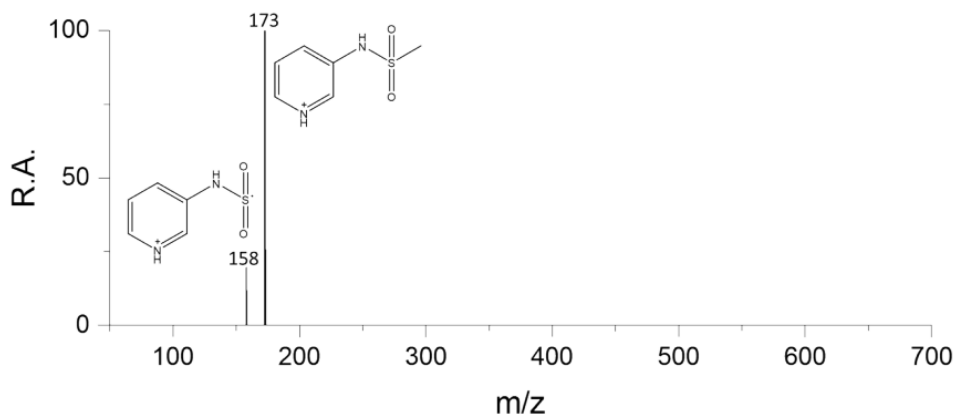


Figure 3.4 MS/MS spectra for ions corresponding to  $m/z$  173

The ES setup for the reaction was similar to that used in the C–O coupling reactions. Cesium carbonate was initially used as the base for the reaction. However, these spectra were dominated by cesium peaks. Different bases and solvent systems were therefore explored (Table 3.1) and potassium hydroxide was chosen as a suitable base for this reaction since it showed better MS conversion. The best solvent system was tetrahydrofuran: water in a 3:1 (v/v) ratio. Reaction acceleration was observed with PS as well, but ES was chosen as the preferred method of scale up for the reasons stated before. The apparatus for the scale up was the same as that used in the ether formation ES experiments. However, for scale up, multiple fused silica lines were used to spray the reaction mixture onto the glass wool which was used as the collection surface. The product was collected, rinsed with deuterated solvent and then confirmed by  $^1\text{H}$  NMR (Figure 3.6).

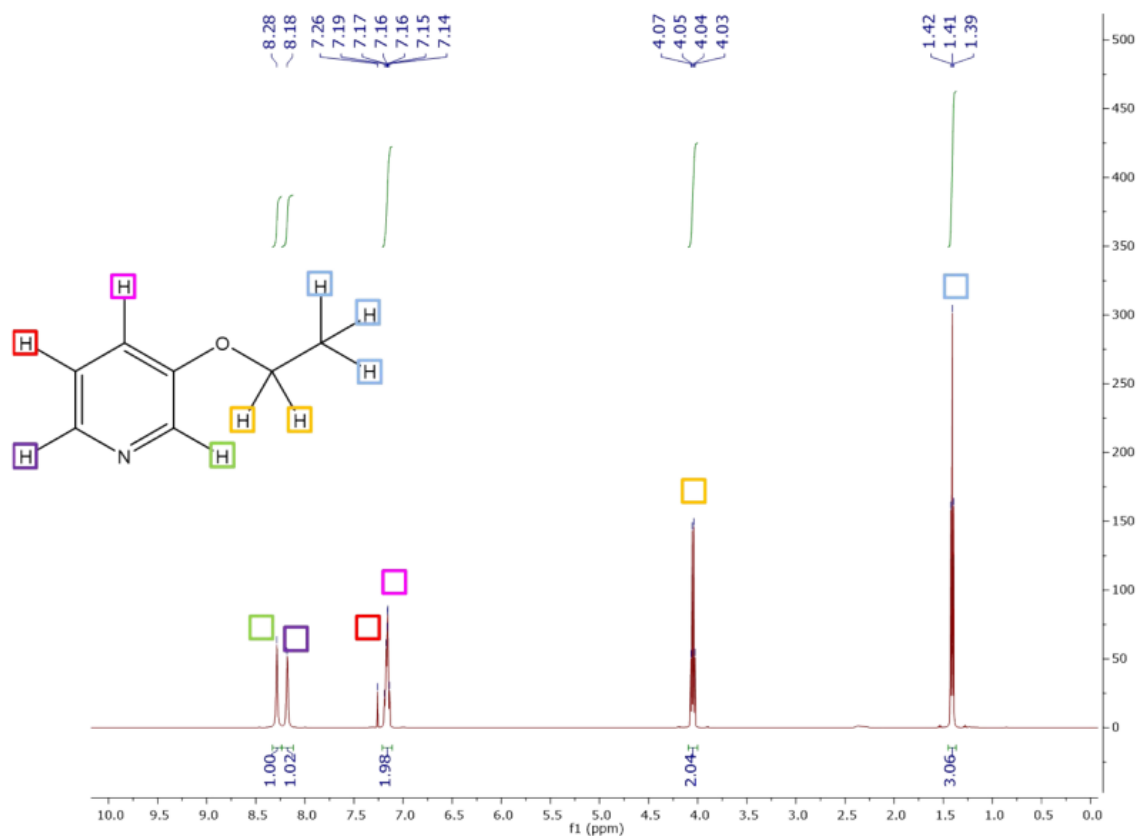


Figure 3.5  $^1\text{H}$  NMR of the C–O coupling product (using ethanol as the reagent) – offline collection using ES

Different reagents were explored for C–N coupling as well. Those studied included sulfonamides such as ethanesulfonamide, cyclopropylsulfonamide, tertbutylsulfonamide and benzenesulfonamide. Interestingly, we observed a  $[M + H]^+$  peak with methanesulfonamide, but observed the radical cation  $[M]^+$  in the case of the other sulfonamide substrates. Also interesting was the fact that the ions corresponding to the  $[M]^+$  signals did not undergo fragmentation under any conditions, at high collisions energies the ion signal disappeared presumably due to charge exchange. The MS conversions of the different substrates are listed in Table 3.2.

Table 3.1 Systems explored for the C-N coupling reaction between 3-iodopyridine and methanesulfonamide

Base	Solvent	Catalyst	Comments
Cesium carbonate	Water	Cu <sub>2</sub> O	Spectrum dominated by cesium peaks
	Methanol	Cu <sub>2</sub> O	Spectrum dominated by cesium peaks
Potassium carbonate	Methanol:water (3:1)	Cu <sub>2</sub> O	No product formation
Sodium ethoxide	Methanol	Cu <sub>2</sub> O	No product formation
	Isobutyrylcyclohexanone	CuI	No product formation
Sodium hydroxide	Methanol	Cu <sub>2</sub> O	No product formation
	Methanol:water (1:1)	CuI	No product formation
Potassium hydroxide	Isobutyrylcyclohexanone + DMF	CuI	No product, only DMF peaks seen
	Isobutyrylcyclohexanone + THF	CuI	Product formed
	THF:water (1:1)	Cu <sub>2</sub> O	Product formed

We performed an additional bulk reaction using ethanesulfonamide to verify our findings with reference to the  $[M]^+$  ion. The bulk reaction mixture (at the end of 30 hours) was sprayed using nESI and the high-resolution MS showed the formation of the  $[M]^+$  ion, (Figure 3.6) thus confirming that the ES generated product is indeed the desired product. These ancillary observations prompted us to explore different pyridines to confirm if the trend existed across o-,m-

and p-substituted iodopyridines. Using the ESI setup as described before, we performed the reaction with 2,3 and 4-iodopyridine with methanesulfonamide and ethanesulfonamide. The trend observed is the same as seen with 3-iodopyridine. Methanesulfonamide forms the  $[M + H]^+$  ion while ethanesulfonamide forms the radical cation  $[M]^+$  ion.

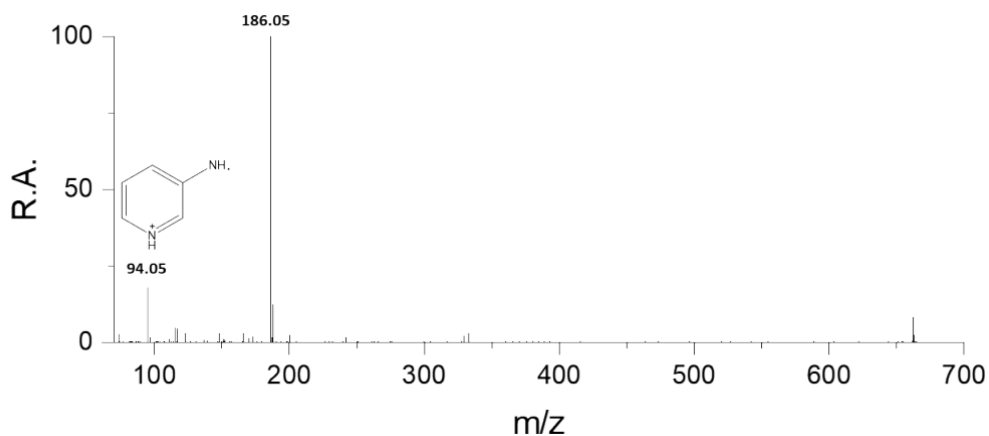


Figure 3.6 High-resolution MS of the bulk reaction using ethanesulfonamide as the starting reagent showing the radical cation of the pyridylsulfonamide as the major reaction product

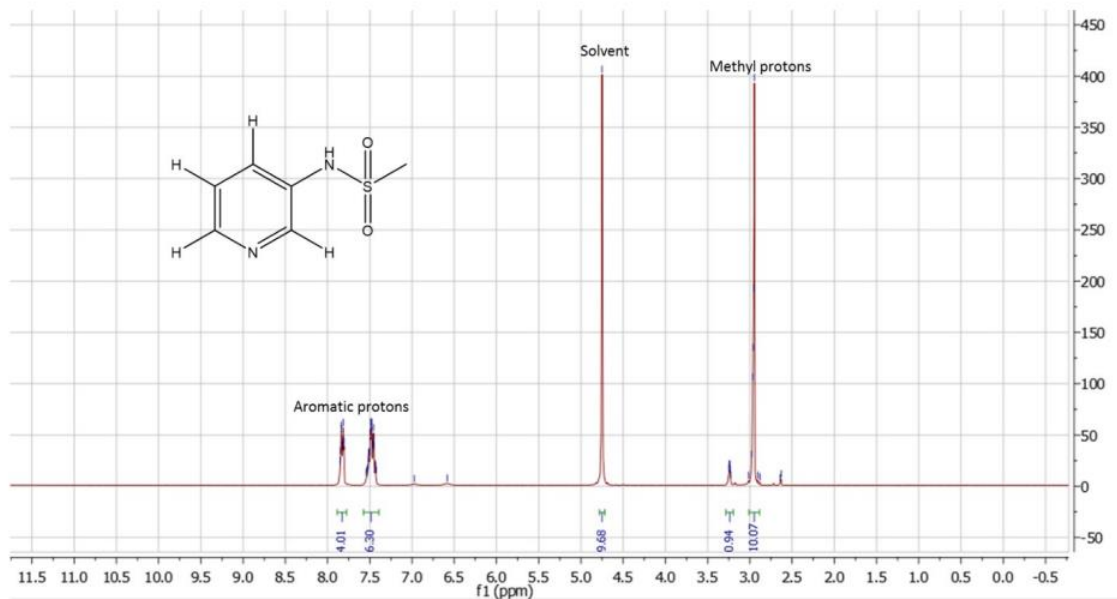


Figure 3.7 <sup>1</sup>H NMR of C-N coupling product – offline collection using ES. Solvent: Methanol-d<sub>4</sub>

Table 3.2 Substrate scope – relative abundance (R.A) yields of different substrates used for C-O and C-N coupling using 3-iodopyridine

<b>Alcohol (C-O coupling)</b>	<b>Product ion</b>	<b>R.A yields<sup>a</sup></b>	<b>Sulfonamide (C-N coupling)</b>	<b>R.A yields<sup>a</sup></b>	<b>Product ion</b>
Ethanol	[M+H] <sup>+</sup>	100	Methanesulfonamide	[M+H] <sup>+</sup>	100
1-Hexanol	[M+H] <sup>+</sup>	96	Ethanesulfonamide	[M] <sup>+</sup>	63
Cyclohexanol	[M+H] <sup>+</sup>	17	Cyclopropylsulfonamide	[M] <sup>+</sup>	50
1-butanol	[M+H] <sup>+</sup>	100	<i>t</i> -butylsulfonamide	[M] <sup>+</sup>	20
<i>t</i> -butanol	[M+H] <sup>+</sup>	0	Benzenesulfonamide	[M] <sup>+</sup>	66

### 3.3 Conclusions

In summary, we have demonstrated the acceleration of two air and water sensitive coupling reactions using droplets generated in ES. We have also shown the acceleration of a heterogeneous reaction by modifying the ESI setup to include online filtration. A third finding, confirming earlier data,<sup>4</sup> is that by doing a substrate scope experiment, it is possible to use accelerated reactions as a predictor for bulk reactions. Finally, we have demonstrated scale up to the 10's of mg of representative examples of these reactions. This form of preparative MS is clearly a valuable tool for the synthesis of small quantities of product. Multiplexing these systems should aid in the synthesis of larger quantities of product in a short amount of time.

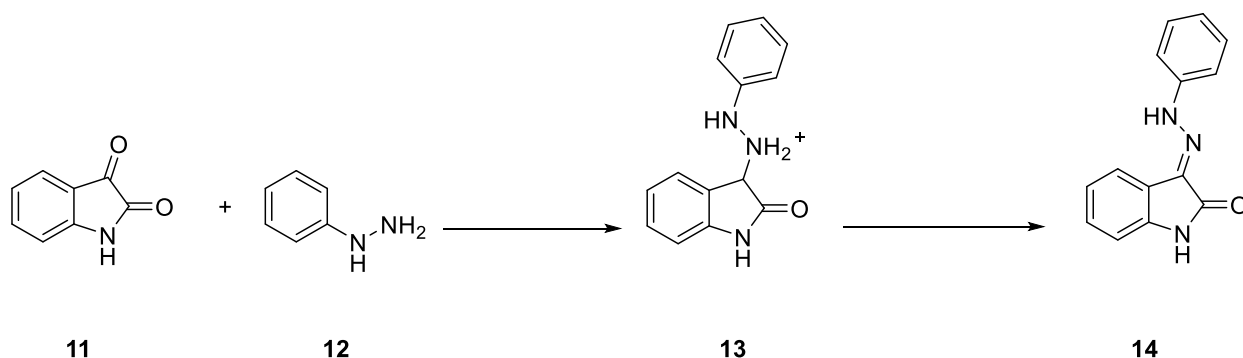
## CHAPTER 4. REACTION ACCELERATION IN ELECTROSPRAY DROPLETS: SIZE, DISTANCE AND SURFACTANT EFFECTS

Portions of this chapter have been published in the Journal of the American Society for Mass Spectrometry as the article “Marsh, M. B, Iyer, K., Cooks, R.G. (2019) Reaction acceleration in electrospray droplets: size, distance and surfactant effects, J. Am. Soc. Mass Spectrom. (2019) 30: 2144. <https://doi.org/10.1007/s13361-019-02287-3>”

### 4.1 Introduction

Control of reaction rates is a shared goal of all branches of chemistry. While catalysts and heat<sup>72</sup> have been studied in great detail, recent studies of reactants in microdroplets and thin films suggest that confined reaction volumes too can greatly enhance reaction rates compared to those in bulk solution.<sup>5, 31, 33, 34</sup> A growing body of literature exists which shows that many common organic reactions<sup>49, 73-77</sup> and some inorganic particle formation processes,<sup>78</sup> are accelerated in charged microdroplets generated in the course of electrospray and nanoelectrospray ionization (nESI). Despite the growing number of accelerated reactions that have been studied, open questions remain about the origin of the observed acceleration. In charged microdroplets, reaction rates increase with decreasing droplet size (increasing surface area to volume ratio)<sup>5, 33, 49, 74, 77</sup> implying that the surface of the droplet is intimately involved with the increase in reaction rates observed in these systems. Fluorescence anisotropy measurements of a rhodamine dye in an oil-water emulsion show interfacial enhancement of molecules in droplets, directly implicating a surface-mediated process.<sup>31</sup> The interface of a solution, either with air as in aerosols<sup>79</sup> or levitated droplets,<sup>22, 80</sup> or with a non-miscible solvent as in so-called on-water reactions,<sup>57, 81</sup> has a different solvation environment than does bulk solution, in part due to alignment of molecules at the interface.<sup>82</sup> This results in changes in the potential<sup>81</sup> energy surface for reaction.<sup>34</sup> In fact, one suggested explanation of the increased surface reactivity<sup>82</sup> is partial solvation of reactants at the interface.<sup>33</sup> In this work, a series of systematic experiments was performed to elucidate the influence<sup>29</sup> of experimental factors and the underlying causes of reaction acceleration in charged<sup>51</sup> microdroplets produced by nESI. Hydrazone formation from isatin (scheme 4.1)<sup>33</sup> was chosen as a model reaction to measure the influence of distance, tip size, and surfactant concentration on<sup>83</sup> reaction acceleration. Super resolution microscopy was used to measure the diameters of droplets of different types; this measurement was made on the droplets after impact on a collector surface. It provides information

on the effects of spray tip diameter and evaporation on the size of nESI droplets. Another set of experiments measured the influence of surfactant concentration on the droplet size distribution. Correlation of the distance, tip diameter and surfactant effects on droplet size, as measured by splash microscopy, provided a picture of microdroplet size effects on reaction acceleration. Initial data on the use of ambient ion focusing on acceleration were taken also, in view of the potential value of such focusing in increasing the scale on which organic synthesis might be performed using nESI sprays.<sup>51</sup>



Scheme 4.1 Formation of 3-(2-phenylhydrazono)indolin-2-one (**14**) from the reaction of indoline-2,3-dione (**11**, isatin) with phenylhydrazine (**12**) in methanol proceeding via reaction intermediate (**13**)

## 4.2 Experimental

### 4.2.1 Microscopy

3D structured illumination microscopy (SIM) experiments were performed using a super resolution Nikon Ti-E microscope. The experimental details of this process have been discussed previously.<sup>29</sup> Briefly, a laser light source of 561 nm was used, the total magnification was 250x. nESI emitters were used as the spray source and a 100  $\mu$ M Rhodamine B solution in methanol:glycerol 9:1 was used as the spray solution. Previous studies<sup>30</sup> have shown that glycerol containing droplets measured using the microscopy method, match reasonably well to PDA studies of droplets containing 1:1 water: methanol. This suggests that surface wetting does not change the sizes of the droplets significantly from corresponding air-based measurements. nESI emitters were pulled from borosilicate glass capillaries (0.86 mm I.D., 1.5 mm O.D.) using a micropipette puller to achieve an O.D. of  $20 \pm 0.5$   $\mu$ m (I.D. estimated at 11  $\mu$ m from initial capillary dimensions). The

tip diameters were confirmed by visual observation using a Kronos light microscope equipped with a scale bar. All nESI experiments were performed using a platinum-iridium wire as the electrode. An external voltage of 4 kV was supplied to the emitter from an external high voltage power supply. The external power supply was connected to a waveform generator to allow pulsed voltages to be applied. Pulsing was performed to avoid the formation of droplet aggregates, which is common with a continuous spray. The pulse duration used for this experiment was 20 ms. Droplets were collected on a grounded indium-tin-oxide (ITO) coverslip (Nano CS, NY, USA) that was approximately 0.16 mm thick and placed in contact with the objective. Two sets of experiments were performed, the first of which measured the effect of distance on droplet size. Distances of 3 mm and 9 mm were used to study the effect of this variable. Note that the distance refers to the distance between the tip of the nanospray emitter and the surface of the coverslip. The second set of experiments measured the effect of the concentration of the surfactant on the droplet size. For both experiments, ten frames were acquired for each setting. For the distance experiments, ten image frames were acquired for each distance and then normalized prior to analysis. A modified circular Hough transformation function in Matlab was used to detect and measure droplet size. An overlap removal algorithm was used to identify incorrectly assigned droplets and remove any overlaps associated with them.

#### **4.2.2 Nanospray measurements of reaction acceleration**

Mass spectrometric measurements were performed using an Agilent Ultivo triple quadrupole instrument. Briefly, a nESI emitter was connected to an external high voltage power supply while the inlet capillary of the mass spectrometer was held at 100 V. The DC voltage used for all nESI experiments was 2 kV. The nESI emitter was positioned at the appropriate distance from the mass spectrometer and the mass spectrum was recorded for one minute. For the tip size experiments, pulled borosilicate glass emitters with O.D.'s of 1  $\mu\text{m}$ , 5  $\mu\text{m}$ , and 20  $\mu\text{m}$  (estimated I.D.'s of 0.6  $\mu\text{m}$ , 3  $\mu\text{m}$ , 11  $\mu\text{m}$ , respectively) were used, while 5  $\mu\text{m}$  diameter emitters were used for all other mass spectrometry measurements. Reaction mixtures were prepared by mixing 1 ml of 3 mM isatin (**11**) in methanol with 10  $\mu\text{L}$  phenylhydrazine (neat) (**12**). An aliquot (1  $\mu\text{L}$ ) of 1 M methanolic HCl was then added to the reaction mixture.

## 4.3 Results and Discussion

### 4.3.1 Microscopy-distance experiments

Previously<sup>29</sup> it was shown that super resolution microscopy can be adapted to measure the sizes of droplets produced via paper spray and nESI. These results indicated that the size of nESI droplets depend on, among other factors, the size of the nESI emitter. As the emitter diameter decreased so did the mean droplet diameter produced during spraying. Measurements at 3 mm distance, with 20  $\mu\text{m}$  O.D. emitters, gave a mean droplet diameter of 1.5  $\mu\text{m}$  and a 5  $\mu\text{m}$  emitter gave a mean droplet diameter around 500 nm. In this work, the influence of spray distance, and by extension droplet flight time, on droplet size was considered. The spray distance refers to the distance between the tip of the nESI emitter and the collection surface and/or the inlet of the mass spectrometer. Figure 4.1 shows super resolution images of droplets produced by the nESI emitter at 3 mm and 9 mm distances and the corresponding droplet size distributions. The distance from the nESI tip to the surface of the conductive coverslip used as the collector surface was measured using Vernier calipers. Methods used to capture and generate images for the experiments have been described previously.<sup>29</sup> The effect of distance on droplet size can be clearly seen from Figure 4.1. It should be noted that the frame shown above is one of several and is not representative of the entire droplet plume. Closer distances generate larger droplets while the droplet size decreases as the emitter is moved away from the surface. Larger distances allow greater flight times for the droplets, which in turn provide more time for droplet evaporation. The droplets evaporate until they undergo Coulomb fission, as described by the Rayleigh relation, given as

$$Q_{crit} = 64\pi\epsilon_0\gamma r^3$$

where  $Q_{crit}$  is the critical charge,  $\gamma$  is the surface tension of the droplet solvent, and  $r$  is the droplet radius. Coulomb fission serves to further decrease the size of nESI droplets. These results are consistent with observations of droplet evaporation in paper spray and standard ESI.<sup>30, 83, 84</sup>

### 4.3.2 Microscopy – surfactant experiments

Microscopy experiments were also performed to assess the effect of a typical surfactant, cetyltrimethylammonium chloride (CTAC), on droplet behavior. A solution of 100  $\mu\text{M}$  Rhodamine B in 9:1 methanol:glycerol containing varying amounts of surfactant (0 mM, 0.1 mM, 1 mM and 10 mM) was used in all experiments as the spray solution. As shown in Figure 4.2, as the concentration of the surfactant was increased, the droplet size decreased. While no comparisons

could be drawn between this system and known experimental data due to the high phenylhydrazine and glycerol content of the solution, there is significant evidence that, while methanolic solutions

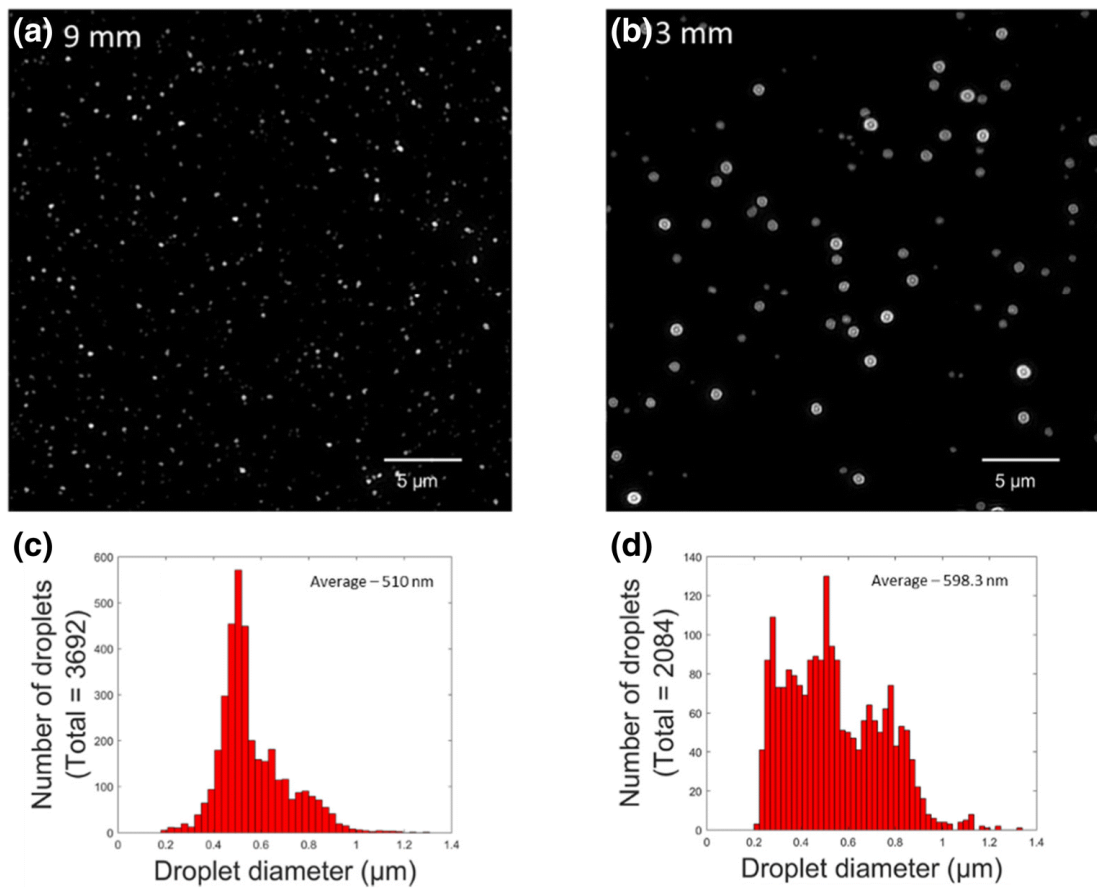


Figure 4.1 Super resolution microscopy images of 100  $\mu\text{M}$  Rhodamine B in 9:1 methanol:glycerol droplets produced by nESI at distances (a) 9 mm and (b) 3 mm. Corresponding diameter distributions for (c) 9 mm and (d) 3 mm are also shown

a change in surface tension, resulting in faster fission of the nESI droplets and lower average droplet diameters.

#### 4.3.3 Effect of Tip Size, Concentration, and Surfactants on Reaction Acceleration

While the previously discussed microscopy experiments provided insight into nESI droplets produced under different conditions, the influence of these conditions on reaction acceleration has not been systematically explored. To investigate these effects, a series of experiments was performed which probe how these factors changed the observed acceleration in a model hydrazone formation reaction (see Scheme 4.1) (representative mass spectrum shown in

Figure 4.3 (a). The reaction solution was mixed and immediately loaded into nESI capillaries with outer diameters of 1, 5, or 20  $\mu\text{m}$ . The solutions were sprayed at various distances from the mass spectrometer inlet to observe reaction progress, as in several previous studies [5, 6, 10, 20]. The extent of reaction progress is given by the conversion ratio, defined as  $\frac{I_{238}}{I_{109} + I_{238}} \times 100$  where  $I_{238}$  is the intensity of the peak corresponding to the hydrazone product (**14**) and  $I_{109}$  is the intensity of the peak corresponding to phenylhydrazine (**12**). The resulting measurements (Figure 4.3 (b)) showed two trends. First, for measurements recorded at the same distance, the conversion ratio fell as the nESI emitter diameter increased. Second, all emitters showed increased conversion at longer distances, with the 1- $\mu\text{m}$  emitter having 73% conversion at 10 cm from the mass spectrometer inlet, while the

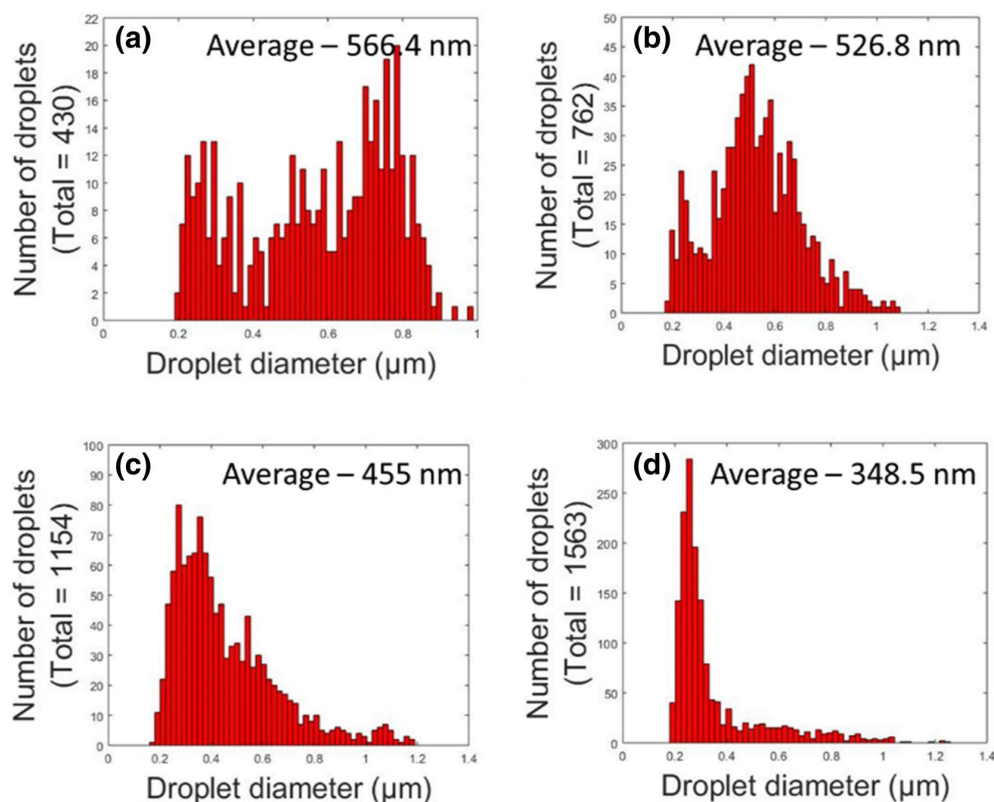


Figure 4.2 Effect of surfactant on droplet size distribution of a solution containing 100  $\mu\text{M}$  Rhodamine B in 9:1 methanol:glycerol and (a) no surfactant, (b) 0.1 mM surfactant, (c) 1 mM surfactant, and (d) 10 mM surfactant. All experiments were performed using a 20-ms pulse duration and 20- $\mu\text{m}$  nESI tip placed at a distance of 5 mm from the ITO coverslip

20- $\mu\text{m}$  emitter showed only 42% conversion. These results indicated that, all else held equal, smaller initial droplets resulted in greater conversion of reactants to products. It should be noted that droplet size effects have previously been observed in experiments comparing reactive desorption electrospray ionization (DESI) with nESI ionization.<sup>5</sup> Representative error bars have been added to Figure 4.3 (b) for the 5- $\mu\text{m}$  tip case. These error bars represent the standard error obtained from three separate measurements on different days. Note that, while error does increase with distance, the errors are much smaller than the size of the effects observed here.

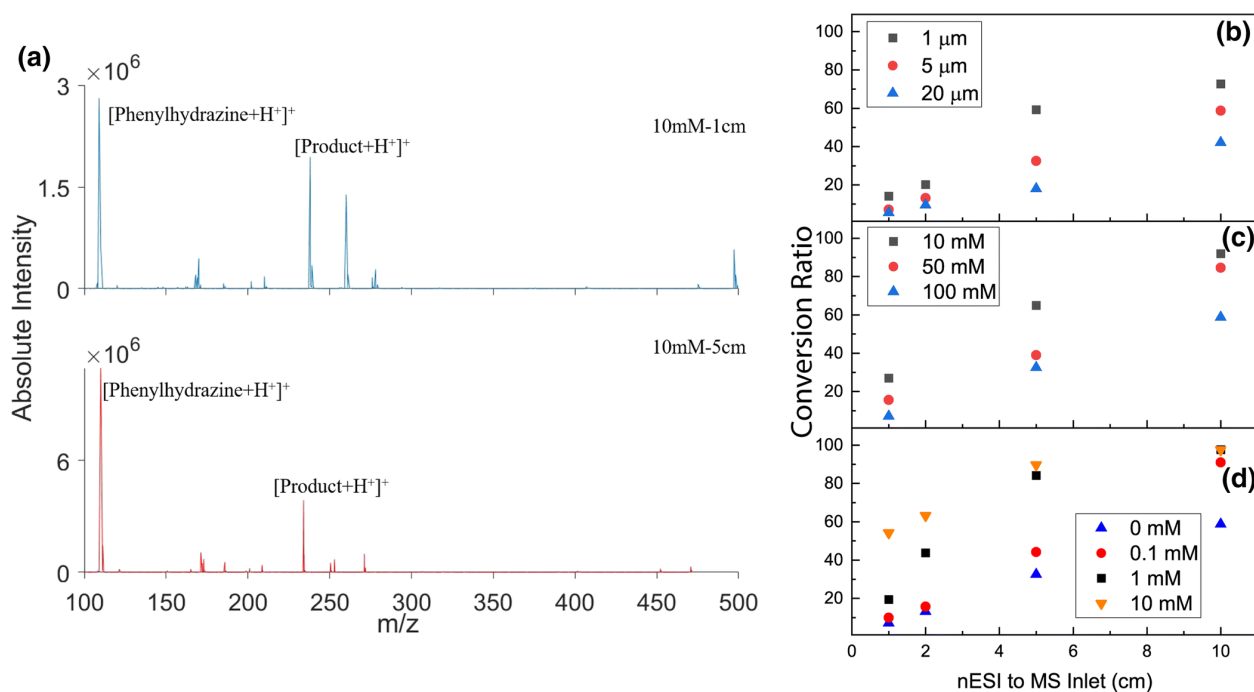


Figure 4.3 (a) Representative mass spectrum of phenylhydrazine-isatin reaction mixture shown at distances of 1 cm and 5 cm. Effect of (b) tip size (see legend) (c) 10, 50, and 100 mM phenylhydrazine concentrations (shown in legend) with constant isatin concentration and (d) different surfactant concentration (shown in legend) on conversion ratio as a function of emitter to MS distance. Note that the data in panels (b) and (c) were recorded with a 5- $\mu\text{m}$  emitter. Isatin concentration was 3 mM in all measurements here. Methanol was the solvent

Next, the influence of reagent concentration on the conversion ratio was investigated to examine the effect on reaction acceleration. The concentration of isatin was held constant at 3 mM in each measurement while the phenylhydrazine concentration was varied. The data (Figure 4.3 (c)), recorded using a 5- $\mu\text{m}$  O.D. nESI emitter, showed an inverse relationship between the conversion ratio and phenylhydrazine concentration. As much as 92% conversion was observed

for the 10 mM phenylhydrazine solution, and 85% in the 50 mM phenylhydrazine solution, although the maximum conversion observed in the 100-mM case is only around 60% for the 5- $\mu$ m emitter. Similar to the tip size study, the conversion ratio was found to increase with distance, although as concentration decreased, the conversion increased for the same distance. Given that phenylhydrazine is present in excess of the isatin in the above experiment, the effect of increasing both phenylhydrazine and isatin concentrations while maintaining a 1:1 ratio was studied. The data (shown in Table 4.1) indicate that for 10 mM phenylhydrazine/10 mM isatin, the rate is increased significantly relative to the 20 mM phenylhydrazine/20 mM isatin case, at both the distances used. Thus, it is apparent that, in this case, the effect of added concentration is, counterintuitively, to lower the observed rate.

Table 4.1 Concentration effects on conversion ratio of various phenylhydrazine + isatin solutions

Phenylhydrazine Conc (mM)	Isatin Conc (mM)	Conversion Ratio at 1 cm	Conversion Ratio at 5 cm
100	3	9.9	32.5
50	3	19.8	39.1
10	3	49.8	64.9
10	10	40.8	61.1
20	20	26.1	54.7

Finally, the influence of surfactant content in the nESI solution was studied. Here, the solutions were made with 0.1 mM, 1 mM, and 10 mM concentrations of CTAC as was done in the corresponding microscopy experiments. The experimental data, taken with a 5- $\mu$ m O.D. nESI emitter, are shown in Figure 4.3 (d). As surfactant concentration was increased, the conversion ratio also increased for an emitter positioned the same distance from the mass spectrometer inlet. Comparison of the 0.1 mM surfactant concentration data with the 0 M surfactant concentration data shows that, while the conversion for the two cases is similar with the nESI emitter close to the mass spectrometer inlet, the curves diverge at long distances, with the 0.1-mM sample showing nearly 100% conversion at 10 cm. In all cases, much higher conversion was observed

than in the surfactant-free case. To investigate the effect of surfactant *charge* on the reaction, the same experiments were performed using sodium lauryl sulfate, putatively a negatively charged surfactant. While the surfactant is likely protonated in the acidic environment of the droplets here, it still stands in contrast to the positive charge of the CTAC surfactant above. It was observed that, for 1 mM and 10 mM concentrations (Table 4.1), the reaction was accelerated by a greater degree than in the CTAC case. While the main effect of surfactant is, we believe, to increase the droplet fission rate, this data indicates that electrostatic effects (which have been shown to be significant in small droplets)<sup>85</sup> from the surfactant molecules may also play a role in the effects observed here. The reactivity of bulk solutions with and without SLS (Table 4.2) shows that the reaction proceeds slightly slower with surfactant compared with the no surfactant case.

Table 4.2 Bulk reaction of phenylhydrazine (100 mM) + Isatin (3 mM) with and without surfactant. Note the lower initial and final conversion ratios for the reaction with surfactant.

Reaction	Conversion ratio at 1 minute	Conversion ratio at 60 minutes
No Surfactant	27	78
+ 1 mM SLS	10	55

To understand why these factors (droplet size, phenylhydrazine concentration, and surfactant concentration) influenced the observed reaction rate, their effects on the electrospray process and droplet dynamics must be understood. While open questions remain about the mechanism of reaction acceleration in microdroplets, it is now clear that the increased reaction rates observed in confined volumes are due, in part, to accelerated reactions that occur at the surface of the droplet.<sup>31, 33, 34</sup> Reagent species located in this region have significantly different solvation environments than those in bulk, meaning that certain species may be stabilized or destabilized at the interface,<sup>82, 86</sup> leading to changes in the reaction potential energy surface compared with the bulk case. Thus, the rate constant at the surface may be significantly different than the rate constant in bulk solution. Since the rate constants at the bulk and surface are weighted by the

concentrations of molecules in those regions, any increase in surface concentration to bulk concentration ratio can have an outsized effect on the observed reaction rate.

First, the effect of tip size (and by extension the initial droplet size) is considered. For a spherical droplet, the ratio of surface area to droplet volume increases by  $\frac{3}{r}$ , where  $r$  is the radius of the droplet. Thus, as the droplet size is decreased, the “bulk-like” portion of the droplet decreases relative to the volume of the surface. To understand how this influences the relative concentrations of bulk and surface molecules, a model has been developed. Briefly, the model calculates the surface coverage of molecules using an equilibrium surface excess parameter,  $\Gamma$ ,<sup>87</sup> which represents the propensity of molecules to cover the surface, and to determine which portion of the molecules are adsorbed at the interface vs. being bulk solvated. Details of the calculations are given below:

The solute of interest is defined by a surface excess term,  $\Gamma$  (taken here to be the value when the surface is saturated),<sup>□</sup> which is related to the effective area per molecule by the relation<sup>88</sup>

$$\sigma = \frac{1}{\Gamma N_A}$$

Where  $N_A$  is Avogadro’s number. This value is used to calculate the number of molecules on the surface by dividing the droplet surface area,  $A$  (calculated for each diameter using the standard spherical surface area equation), by  $\sigma$

$$N_{surface} = \frac{A}{\sigma}$$

The number of bulk molecules is given by the equation

$$N_{bulk} = C_{total}V_{total}N_A - N_{surface}$$

Where  $C_{total}$  and  $V_{total}$  are the total concentration of solute molecules and volume of the droplet respectively.  $V_{total}$  is calculated for each droplet diameter using the standard spherical volume formula. For the parameters in this paper  $N_{surface}$  did not exceed  $C_{total}V_{total}N_A$  under any condition. The surface concentration is given by

$$C_{surface} = \frac{N_{surface}/N_A}{V_{surface}}$$

Where

$$V_{surface} = 4\pi r^2 \Delta r$$

Where  $\Delta r$  is the surface layer thickness, and  $r$  is the droplet radius.

Similarly, the bulk concentration is given by

$$C_{bulk} = \frac{N_{bulk}/N_A}{V_{total} - V_{surface}}$$

The surface to bulk concentration ratio is defined as

$$\frac{C_{surface}}{C_{bulk}}$$

For the calculations in the main text, this value was evaluated for each droplet diameter.

For the droplet evaporation calculations, the droplet radius as a function of time for methanol droplets is evaluated by the method of Kebarle and Tang<sup>89</sup> as

$$r = r_0 - \frac{\alpha v p^0 M}{4\rho RT}$$

Where  $r_0$  is the initial droplet radius,  $v$  is the average molecular velocity of the solvent (as a gas),  $p^0$  is the solvent vapor pressure,  $M$  is the solvent molecular mass,  $R$  is the gas constant,  $\rho$  is the density of the solvent, and  $\alpha$  is the condensation constant.

For methanol, this equation becomes (at 300 K)

$$r = r_0 - 1.2 \times 10^{-3}t$$

For the droplet fission calculations, the above relation between radius and time is employed with the Rayleigh relation

$$Q_{crit}^2 = 64\pi\epsilon_0\gamma r^3$$

where  $Q_{crit}$  is the critical charge and  $\gamma$  is the surface tension of the droplet solvent to calculate when the radius shrinks below the minimum value. Droplet sizes and charge after fission are calculated using the same parameters and assumptions as given in ref.<sup>90</sup>

It should be noted that this model assumes that the surface will be completely covered by molecules before bulk solvation becomes significant. The volume of the surface layer is determined by multiplying the surface area by a fixed thickness parameter  $\Delta r$ , chosen here to be 0.5 nm, which is on the order of the size of a methanol molecule. A schematic view of the parameters considered is shown in Figure 4.4 (a). Note that this model does not consider diffusion to and from the interface. The surface concentration/bulk concentration ratio for a droplet is plotted as function of droplet radius in Figure 4.4 (b). In this case, the solute concentration is taken to be 100 mM, equivalent to the concentration of phenylhydrazine in the tip size experiments. Although the surface excess parameter for this system (phenylhydrazine in methanol) is not known, this model still provides a qualitative picture of molecular partitioning in droplets for surface active species. Here, the  $\Gamma$  value ( $3 \times 10^{-7}$  mol/m<sup>2</sup>) was chosen to represent a case where molecules are preferentially adsorbed at the surface but have a significantly lower surface affinity than surfactant molecules, which typically have a surface excess on the order of  $10^{-6}$  mol/m<sup>2</sup>.<sup>91</sup> In Figure 4.4 (c), the droplet diameter is shown as a function of flight time, using Kebarle and Tang's model which assumes evaporation in the surface limit.<sup>90</sup> As the droplet radius shrinks, the droplet undergoes fission events, as dictated by the Rayleigh limit. The surface to volume ratio, taking into account evaporation and fission events, as a function of time is shown in Figure 4.4 (d), as calculated using the method of Kebarle and Tang.<sup>90</sup> In this model, a parent droplet undergoes fission into 20 smaller offspring droplets containing 15% of the total charge of the parent droplet and having 2% of the total mass of the parent when the droplet reaches 80% of its critical radius, as given by the Rayleigh relation. Here, the surface to volume

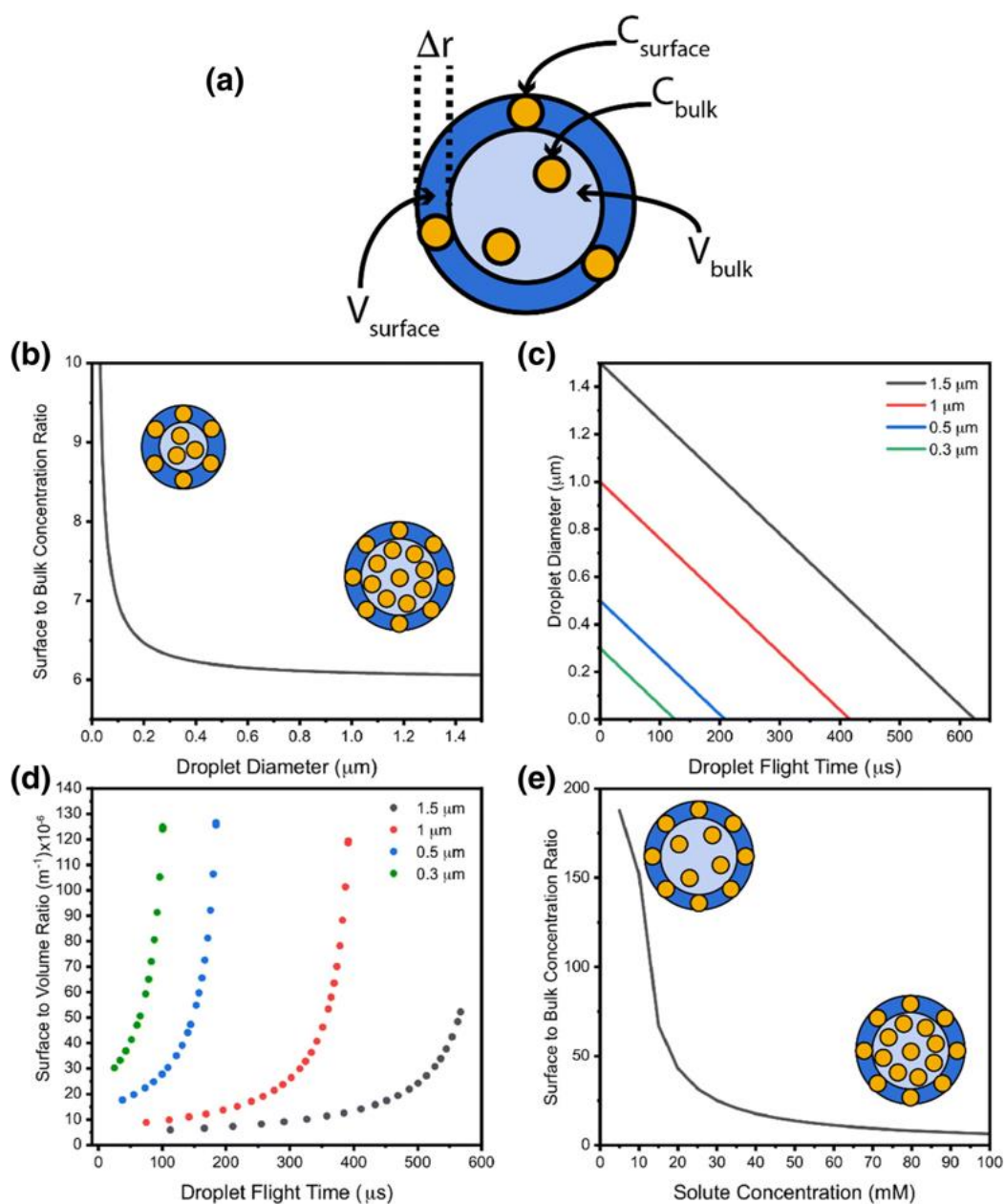


Figure 4.4 (a) Model of droplet with surface (dark blue) and bulk (light blue) volumes and differing surface and bulk concentrations (molecules represented by orange circles). (b) Relationship between droplet diameter and surface to bulk concentration ratio for a constant concentration of 100 mM solute. Droplet drawings show how volume and concentrations change with diameter. (c) Calculated droplet diameter as a function of droplet flight time. (d) Surface to volume ratio as a function of droplet flight time for different droplet sizes. (e) Surface to bulk concentration ratio for different solute concentrations in a 500-nm diameter droplet. Droplet drawings show the effect of solute concentrations schematically

ratio is evaluated at each droplet fission event as the sum of areas and volumes for the parent droplet and immediate offspring droplets. The droplets have an initial charge equal to 60% of the critical charge for the initial droplet size and have a surface tension equal to that for bulk methanol (22 mN/m).

Comparison of the experimental data with the calculated surface to bulk concentration ratios shows two effects. First, the smaller initial droplets have a slightly higher surface to bulk concentration ratio when they are created, implying that the initial rate is more reflective of the surface reaction rate for such droplets. Second, the calculated evaporation and fission dynamics show that as the droplets undergo evaporation after creation, the surface to volume ratio increases rapidly. This effect is particularly pronounced for the smallest droplets, which see a large increase in surface to volume ratio at earlier times than the large droplets. This observation, taken with the experimental data, suggests that the surface area and surface concentration are key contributors to the observed acceleration with decreasing droplet size. The same surface concentration model, with a surface excess value of  $3 \times 10^{-7}$  mol/m<sup>2</sup>, is used to evaluate how changes in the initial solution concentration influence the surface to bulk concentration ratio in droplets. The resulting curve, shown in Figure 4.4 (e) for a 500-nm diameter droplet, indicates that as concentration is decreased, the surface to bulk concentration ratio undergoes a steep increase. This result is reflective of the nature of surface coverage by solute molecules before bulk solvation occurs. The observed rate constant of the reaction depends upon the rate constant of the reaction in the bulk of the droplet and that at the surface of the droplet, as well as the concentrations in these regions. Reduction of the total concentration lowers the bulk concentration while keeping the surface concentration approximately constant, resulting in an increase of the observed (total) rate constant. Again, these results are qualitatively consistent with the experimental data, and further suggest the surface of the droplet is fundamentally important to the high observed reaction rates. This is consistent with the picture promoted by Zare through several recent studies<sup>31, 34, 74, 92</sup> and also with partial solvation as the underlying cause of acceleration, as we have proposed.<sup>33, 51</sup> Finally, the effect of surfactant on the reaction is considered in Figure 4.5. The influence of surface tension on droplet fission was evaluated using the droplet evaporation model described above. The calculations here use the surface tension of bulk methanol (22 mN/m) as the baseline and a surface tension of 19 mN/m as a representative case where surfactant is present. Note that the actual surface tension of this

solution is unknown. All calculations are for an initial droplet size of 750 nm with a total charge equal to 60% of the critical charge for the 22 mN/m case (15,239 charges). In the relative surface area graph (Figure 4.5 (b)), it is assumed that the smaller droplets formed during fission have evaporated between fission events, so the surface area is calculated only considering the parent and immediate offspring droplets.

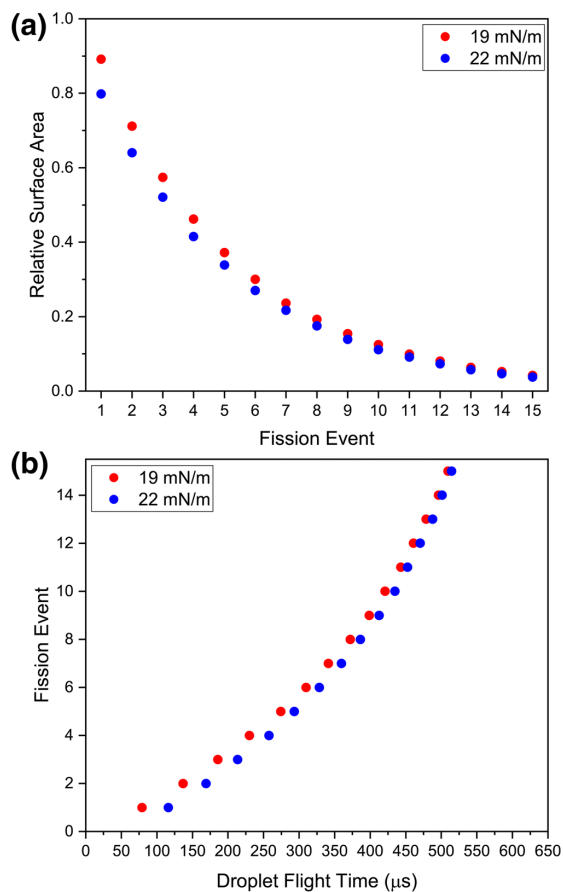


Figure 4.5 (a) Evolution of surface area with droplet fission event. The surface area at droplet creation is 1. (b) Fission event as a function of droplet flight time for 19 mN/m and 22 mN/m surface tensions

The surfactant molecules can influence the reaction in two ways. First, the surfactant molecules lower the surface tension of the droplets, which results in droplets undergoing Coulomb fission earlier than when no surfactant is present, creating more surface area (Figure 45). This effect is clearly observed in the surfactant microscopy data. The second effect is displacement of reagent molecules from the surface by surfactant molecules which would have the opposite effect. At

first glance, it is unclear which effect should dominate in a nESI spray. However, each Coulomb fission event results in the creation of multiple droplets which increase the total surface area, lessening the effect of the surfactant coverage. It is clear from examining Figure 4.5, along with the microscopy data, that the effect of surfactant is primarily to decrease the flight time needed for a droplet to undergo fission, which then results in a higher total surface area at a given time compared with the surfactant-free case. Thus, the dynamic nature of nESI droplets serves to overcome the surface excluding effects of surfactants, further enhancing the reaction rate compared with the no surfactant case. This result stands in contrast with studies of reaction acceleration in Leidenfrost levitated droplets where it has been shown that addition of surfactant to the droplet results in a reduction of the acceleration, implying that exclusion of molecules from the surface of the droplet reduces the rate.<sup>50</sup> Note, however, the Leidenfrost droplets do not fission so the data are entirely consistent.

#### **4.4 Applications of ambient focusing in reaction acceleration**

With the establishment of the main facts concerning reaction acceleration, attention can turn towards accelerating reactions on a preparative scale. Several examples already exist in the literature which demonstrate synthesis on the 10's of milligram scale.<sup>9, 29</sup> One strategy, posited here, is to deposit electrosprayed material onto a collection surface as done in some of the earliest experiments that used acceleration for synthesis<sup>93</sup> but now using a focusing electrode or aperture to increase ion currents. Note that well focused beams (~ 5 mm) of ions can be generated in the open air by the use of DC potentials in ellipsoidally shaped electrodes.<sup>94</sup> An even more straightforward method for producing focused ion beams is to direct the nESI plume through an aperture either floated or held at ground to give a spot up to 10× smaller than the aperture the beam was passed through.<sup>95</sup> We observed the effect of focusing on reaction acceleration at a distance of 5 cm from the nESI emitter to the mass spectrometer inlet using both an ellipsoidal electrode, similar to that discussed in ref.,<sup>51</sup> and a 15-mm diameter aperture. In both cases, the electrodes were held at 3 kV, while the sprayer was held at 5 kV to allow sufficient signal for MS analysis. In the case of the ellipsoidal electrode, the emitter was positioned perpendicular to the MS capillary, thus preventing neutral species from being transported. The observed enhancement was similar to that observed by spraying at a 5 kV potential from 5 cm without the use of the electrode. This suggests that focusing itself does not influence the observed degree of

reaction acceleration, meaning that the ellipsoidal electrode setup could be employed for surface patterning. Similarly, the aperture experiment showed similar conversion ratios to the case where no aperture was used. Position of the aperture between the MS inlet and nESI emitter did not influence the observed conversion ratio.

#### **4.5 Conclusions**

In this study, the influence of droplet size, reagent concentration, and surfactant concentration is considered. The evaporative dynamics of microdroplets produced by nESI were followed by super resolution splash microscopy. It was found that over a distance of 6 mm, droplets of methanol undergo significant shrinkage due to evaporation and that the addition of surfactant results in droplet size distributions weighted towards smaller droplets than without surfactants. The influence of these effects, in addition to that of reagent concentration and initial droplet size, was tested on the hydrazone formation reaction. Experiments show that smaller droplets lead to increases in reaction rate, and that a lower concentration of reagent molecules similarly increases the rate. These effects are indicative of a surface reaction occurring in the nESI droplets. Experiments with varying concentrations of surfactant molecules further indicate that smaller droplets enhance reaction rates. The role of diffusion to and from the interface in changing local concentration remains to be determined. No significant changes in acceleration were observed to be associated with ambient ion focusing.

## CHAPTER 5. SCREENING OF THE SUZUKI CROSS-COUPLING REACTION USING DESORPTION ELECTROSPRAY IONIZATION IN HIGH-THROUGHPUT AND IN LEIDENFROST DROPLET EXPERIMENTS

Portions of this chapter have been published in the Journal of the American Society for Mass Spectrometry as the article “Iyer, K., Fedick, P., Wei, Z., Avramova, A., Cooks, R.G. (2019) Screening and acceleration of Suzuki cross coupling reaction in desorption electrospray ionization and Leidenfrost droplets. *J. Am. Soc. Mass Spectrom.* (2019) 30: 2144. <https://doi.org/10.1007/s13361-019-02287-3>”

### 5.1 Introduction

The Suzuki cross-coupling reaction<sup>96</sup> is one of the most widely used reactions in pharmaceutical science.<sup>97</sup> The formation of a carbon-carbon bond by coupling a boronic acid with an organohalide was first reported in 1979.<sup>98,99</sup> The carbon-carbon bond is formed with the aid of a metal catalyst, most commonly a palladium complex, although other metals have been utilized.<sup>100, 101</sup> Similar to other metal-catalyzed reactions, including the Negishi<sup>102</sup> and Heck<sup>103</sup> reactions, this metal-catalyzed reaction has been well studied and the acceleration of the chemical reactions using catalysts is well documented.<sup>104</sup> A relatively new form of reaction acceleration is available through the use of thin films or microdroplets to confine reagents.<sup>31, 33, 77, 105</sup> Reaction acceleration in charged microdroplets was reported in 2006,<sup>106</sup> and it has since been applied to a number of reactions including the Claisen-Schmidt condensation,<sup>73</sup> the Katritzky transamination,<sup>7</sup> hydrazone formation,<sup>32</sup> BOC-deprotection,<sup>107</sup> cycloadditions,<sup>75</sup> and even the formation of gold nanostructures.<sup>78</sup> A number of different ionization sources have been used to generate droplets of various sizes to study reaction acceleration.<sup>29</sup> They include electrospray,<sup>6, 108</sup> nano-electrospray,<sup>32, 49</sup> paper spray,<sup>7, 50</sup> easy ambient sonic-spray,<sup>107</sup> desorption electrospray,<sup>5</sup> and theta tip spray.<sup>75</sup>

Although the mechanism of reaction acceleration is not completely understood, the underlying factors are clear. The degree of desolvation of the droplet, and hence the surface/volume ratio of the droplet, is a contributing factor and it points to increased rate constants for reactions at the interface.<sup>51</sup> As seen in the Hantzsch synthesis, when the spray source was moved further away from the mass spectrometer inlet, product formation was found to increase, in part, due to increased desolvation of the droplets and consequent increases in reagent concentrations<sup>49</sup> but also because

of the greater contribution from the surface over the bulk forms of the reaction. Unusual pH values at interfaces may also play a role in acceleration of reactions in confined volumes. The generation of thin films on a substrate has also been shown to be accompanied by reaction acceleration. The mechanism of thin film acceleration likely combines the above factors.<sup>9</sup> Thin films and sprayed droplets systems have been used to generate milligram amounts of product per minute and they can be useful in determining new reaction pathways as well as performing synthesis on a small scale.<sup>22, 28</sup>

Reaction acceleration in droplets can be used to guide chemistry at scale, and it can also be leveraged to acquire chemical information in a high-throughput format, for example, using a DESI-MS high-throughput system.<sup>22, 51</sup> This system utilizes DESI as an ambient ionization technique for analysis of the products formed in secondary microdroplets. The time scale available in these experiments is such that highly accelerated reactions in microdroplets must be involved. In preliminary work, the Suzuki cross-coupling reaction was explored using DESI. Briefly, four inorganic bases were screened using an aryl bromide as the reagent.<sup>22</sup> Other metal-catalyzed systems have been studied previously in accelerated microdroplets, including copper-catalyzed C–O and C–N coupling reactions that were performed by both electrospray and paper spray.<sup>29</sup> To calculate the reaction rate acceleration factor, the ratio of the intensity of the product ion to the intensity of the reactant ions for the accelerated system is divided by the same ratio for the bulk system<sup>109</sup> using the following equation.

$$\text{Reaction rate acceleration} = \frac{\left( \frac{\text{Intensity of product ion}}{\text{Intensity of reactant ion}} \right)_{\text{Accelerated system}}}{\left( \frac{\text{Intensity of product ion}}{\text{Intensity of reactant ion}} \right)_{\text{Bulk system}}}$$

It is important to note this definition assumes that the two reactions are run for the same period of time and the ion intensity ratio must be corrected for differences in ionization efficiency although these effects are often quite small and this is not done in the present study. Leidenfrost effect<sup>8</sup> produces levitated droplets<sup>80</sup> and represents another technique for generation of droplets in which reaction acceleration can be studied. The Leidenfrost effect occurs when a liquid droplet is levitated on its own vapor cushion when dropped onto a surface that is at a significantly higher

temperature than the liquid's boiling point.<sup>110</sup> The vapor cushion creates an insulating layer which prevents the liquid from boiling away rapidly. The droplet can therefore be maintained at a constant volume through the continuous replenishment of evaporated solvent. A number of reactions including the Katritzky transamination,<sup>8</sup> hydrazone formation, Claisen-Schmidt condensation, and the synthesis of diazepam have been explored previously using Leidenfrost levitation.<sup>8, 111, 112</sup> More recently, Li et al. utilized the Leidenfrost effect to accelerate pharmaceutical degradation.<sup>22</sup> In this study, we report the use of a high-throughput DESI screening system<sup>22</sup> (Figure 5.1) to screen reaction conditions (reagents, bases, stoichiometry) for the Suzuki cross-coupling reaction. Separately, we used Leidenfrost droplets to accelerate reactions with product analysis by nano-electrospray ionization (nESI) operated using conditions that do not cause reaction acceleration. A total of eight reactions utilizing different starting materials were tested using the DESI screening system and the Leidenfrost method (Schemes 5.1, 5.2 and 5.3). Each set of reactions was performed with three different bases as well as without base being added.

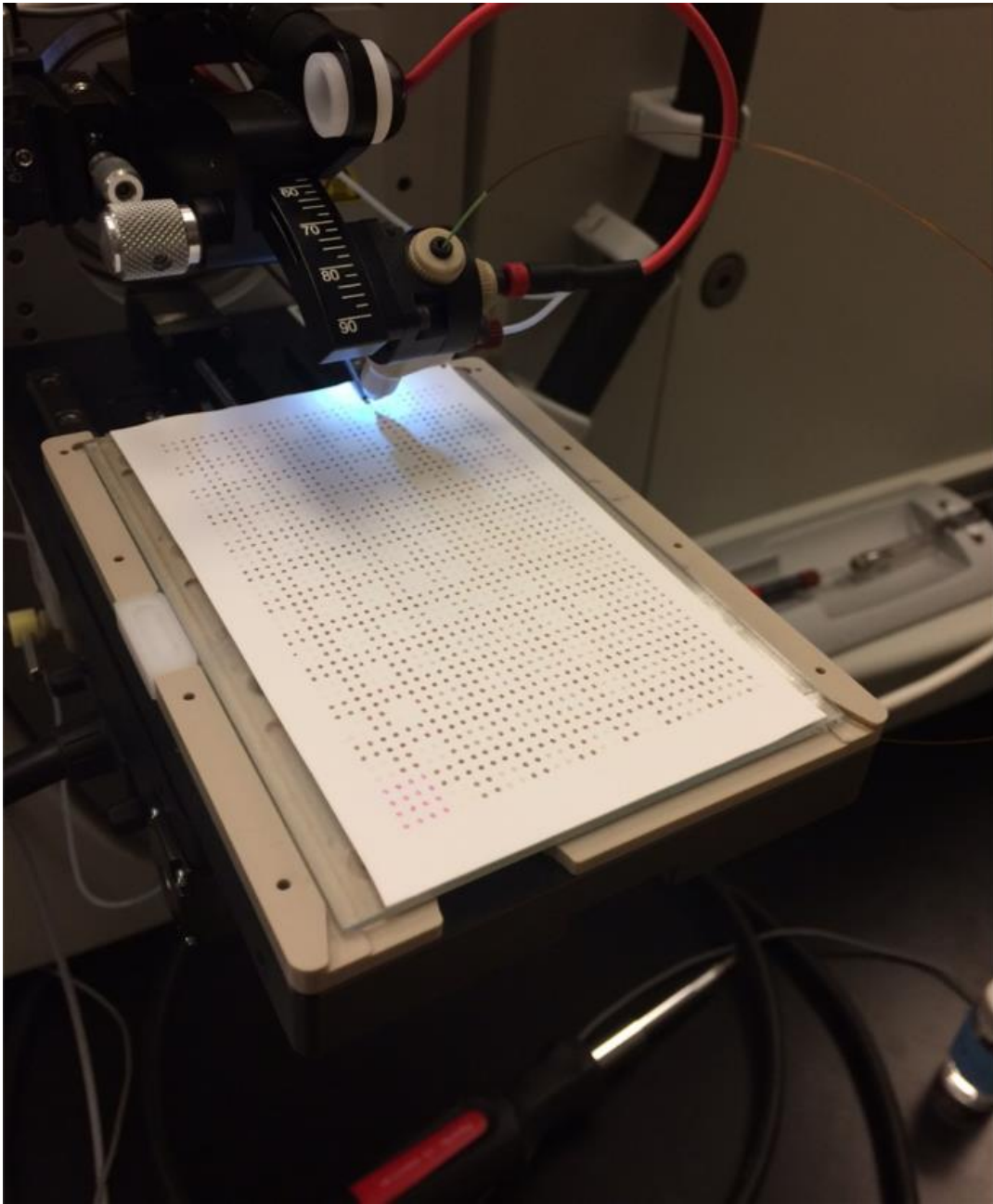
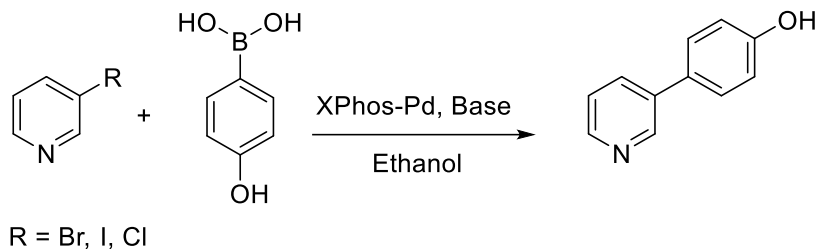
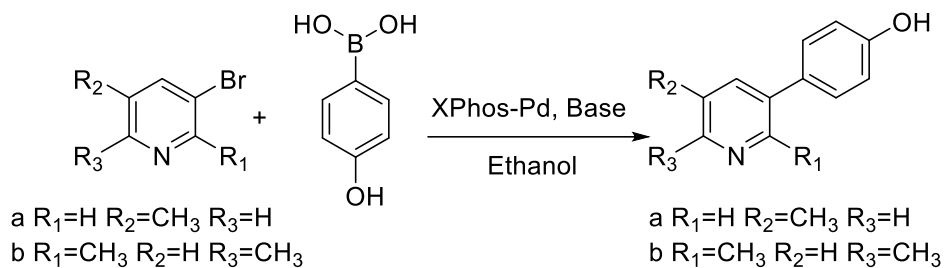


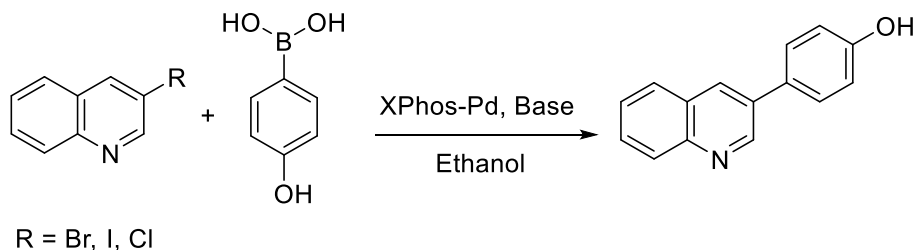
Figure 5.1 Photograph of the desorption electrospray ionization (DESI) setup



Scheme 5.1 Suzuki cross-coupling between meta-substituted pyridines 3-bromopyridine (**15**) 3-iodopyridine (**16**) and 3-chloropyridine (**17**) with 4-hydroxyphenylboronic acid (**18**) to form 4-(pyridin-3-yl)phenol (**19**)



Scheme 5.2 Suzuki cross-coupling between substituted meta-substituted bromopyridines 3-bromo-5-methylpyridine (**20**) and 3-bromo-2,6-dimethylpyridine (**21**) with 4-hydroxyphenylboronic acid (**18**) to form 4-(5-methylpyridin-3-yl)phenol (**22**) and 4-(2,6-dimethylpyridin-3-yl)phenol (**23**).



Scheme 5.3 Suzuki cross-coupling between meta-substituted quinolines: 3-bromoquinoline (**24**) 3-iodoquinoline (**25**) and 3-chloroquinoline (**26**) with 4-hydroxyphenylboronic acid (**18**) to form 4-(quinolin-3-yl)phenol (**27**)

## 5.2 Experimental

### 5.2.1 Chemicals

XPhos Pd G3, 1,8-diazabicyclo[5.4.0]undec-7-ene, 4-hydroxyphenylboronic acid, 3-bromopyridine, 3-iodopyridine, 3-chloropyridine, 3-bromoquinoline, potassium ethoxide, tetrabutylammonium hydroxide, and anhydrous pure 200 proof ethyl alcohol were purchased from Sigma-Aldrich (St Louis, MO). Ethyl alcohol was used as the solvent system for all experiments. 3-Iodoquinoline was purchased from EnamineStore (Monmouth Junction, NJ), 3-chloroquinoline was purchased from Accela (San Diego, CA), 3-bromo-2,6-dimethylpyridine was purchased from Matrix Scientific (Columbia, SC), and 3-bromo-5-methylpyridine was purchased from Asymchem (Morrisville, NC). Leidenfrost reactions were conducted with 1a-c, 4a-b, and 6a-c at a concentration of 0.1 mM, 2 at 0.1 mM, XPhos-Pd G3 at 0.01 mM, and bases at 0.2 mM. Bulk experiments were conducted with all reactants at 20 times the concentrations of the Leidenfrost experiments.

### 5.2.2 Plate preparation for DESI-MS imaging

A Biomek i7 liquid handling system was used to prepare 96- and 384-well microtiter plates using robotic pipetting. For the 96-well plate, 30  $\mu$ L 4-hydroxyphenylboronic (0.5 M in EtOH) solution, 30  $\mu$ L aromatic halogen reagents (0.5 M in EtOH), 30  $\mu$ L Xphos-Pd G3 solution (0.05 M in EtOH), and 30  $\mu$ L base solutions (1 M in EtOH) were added to each sample well and mixed. To expand density from 96 to 384, each well was divided into four quadrants to test the concentration effect. Methyl orange dye was added at selected pixels to serve as a position beacon. The plate layout can be found in Figure 5.2. The 384-well plate was then remade on PTFE using a density of 1536 by a stamping pin tool. The reaction mixture in each well of the 384-well plate has four replicas in the final 1536 density plate used for DESI analysis.

### 5.2.3 DESI-MS screening

A commercial DESI source from Prosofia Inc. was used for analysis of the plate. A Thermo LTQ linear ion trap was used to acquire data. DESI-MS experiments were performed in negative ion mode over mass range  $m/z$  50–500. The DESI spray solvent was methanol with a flow rate

4  $\mu\text{L}/\text{min}$ . Sheath gas used was nitrogen at a pressure of 120 psi. Injection time was set to 10–15 ms for 1 microscan and mass scan time was set to 80 ms. The DESI moving stage speed was 4376  $\mu\text{m}/\text{s}$  (350- $\mu\text{m}$  step size). The commercial Prosolia 2D DESI stage control system in combination with Firefly software was used to convert data from Thermo format (.raw) to a format compatible with the BioMAP imaging freeware (.img). Ion images were then generated using BioMAP.

#### **5.2.4 Leidenfrost droplets**

The reaction mixture (1 mL) was mixed in a vial and dropped using a Pasteur pipette into a well of a porcelain spotting/color plate (Thomas Scientific, Swedesboro, NJ) atop a Fisher Scientific hotplate with a surface temperature 540 °C. The mixture was then allowed to levitate for about a minute so that the droplet could shrink to approximately 50  $\mu\text{L}$ . The Leidenfrost droplets were maintained at a constant volume of 50  $\mu\text{L}$  over the course of the 10 minute experiment by continuously adding solvent by a Harvard Apparatus PHD 22/2000 syringe pump (Holliston, MA) at 275  $\mu\text{L}/\text{min}$  (Figure 5.3). The solvent was delivered by a Popper and Sons Perfektum Micro-Mate Interchangeable 20 cc syringe (New Hyde Park, NY) outfitted with PEEK tubing 1/16" O.D.  $\times$  0.030" I.D. (IDEX Health and Science, Oak Harbor, WA). The PEEK tubing was held in place by a rubber stopper with a hole punched in the center. The PEEK tubing was attached to the syringe using a female luer adapter attached to a 10–32 male luer adapter, a one-piece fingertight 10–32 coned, for 1/16" O.D., and a stainless-steel union body true ZDV 0.062" through hole (IDEX Health and Science, Oak Harbor, WA). Products were examined by nESI using non-accelerating conditions. For all MS analysis pertaining to Leidenfrost droplets and bulk reactions, we used nESI under non-accelerating conditions. Although nESI produces droplets in which reaction acceleration can occur, we are able to choose conditions where we can avoid reaction acceleration to ensure that we are sampling the true product yields for the bulk and for the Leidenfrost experiments. This is done by placing a nESI emitter very close to the inlet of the MS (approximately 1 mm). This ensures that the droplets do not have significant flight times in air, preventing desolvation and hence not giving the droplet enough reaction time.

### 5.2.5 Mass spectrometry

Mass spectrometric analyses were performed in negative ionization mode on an LTQ ion trap (Thermo Fisher Scientific, San Jose, CA). The LTQ was operated using the following parameters: capillary voltage of  $-15$  V, capillary temperature of  $150$  °C, and a tube lens voltage of  $-65$  V. nESI was utilized at  $2.0$  kV. To construct the nESI tips, borosilicate glass capillaries ( $1.5$  mm O.D.,  $0.86$  mm I.D., Sutter Instrument Co.) were pulled to a tip using a Flaming/Brown micropipette puller (Sutter Instrument Co. model P-97, Novato, CA, USA) with an outer diameter of  $2$   $\mu\text{m}$ .

### 5.2.6 Results and discussion

Rapid DESI reaction screening was performed at rates that approached  $10,000$  reaction mixtures per hour to evaluate three bases for the Suzuki reaction, viz., 1,8-diazabicyclo[5.4.0]undec-7-ene (DBU), potassium ethoxide (EtOK), sodium ethoxide (EtONa), and the set of eight reagents listed in Figure 5.4. A control experiment without base was also performed. In addition to spotting different reaction mixtures for analysis, methyl orange was also spotted on the plate at regular intervals (Figure 5.2) as a positional reference. This was also done to ensure proper sample deposition using the pinning tool and reproducibility of each spot. Rhodamine is another common dye that is used as fiduciary marker; however, since the MS analysis was performed in the negative ion mode, methyl orange was more suitable. The high-throughput DESI-MS analysis was performed in an automated manner using methanol as the DESI spray solvent. Ion images were generated for each of the reaction spots on the plate using Biomap and this enabled a quick readout of the results. As seen from the heat map in Figure 5.2 (left), the deposition of reagents onto the PTFE slide was reproducible with no cross-contamination of reagents.

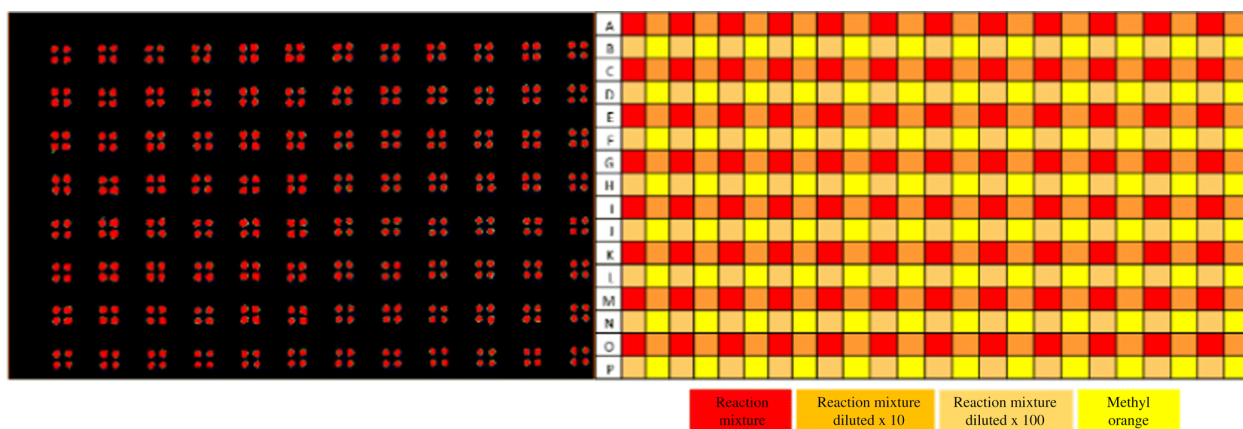


Figure 5.2 Plate layout for methyl orange and reaction mixtures (right). Biomap images of methyl orange ( $m/z$  304) array showing the reproducibility of the pinning tool (left). Plates are  $127 \times 85$  mm

Next, DESI-MS analysis was performed on the samples on the plate to evaluate the performance of three bases and eight reagents. Figure 5.4 indicates the reaction mixture layout for the different systems tested. Each pair of rows corresponds to a different starting material while the columns indicate the base that was used in the reaction. Each square contains the same reaction mixture pinned in replicates of four. Reaction mixtures were also spotted at different concentrations as indicated in Figure 5.3. The white squares in Figure 5.4 (right) are representative of wells that contain only methyl orange.

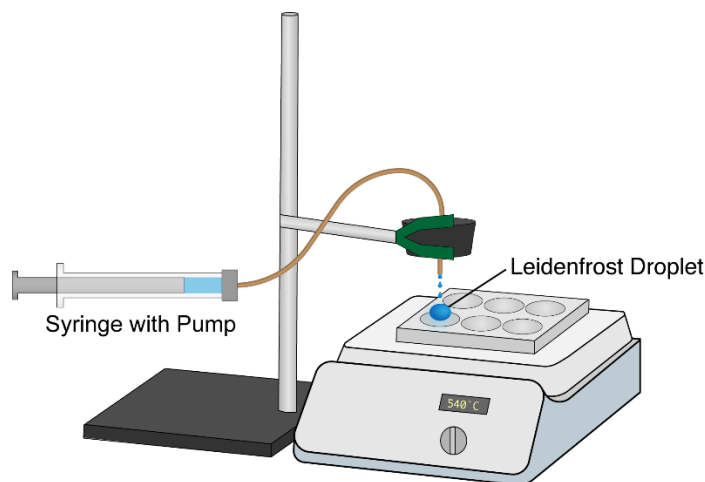


Figure 5.3 Leidenfrost apparatus

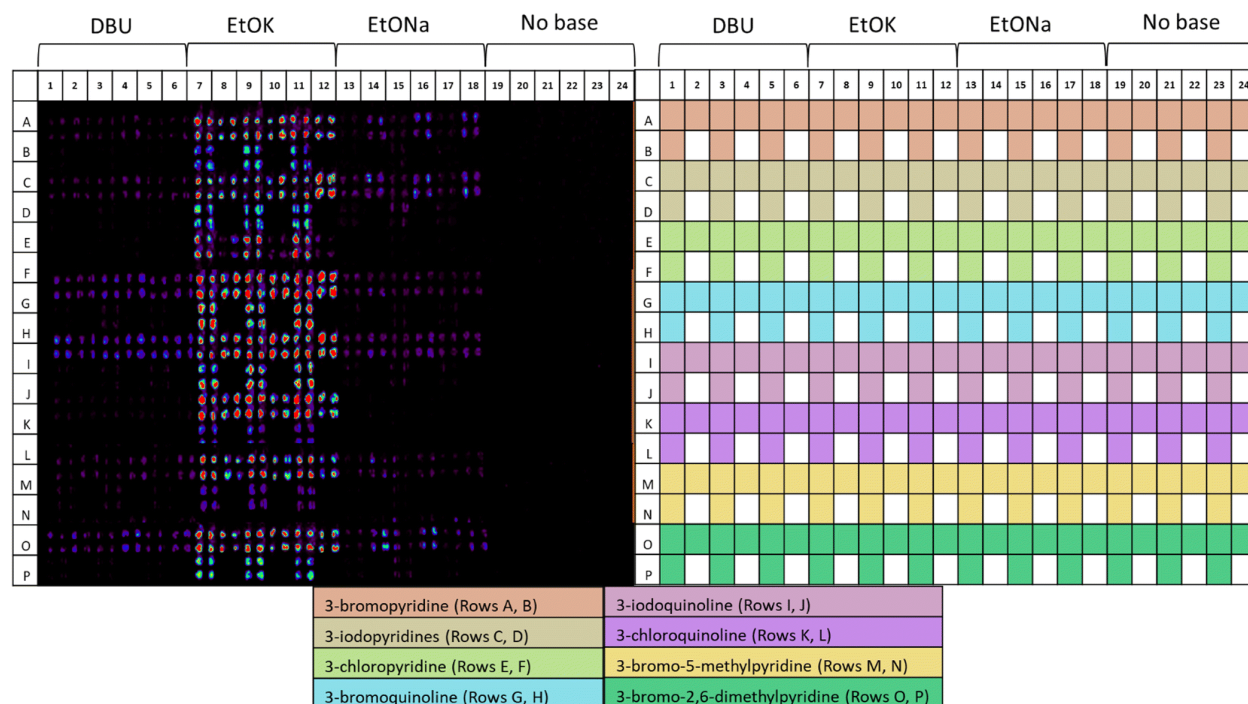


Figure 5.4 Reagent layout on the final reaction plate for the Suzuki reaction (right). Each pair of rows contains a different set of starting reagents in replicates. Rows A and B correspond to wells containing 3-bromopyridine (1a), rows C and D contain 3-iodopyridine (1b), rows E and F contain 3-chloropyridine (1c), rows G and H contain 3-bromoquinolin (6a), rows I and J contain 3-iodoquinoline (6b), rows K and L contain 3-chloroquinoline (6c), rows M and N contain 3-bromo-5-methylpyridine (4a), and rows O and P contain 3-bromo-2,6-dimethylpyridine (4b). White squares contain methyl orange as the positional marker. All reaction wells contain reagent 4-hydroxyphenylboronic acid (2) and catalyst but differ in the bases added. Columns 1–6 contain DBU, columns 7–12 contain EtOK, columns 13–18 contain EtONa and columns 19–24 have no base. DESI imaging heat map of the reaction plate for various products (left)—4-(pyridin-3-yl)phenol (3) at  $m/z$  170 (rows A–F), 4-(quinolin-3-yl)phenol (7) at  $m/z$  220 (rows G–L), 4-(5-methylpyridin-3-yl)phenol (5a) at  $m/z$  184 (rows M–N), and 4-(2,6-dimethylpyridin-3-yl)phenol (5b) at  $m/z$  198 (rows O–P). Each product was individually searched by the product  $m/z$  and then the data were overlaid onto a single figure

As seen in the heat map generated by Biomap (Figure 5.4, left), the base that generated the most product was EtOK for all reaction systems. EtONa and DBU did not perform as well and generated very little product as compared to EtOK. The wells without base did not show the generation of product in DESI-MS screening. Note that the different reagents generate different products; hence, each row of the heat map was processed separately in Biomap and the images were overlaid to generate one large heat map for the entire plate. Methyl orange signals are not displayed in the heat map for Figure 5.4 since it is used only a positional reference as has already been illustrated in Figure 5.3. With regard to trends in reagent reactivity and concentrations, the

heat map indicates that all substituted pyridines and quinolines have good reactivity even at lower concentrations. Figure 5.5 (left) shows the mass spectra for the coupling of 3-bromopyridine (**15**) with 4-hydroxyphenylboronic acid (**18**). These mass spectra were extracted from the data used to create the heat map. Using EtOK as the base results in almost complete conversion, while as it can be clearly seen that the reaction does not proceed without added base.

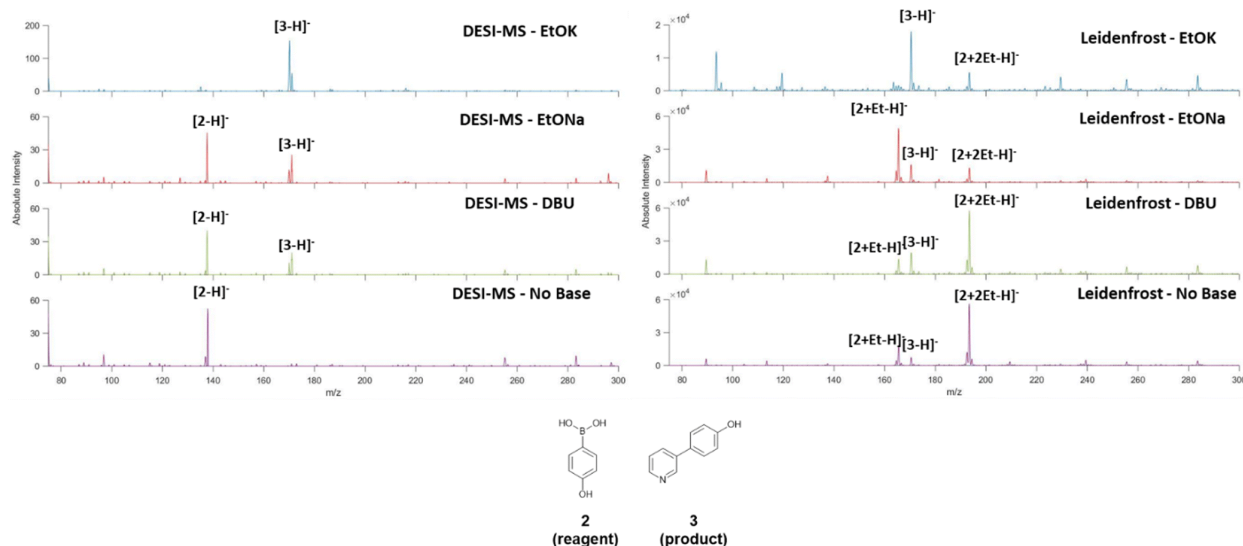


Figure 5.5 Mass spectra for the Suzuki cross-coupling reaction between 3-bromopyridine (**15**) with 4-hydroxyphenylboronic acid (**18**) from the DESI-MS experiment (left). Mass spectra for the Suzuki cross-coupling reaction between 3-bromopyridine (**15**) with 4-hydroxyphenylboronic acid (**18**) from the Leidenfrost experiment (right). Blue: mass spectrum of the reaction using EtOK as the base. Red: mass spectrum of the reaction using EtONa as the base. Green: mass spectrum of the reaction using DBU as the base. Purple: mass spectrum of the reaction without any base added. The “-Et” label in the mass spectra refers to ethoxylated peaks

Comparison of the DESI-MS results was also made with droplets generated by the Leidenfrost effect. The reaction was found to proceed to a greater extent using the brominated reagents as compared with the iodo- or the chloro- reagents. Figure 5.5 (right) shows the mass spectrum of the Suzuki cross-coupling of 3-bromopyridine (**15**) with 4-hydroxyboronic acid (**18**). These mass spectra were recorded after a 10-minute Leidenfrost experiment. As seen from the figure, EtOK again performed better as a base than did EtONa and DBU. However, the most interesting observation is that the reaction proceeded even in the absence of a base in the Leidenfrost droplets. The reason for the reaction in the Leidenfrost droplet is attributed to the basicity of the Leidenfrost droplet as demonstrated by Abdelaziz et.al.<sup>113</sup> The reaction perhaps did not proceed in the DESI-



To confirm the identity of the reported products, MS/MS confirmation was performed on the product ions of representative cases (Figure 5.6).

Table 5.1 Acceleration Factors for Different Substrates Reacting with 4-Hydroxyphenylboronic Acid in Leidenfrost Droplets

Substrate	Acceleration factors <sup>a</sup>		
	EtOK	EtONa	DBU
3-bromopyridine	239	124.2	71.6
3-iodopyridine	36.9	24.3	12.9
3-chloropyridine	N/A <sup>b</sup>		
3-bromoquinoline	183	116.7	68.9
3-iodoquinoline	37.9	20.4	13.6
3-chloroquinoline	N/A <sup>b</sup>		
3-bromo-5-methylpyridine	9.2	5.3	N/A <sup>b</sup>
3-bromo-2,6-dimethylpyridine	2.6	2.4	N/A <sup>b</sup>

<sup>a</sup>Acceleration factors reported in Table 5.1 are calculated using the ratios of the mass spectrometry signals of the products to those of the starting materials in the Leidenfrost droplet relative to the bulk. Each experiment was performed in triplicate

<sup>b</sup> No product formation

The reproducibility of acceleration factors in the Leidenfrost droplet was validated by performing each reaction in triplicate and this gave standard deviations of less than 3%. Table 5.1 shows the average acceleration factors for three 10-minute runs for each reagent. The trends in substrate reactivity and base performance matches well between the DESI-MS results and the Leidenfrost findings. Approximate acceleration factors are provided for DESI experiments in the Table 5.3 in

which the reaction time is on the order of a few msec. Note that a far better comparison of acceleration is made by measuring the ratio of the time needed to reach a particular product/reagent intensity ratio. The characteristic lifetime of a DESI droplet is on the order of a few milliseconds, compared to 10 minute for the Leidenfrost droplets, yet the experiments give very similar product ion abundances over a large set of compounds. In order to compare the AFs (including approximate acceleration factors) between the DESI-MS system and the Leidenfrost (LF) system, several factors need to be considered. Presented in Table 5.2, are product to reagent ratios for the Leidenfrost system at two and 10-minute time points, bulk systems – at room temperature and reflux and the DESI-MS system.

AFs for confined volume systems may be calculated in one of the following ways:

- (i) as a ratio of rate constants
- (ii) more simply, as the ratio of the mass spectrometric intensities of the product to the reagent intensities for a confined volume system divided by the same ratio for a bulk system both recorded after the same fixed time.<sup>109</sup> This is the method by which we calculate acceleration factors for the LF system.
- (iii) as a ratio of the times required for a confined volume system and a bulk system to achieve the same yields for the product

Table 5.2 Product to reagent ratios for the Leidenfrost system (two and 10-minute time points), bulk - room temperature and refluxed and the DESI-MS system

Reagent	Base	Product to reagent ratios				
		Leidenfrost		Bulk		DESI-MS
		2 min	10 min	Room temperature	Heated	Room temperature
3-bromopyridine	EtOK	0.62	3.13	0.01	0.01	1.26
3-iodopyridine		0.38	2.01	0.01	0.05	0.19
3-chloropyridine						
3-bromoquinoline		0.47	1.50	0.00	0.01	0.66
3-iodoquinoline		0.15	0.55	0.01	0.01	0.30
3-chloroquinoline						
3-bromo-5-methylpyridine		0.02	0.10	0.01	0.01	0.05
3-bromo-2,6-dimethylpyridine		0.05	0.26	0.04	0.10	0.10
3-bromopyridine	EtONa	0.07	0.35	0.01	0.00	0.57
3-iodopyridine		0.05	0.25	0.01	0.01	0.08
3-chloropyridine						
3-bromoquinoline		0.01	0.59	0.00	0.01	0.24
3-iodoquinoline		0.01	0.32	0.01	0.02	0.10
3-chloroquinoline						
3-bromo-5-methylpyridine		0.02	0.08	0.01	0.02	0.04
3-bromo-2,6-dimethylpyridine		0.02	0.07	0.00	0.03	0.00
3-bromopyridine	DBU	0.15	0.76	0.01	0.01	0.26
3-iodopyridine		0.03	0.19	0.00	0.02	0.02
3-chloropyridine						
3-bromoquinoline		0.07	0.30	0.00	0.00	0.05
3-iodoquinoline		0.04	0.21	0.00	0.02	0.01
3-chloroquinoline						
3-bromo-5-methylpyridine		0.01	0.04	N/A <sup>a</sup>	N/ <sup>a</sup>	0.05
3-bromo-2,6-dimethylpyridine		0.00	0.01	N/A <sup>a</sup>	N/A <sup>a</sup>	0.05

For the DESI-MS system, however, nominal AFs have to include a correction factor in order to make a direct comparison with the Leidenfrost system which involves a longer time and (of less importance) a higher temperature.

From Table 5.2, it can be seen that for all values,

$$\frac{Bulk (hot)}{Bulk (RT)} = 2 \text{ (approximately)}$$

Equation 1

Additionally,

$$AF \text{ for the LF system} = \frac{LF (hot)}{Bulk (hot)}$$

Equation 2

$$\text{Nominal AF for the DESI - MS system} = \frac{DESI - MS (RT)}{Bulk (RT)}$$

Equation 3

Comparing the 2 AF values from Table S1,

$$\frac{\text{Nominal AF (DESI)}}{AF (LF)} = 1.3 = \frac{DESI - MS (RT)}{Bulk (RT)} \times \frac{Bulk (hot)}{LF (hot)}$$

Equation 4

Substituting values from equation 1 into equation 4, we have,

$$\frac{DESI - MS (RT)}{LF (hot)} \times 2 = 1.3$$

Equation 5

Hence,

$$\frac{DESI - MS (RT)}{LF (hot)} = 0.65$$

Equation 6

The true ratio of AFs is by definition the ratio of the times needed to achieve the same product to reagent ratio in the confined volume and bulk systems. DESI-MS reactions occur on the order of a few milliseconds, while the LF system is a 10-minute reaction. The ratio in Equation 6 can be approximated to 1 and hence comparing the times required by both systems to achieve the same product to reagent ratio, it can be said that the DESI-MS system is  $6 \times 10^5$  times faster than the LF system. Additionally, if heating had been incorporated into the DESI-MS experiments, this factor would be even greater. The very large difference in the two acceleration factors is not surprising since it is well established that droplet size has a very large *inverse* effect on reaction rate. Droplet sizes for the LF experiment are much larger (~5 mm) when compared to DESI-MS droplets (2-4  $\mu\text{m}$ )<sup>21</sup>. This provides a much higher surface to volume ratio for DESI-MS droplets making this a far faster system. Table 5.3 below lists the approximate AFs for the Suzuki cross coupling reaction in DESI-MS microdroplets; they are approximate AF's because ionization efficiencies have not been corrected for and because the reaction in the DESI-MS droplets occurs in times on the order of a few microseconds whereas the bulk reaction takes place in 10 min.

In keeping with other conclusions, this indicates orders of magnitude (ca. 5 orders) difference between reaction rates in these systems. Given that there is already a one to two orders of magnitude acceleration in the Leidenfrost droplets, the magnitude of the acceleration in DESI microdroplets is clearly very large.

Recently, Fumagalli et al. reported the anomalously low value of the dielectric constant of water at interfaces, explaining how confined and interfacial water have different surface properties when compared to bulk water.<sup>116</sup> It seems possible that a similar effect may be seen with solvents in confined volume systems such as Leidenfrost droplets. The vapor-liquid interface is a dynamic system since the heat supplied to the droplet constantly cycles the vapor in and out of the droplet. In contrast, the bulk system does not exhibit the surface effects as seen in the droplet; hence, the rate of product formation in bulk systems is much lower when compared to Leidenfrost droplets

Table 5.3 Approximate acceleration factors for different substrates reacting with 4-hydroxyphenylboronic acid in DESI-MS microdroplets <sup>a</sup>

Substrate	Approximate acceleration factors <sup>*</sup>		
	EtOK	EtONa	DBU
3-bromopyridine	1.2 x 10 <sup>8</sup>	6.0 x 10 <sup>7</sup>	3.0 x 10 <sup>7</sup>
3-iodopyridine	1.8 x 10 <sup>7</sup>	9.2 x 10 <sup>6</sup>	3.1 x 10 <sup>6</sup>
3-chloropyridine	Cannot be determined <sup>b</sup>		
3-bromoquinoline	9.3 x 10 <sup>7</sup>	5.4 x 10 <sup>7</sup>	2.5 x 10 <sup>7</sup>
3-iodoquinoline	2.3 x 10 <sup>7</sup>	7.3 x 10 <sup>6</sup>	5.3 x 10 <sup>6</sup>
3-chloroquinoline	Cannot be determined <sup>b</sup>		
3-bromo-5-methylpyridine	5.5 x 10 <sup>6</sup>	2.5 x 10 <sup>6</sup>	Cannot be determined <sup>b</sup>
3-bromo-2,6-dimethylpyridine	1.6 x 10 <sup>6</sup>	1.2 x 10 <sup>6</sup>	Cannot be determined <sup>b</sup>

<sup>a</sup> Acceleration factors reported in Table S2 are calculated using the ratios of the mass spectrometry signals of the products to those of the starting materials in the DESI-MS relative to the bulk at room temperature. They are then corrected for the time difference between the DESI-MS experiment and the bulk experiment, a factor of 6 x 10<sup>5</sup>. <sup>b</sup> No product formation in bulk and hence approximate acceleration factors cannot be determined.

### 5.3 Conclusions

High-throughput screening using DESI-MS imaging was shown to allow successful screening of bases for the Suzuki cross-coupling reactions in agreement with an earlier study.<sup>22</sup> The conditions generated by DESI-MS screening were successfully transferred to reaction systems that used droplets generated by the Leidenfrost technique for accelerating metal-catalyzed cross-coupling reactions and corresponding trends were observed in these larger droplets. The largest measured reaction acceleration for the Suzuki cross-coupling was that for the 3-bromo substituents. Additional substituents on the ring severely hindered reaction acceleration perhaps due to steric effects. While not all reactions were accelerated, the trend in reactivity in the DESI-MS system remained consistent with the trend observed in the Leidenfrost droplets and in the bulk solutions. In addition, the agreement of coupling rate with previously reported literature and the

reproducibility of the Leidenfrost droplet acceleration using the continuous solvent addition as a means of maintaining droplet size demonstrates that Leidenfrost droplets could be a potential screening tool for new reactions to complement the use of high-throughput DESI-MS. Complete conversion to product in the Leidenfrost droplet can be achieved by increasing the levitation time. This is particularly useful when dealing with potentially less favorable reactions with slower reaction kinetics.

## CHAPTER 6. ION MANIPULATION IN AIR USING 3D-PRINTED ELECTRODES

Portions of this chapter have been published in the Journal of the American Society for Mass Spectrometry as the article “Iyer, K., Marsh, M.B., Capek, G.O., Schrader, R.L., Tichy, S., Cooks, R.G. (2019) Ion Manipulation in open air using 3D-printed electrodes. *J. Am. Soc. Mass Spectrom.* (2019). <https://doi.org/10.1007/s13361-019-02307-2>”

### 6.1 Introduction

The ability to manipulate ions in air is of great importance in mass spectrometry (MS) due to the widespread adoption of electrospray ionization (ESI)<sup>11</sup> and of ambient ionization techniques<sup>1-4, 117</sup> as the ionization methods of choice for many users. Typically, ions are generated at atmospheric pressure and allowed to propagate into the vacuum region of the mass spectrometer where they are focused and analyzed. However, the efficiency of ion transmission is often poor due to the spreading of ions from the spray and the small orifices used in mass spectrometers, leading to rejection of most of the ion signal.<sup>35, 118</sup> Additionally, in order to aid desolvation and so produce gas phase ions, ion sources need to operate either at significant distances from the instrument or they must be operated with a heated sheath gas.<sup>119</sup> While ion funnels may assist in solving this problem, they can only operate under reduced pressure and their operation requires relatively complex radio frequency (RF) voltages.<sup>36</sup> Thus far little has been done to create avenues for manipulating ions under ambient conditions (i.e. in the open air) to improve their transmission to the mass spectrometer.

Ion optical simulations under reduced pressure continue to be a uniquely valuable resource in the development of unique MS instrumentation.<sup>39, 120</sup> It is less common to attempt to use ion optical simulations to investigate ambient pressure ion manipulation or ion focusing. An early observation of this type was made when performing ambient ion soft-landing experiments, where it was observed that after passing through an aperture, ions became focused into a spot much smaller than the aperture.<sup>121</sup> This result was consistent with an earlier observation by Hayn and coworkers during the deposition of organic molecules at atmospheric pressure.<sup>122</sup> A similar effect was observed when placing a transmission electron microscopy (TEM) grid in front of an ESI source,

the ion beam being focused by a factor of ten compared to the size of the TEM grid holes.<sup>123</sup> Experiments using ellipsoidally shaped electrodes as well as curved geometries,<sup>38, 94</sup> indicated that ions could be transported over significant (>1 cm) distances in air while maintaining focus using only DC potentials. Despite this early work many questions remain as to the mechanism of ion focusing in air, the usefulness of which is just beginning to be realized. Presented here is a series of experiments utilizing 3D-printed focusing devices which seek to provide insight into the mechanism of ambient pressure focusing. Electrode designs were generated using AutoCAD software and then imported as stereo lithography (.stl) files into Simplify 3D, a ‘slicing’ program used to break up the model into ‘layers’. The layers are imported as gcode into the operating system of the 3D printer. Fused deposition modeling (FDM) was used to construct three sets of electrodes – (i) conical, ellipsoidal, and cylindrical electrodes (all conic section electrodes), (ii) both conductive and non-conductive simple aperture electrodes, and (iii) curved electrodes with complex geometries (straight, chicane and curved). 3D-printing offered a quick and inexpensive way to construct and render various electrode designs.<sup>124</sup> Ion simulations were performed concurrently using the statistical diffusion model (SDS) in SIMION 8.1. To test the performance of the focusing devices, cross-sections of ion packets focused by the different electrodes were recorded using an IonCCD camera.<sup>125</sup> Additionally, the electrodes were coupled to an Agilent Ultivo Triple Quadrupole MS and mass spectrometric measurements were performed using a mixture of tetra alkyl ammonium (TAA) bromide salts.

## **6.2 Experimental**

### **6.2.1 Focusing electrode designs**

Three sets of devices were designed using AutoCAD software. The first set – conic section electrodes – are comprised of three geometries, cylindrical, conical and ellipsoidal. Each electrode has an opening of 30 mm, an internal length of 50 mm, and holes on one side spaced in 5 mm increments from the opening to the back of the object (Figure 6.1 A, B). The second set of electrodes – the conductive and the non-conductive apertures (not shown in the figure) are simple 2D objects 3, 9, 12, and 15 mm in diameter. The six individual electrodes which comprise the complex geometry electrodes have a curvature of 15 degrees with 20 mm diameter openings

(Figure 6.1, C-E). To generate these electrode systems, the conic electrode components are arranged to give different geometries.

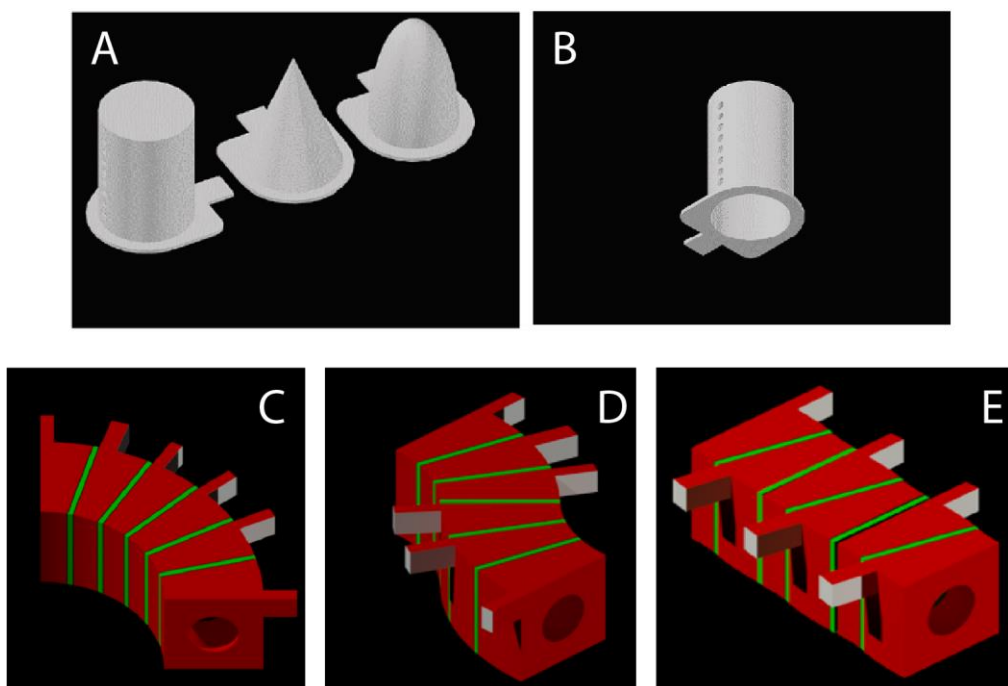


Figure 6.1 (A) Conic section electrodes (50 mm long) in cylindrical, conical and ellipsoidal geometries. (B) Cylindrical electrode showing the holes on the side spaced 5 mm apart and having diameters of  $\sim 1$  mm to allow for the placement of a nanoelectrospray emitter. (C, D, E) Curved, chicane, and straight complex electrodes (openings here are 20 mm).

### 6.2.2 3D-printing

The conic section electrodes were printed at 265 °C using a modified Prusa i3 printer (Makerfarm, UT, USA) from polyethyleneterephthalate glycol (PETG) polymer containing multiwalled carbon nanotubes (3DXTech, MI, USA). High extrusion temperatures are necessary as lower extrusion temperatures produce non-conducting electrodes. The print surface was covered in polyimide tape and heated to 70°C to increase bed adhesion. The conductive apertures and complex geometry electrodes were printed using a Mendel Max 3 (Maker's Tool Works, OK, USA) printer with carbon doped conductive polylactic acid (PLA) filament (Proto-pasta, WA, USA). To check the conductivity of the printed electrodes, a voltage of 3kV was applied to one end of the electrode and the voltage at the other end was measured. All electrodes showed no measurable decrease in voltage across the object, indicating that they had adequate conductivity. Non-conductive apertures

were printed using non-conductive PLAPLA using a MendelMax 3 printer with extrusion temperature of 210 °C and heated glass bed at 50 °C with non-conductive PLA/Polyhydroxyalkanoate (PHA) filament (ColorFabb, Belfeld, Netherlands)

### **6.2.3 IonCCD current measurements**

The cross-sections of the ion packets focused by the different electrodes were recorded using an IonCCD camera (OI Analytical, TX, USA) operated in air. The IonCCD consists of a detector array, composed of 2,126 21  $\mu\text{m}$ -wide titanium nitride pixels, each 1.5 mm in height. The pixel separation is 3  $\mu\text{m}$ , giving an effective resolution of 24  $\mu\text{m}$  per pixel. Incoming ions are neutralized on the TiN pixels, giving rise to the current recorded by the IonCCD software. For experiments involving the conic section electrodes, the current was recorded over a time of 100 ms. For the aperture electrodes and the series electrodes, electrospray beam images were profiled by scanning the IonCCD in the horizontal dimension in 0.65 mm steps with the pixel row held constant in the vertical position. IonCCD images were processed by subtracting the signal with the electrospray off (background signal) from the IonCCD signal recorded with the electrospray and focusing electrode. The intensity of features in the IonCCD spectrum is given in digital numbers (dN). Each dN unit corresponds to 100 elementary charges. Exact parameters for these experiments, including electrode and emitter voltages, are discussed in the results and discussion section

### **6.2.4 SIMION simulations**

Simulations of ion trajectories were performed using the statistical diffusion simulation (SDS) model in SIMION 8.1. Briefly, SDS is a computationally efficient method for simulation of collisions of ions with background gas. Diffusion of ions is simulated by random jumps of the ions at each time step. The jump distance is determined by collision statistics calculated for the ion. The SDS algorithm has been previously validated for simulations of atmospheric ion transport and ion mobility.<sup>126</sup> The simulations here only consider the ions as fully desolvated and do not consider the dynamic droplet evolution process which nESI sprays undergo after droplet creation.

## 6.2.5 Mass spectrometry

MS measurements were performed using an Agilent Ultivo triple quadrupole mass spectrometer. External nanoelectrospray ionization (nESI) was used to generate ions. A platinum wire served as the electrode. nESI emitters were pulled using borosilicate glass capillaries (0.86 mm ID, Sutter Instruments, CA, USA) using a micropipette tip puller (Model P-97, Sutter Instruments, CA, USA). The nESI tips had an outer diameter of  $\sim 5$   $\mu\text{m}$ . For nESI measurements, analyte solution was loaded into the pulled glass capillary using a gel loading tip (Bio-Rad, Hercules, CA). DC potentials were applied to the Pt wire using an external power supply. For nESI measurements, the source and electrodes (if any) were placed directly in front of the inlet of the MS and at a specific distance from it. The capillary in the source of the instrument was held at a positive set point of 100 V and the DC potential applied using an external power supply. For measurements using the nESI emitter alone, spectra were recorded at distances of 5 cm and 60 cm from the inlet. For measurements using the focusing electrodes, the nanospray emitter was placed orthogonally to the ion optical path of the instrument and inside the conic section focusing electrode using the holes on its side. The orthogonal orientation of the emitter in the electrode was chosen so as to decrease the flux of neutral species into the ion beam. For all measurements using the conductive electrodes, the nESI emitter was always held at a higher potential than the electrode. The entire electrode setup (Figure 6.2) was placed in front of the MS inlet at different distances and spectra were recorded using the same source conditions described above. Analyte used was a solution consisting of a mixture of tetraalkylammonium (TAA) bromide salts (C2, C3, C4, C5, C6, C7, C8) at 20  $\mu\text{M}$

## 6.3 Results and discussion

### 6.3.1 Conic section electrodes

To understand how electrode geometry, and therefore the electric field, influences ion trajectories, a series of measurements was recorded with each set of electrodes using the IonCCD detector. The first set of measurements, performed using the electrodes of conical, ellipsoidal, and cylindrical profiles, examined how emitter position within the electrode influences the size and intensity of the exiting ion packet. For IonCCD measurements, the nESI emitter was held at 4.5 kV while the electrode was held at 3 kV. The IonCCD was held 15 mm away from the electrode exit for all three cases.

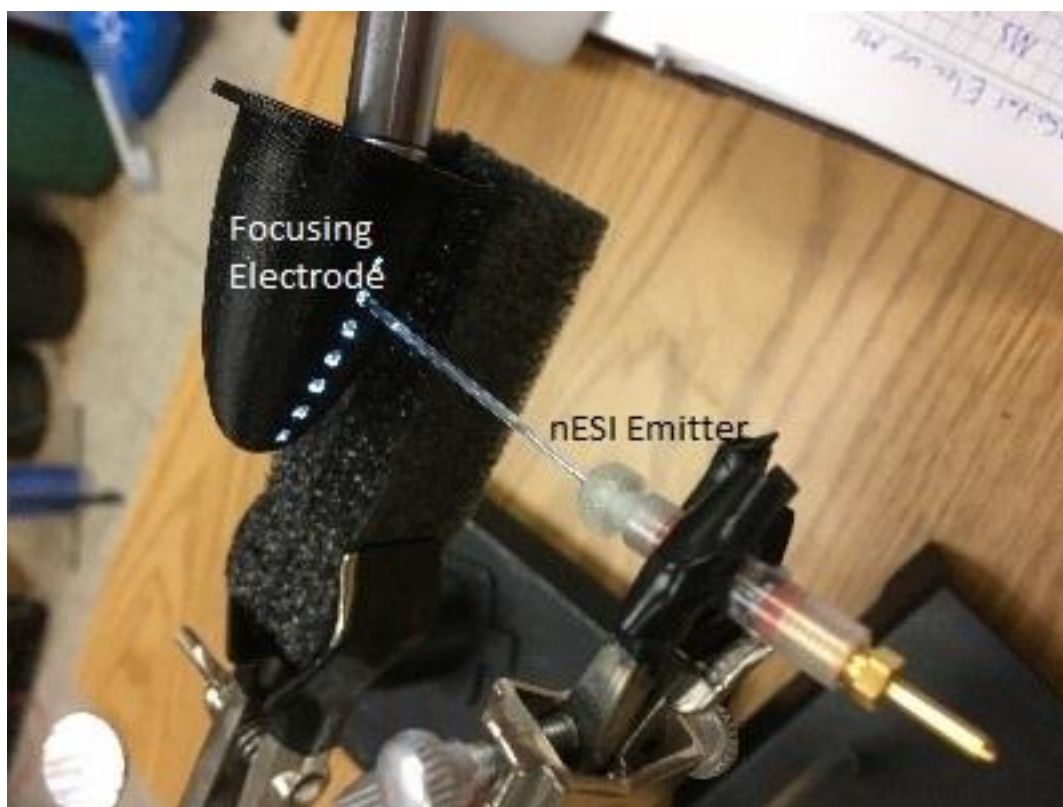


Figure 6.2 Ellipsoidal electrode setup. Note that a flashlight is used to illuminate the holes on the outside of the electrode.

The resulting data (Figure 6.3) show two trends. First, in general, as the emitter is placed farther from the electrode exit, the peak recorded at the IonCCD becomes narrower. However, a significant decrease in the ion intensity was also observed. The difference in intensity is attributed to microdroplet evaporation throughout flight with scattering of the desolvated ions. Second, the conical electrode gives significantly better focusing than the ellipsoidal or cylindrical electrodes at a given distance. However, the cone displayed no measurable signal when the emitter was inserted into the hole 35 mm from the exit (Hole 7), which is attributed to the narrowness of the electrode at that location. Such effects are suggestive of a strong geometrical effect on the focusing observed. The asymmetry in the peaks is due to the nanospray emitter influencing the ion packet, as seen in ref<sup>94</sup>. The ion current, measured at the IonCCD as a function of peak full width half mass (FWHM) is shown for all measurements in Figure 6.2.

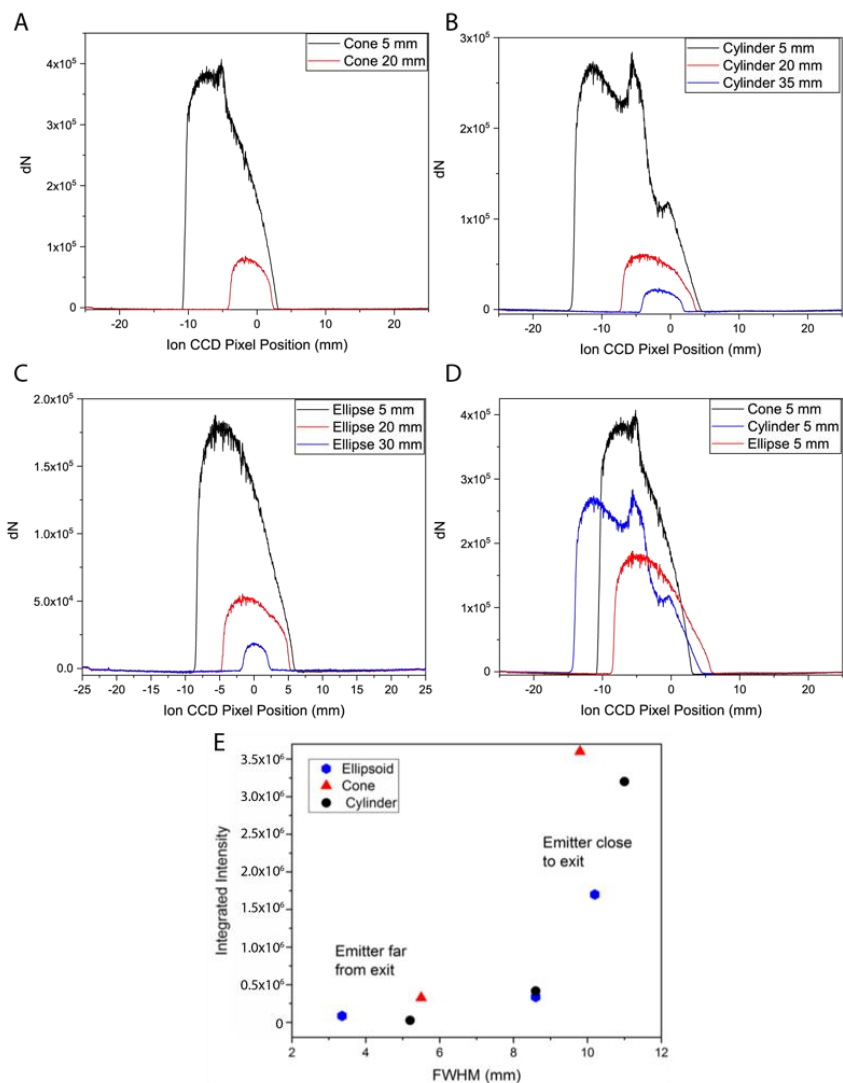


Figure 6.3 Cross sectional beam images recorded with an IonCCD camera for the conical (A), cylindrical (B), and ellipsoidal (C) focusing electrodes. nESI sprayer was held at 4.5 kV while the focusing electrode was held at 3kV. (D) Ion beam cross section at 5 mm for each electrode.

(E) Summary of focusing data for each electrode and emitter distance recorded in these experiments.

For MS measurements, the nESI emitter was held orthogonally to and just inside the focusing electrode using the holes on the side. Mass spectra were recorded at close distances (5 cm) and long distances (60 cm) with and without the focusing electrode. For all experiments, the nESI emitter was always held at a higher voltage than the focusing electrode. When the nESI emitter is placed orthogonally at a distance of 5 cm without the focusing electrode, the cations of all salts – C2 to C8 - are observed in the spectrum, while at farther distances, only C2 to C6 salts are observed

(Figure 6.4 (A)). The voltage on the nESI emitter for these experiments was 2 kV. There is also a significant drop in the signal intensity as the nESI emitter is moved farther away. When the focusing electrode is introduced in the 60 cm experiment, higher mass TAAs are recovered, accompanied by an order of magnitude increase in intensity in signal as seen in figure 3B. For these results the nESI emitter was held at 3 kV while the focusing electrode was held at 2 kV. The resultant potential difference is 1 kV. We observed a proportional change in signal intensity when the potential difference was increased, attributed to the increase in kinetic energy that accompanies the increased voltage on the emitter. The increased transmission of high mass ions is also evidence of a long range effect resulting from ion focusing. In other words, ions which are focused in the electrode appear to maintain focus over the entire transmission distance, although some losses in intensity are observed. This effect is illustrated in Figure 6.5. For the MS results shown in Figure 3B, the nESI emitter was inserted into Hole 1

### 6.3.2 Aperture electrodes

The next set of experiments looked at focusing of ions through printed 2D apertures, building upon previous work in the group<sup>95</sup> in which electrosprayed ions were observed to undergo focusing by a factor of 10x through small apertures such as TEM grids. In these experiments, a 5  $\mu\text{m}$  O.D. nESI emitter was held 7.5 mm from the aperture, which in turn was held 7.5 mm from the IonCCD detector. The IonCCD was scanned over the ion cloud to observe focusing in both the vertical and horizontal directions. First, a series of non-conductive apertures are considered. Shown in Figure 6.6 are the IonCCD images for the spray plume when using 3 mm, 9 mm, 12 mm, and 15 mm apertures. As the aperture size shrinks, so too does the size of the focused spot. All spots have FWHM values which are significantly smaller than is the aperture. The focusing achieved here is attributed to surface charging, viz. the buildup of charge on the aperture due to ion deposition. After a critical amount of charge is deposited, ions are repelled from the surface towards the electrode center, where they form a collimated beam. Next, conductive apertures of the same sizes were explored. The data collected for a range of voltages and aperture sizes is given in Figure 6.7. It is immediately apparent that, as the voltage on the aperture increases, the ion beam FWHM decreases. In addition, as the aperture size decreases the FWHM decreases at constant voltage. Finally, comparison of the 15 mm aperture data at 1 kV with 2 kV and 1.5 kV spray potentials

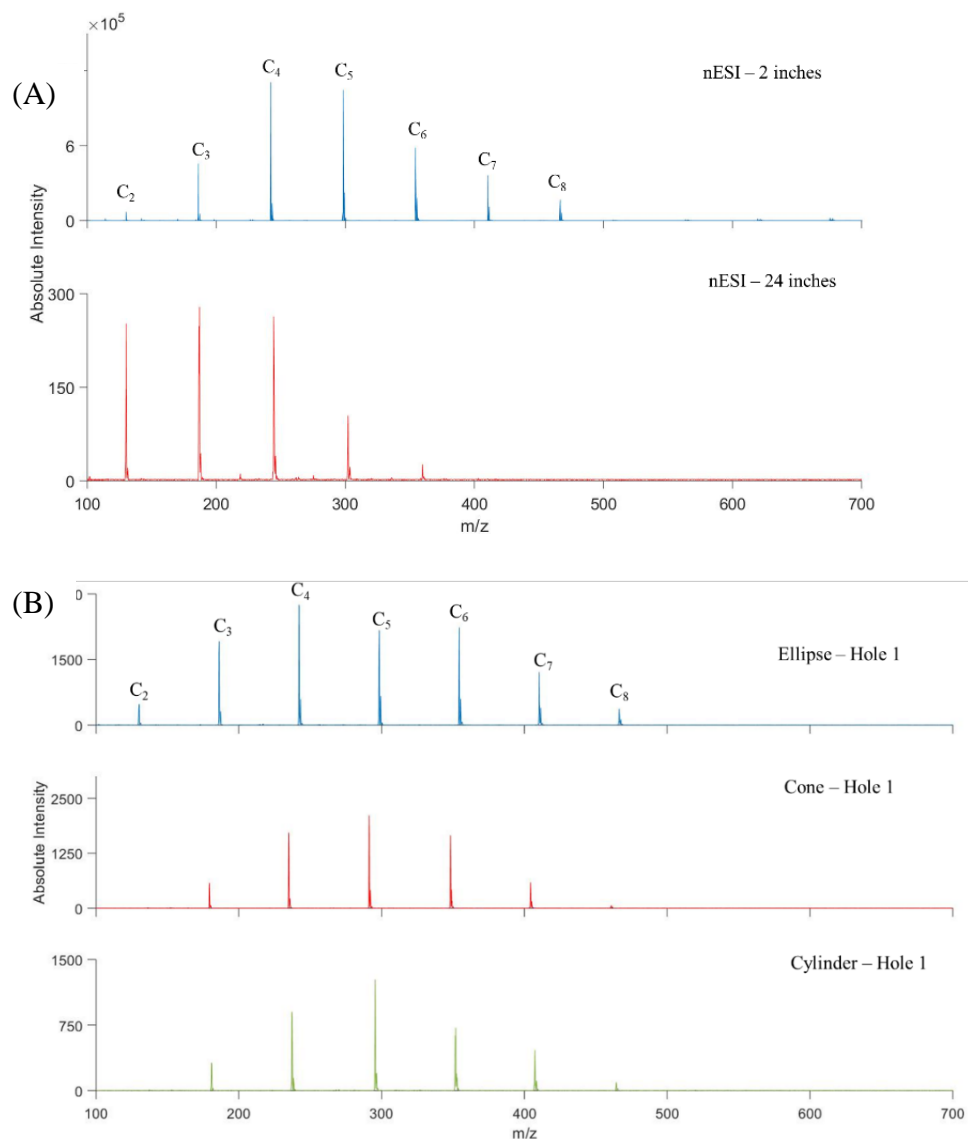


Figure 6.4 (A) Mass spectra showing profiles of a mixture of TAA salts. Top blue – Mass spectrum of the sample at 2 inches. Bottom red – Mass spectrum of the sample at 60 cm.(B) Mass spectra showing profiles of a mixture of TAA salts using focusing electrodes (Hole 1) at a distance of 60 cm. Top blue ellipsoidal, middle red – conical, bottom green – cylindrical. The nESI emitter is held at 3 kV while the focusing electrodes were held at 2 kV

shows that the beam FWHM decreases with increasing difference between aperture potential spray potential. The spatial irregularities in the IonCCD images for the apertures, both non-conductive and conductive, are attributed to the asymmetric nature of the nESI plume that is being focused (see Figure 6.6 (A)). The regions of irregular intensity are smoothed over as the microdroplets from the spray are reduced in size. For example, the conical electrodes and the cylindrical electrode

IonCCD images show an irregular structure at 5 mm distance, but a relatively smooth structure at longer distances.

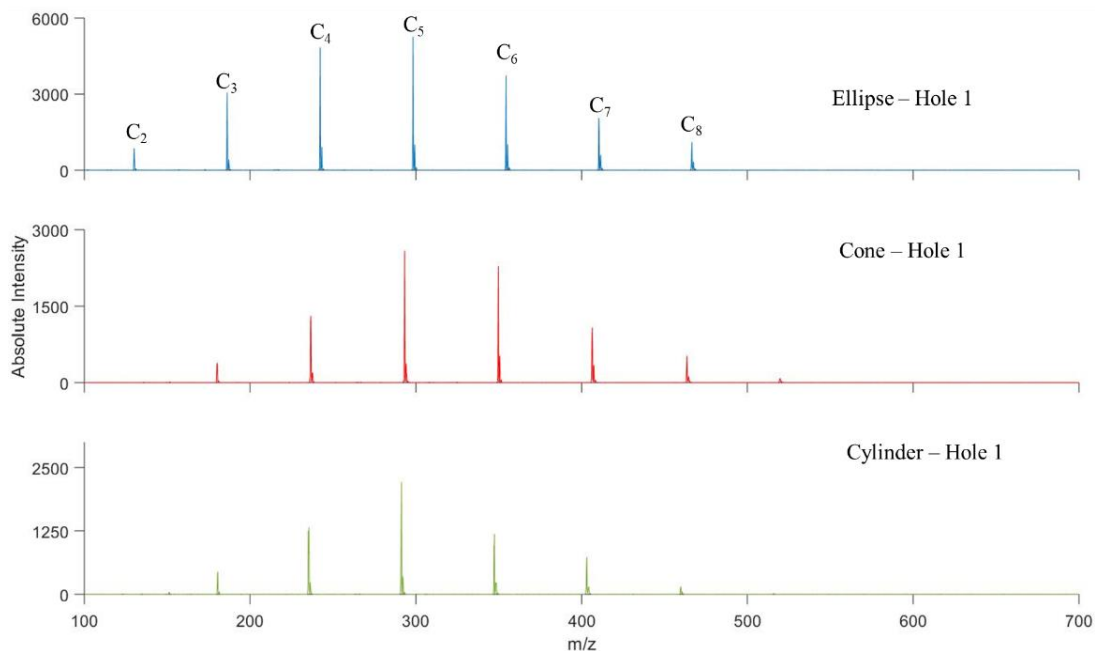


Figure 6.5 Mass spectra showing profiles of a mixture of TAA salts using focusing electrodes (Hole 1, nearest to the exit of the electrode) which is at a distance of 24 inches from the MS. Top blue – ellipsoidal, middle red – conical, bottom green – cylindrical. The nESI emitter is held at 4 kV while the focusing electrodes were held at 2 kV

### 6.3.3 Complex electrodes

Finally, to build upon the work using the simple geometries just described, focusing and transport in complex electrodes was studied. Here, three electrode geometries were explored using the same six electrodes. The first, a curve, the second, a chicane, and the third, a straight path. The electrodes were arranged with the emitter approximately 5 mm into the first electrode and the IonCCD located 7.5 mm from the exit of the electrode. In these experiments a mixture of four TAAs (C<sub>3</sub>, C<sub>4</sub>, C<sub>6</sub> and C<sub>8</sub>) was chosen for study. The emitter in all cases was held at 6 kV, while the electrodes were floated with the first electrode at 3 kV or 4 kV, descending in either 500 V (for 3 kV) or 666 V (for 4 kV) steps.

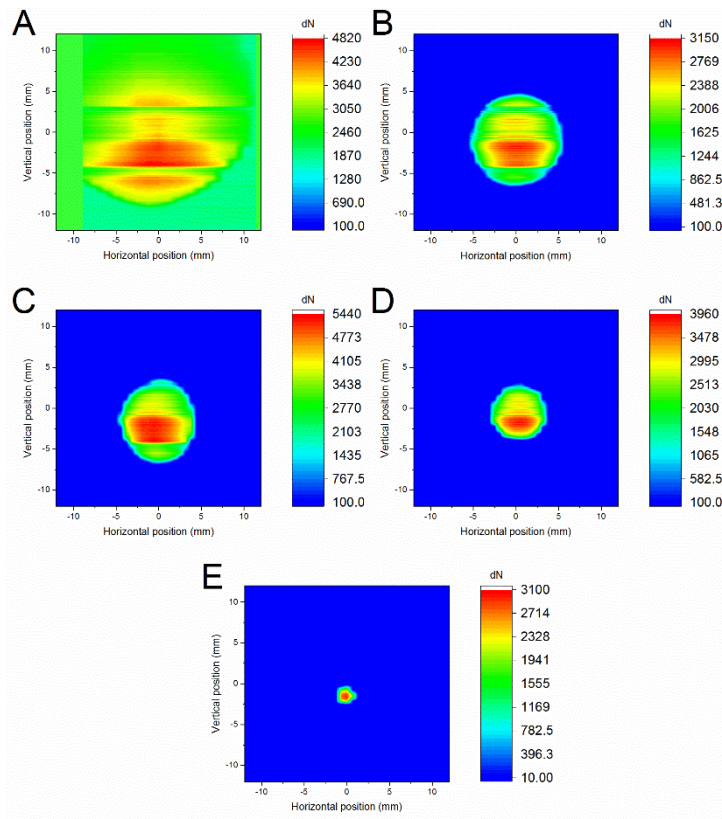


Figure 6.6 Non-conductive apertures: (A). IonCCD Intensity of nESI plume. (B-E) - Ion CCD images of beam focus through 15 mm (B), 12 mm (C), 9 mm (D) and 3 mm (E) apertures. Note the differing color and axes scales for each figure.

As seen in Figure 6.8, for the curved electrode, the IonCCD data showed an asymmetrical spot, with higher intensity at higher voltage. Cuts through the collected data confirm that, as voltage is increased, the asymmetry also increases. The chicane electrode showed a similar, although less pronounced asymmetry at high voltage. At lower voltage, the peak is largely symmetrical. Finally, the straight electrode shows a flat distribution at higher voltage, but at lower voltage the intensity is mostly seen at the edge of the ion distribution. For the curved and the S-shaped electrodes, most of the ions are lost, perhaps due to the fact that they hit the walls of the device. The geometry of the electrodes results in an asymmetric electric field which in turn causes the asymmetry observed in the IonCCD images.

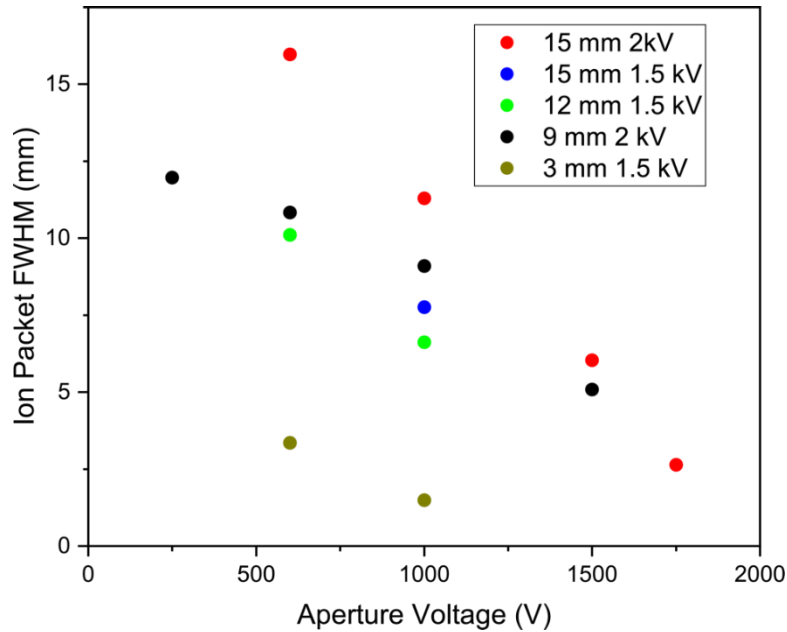


Figure 6.7 Summary of all conductive aperture ion beam data obtained from IonCCD images. For representative IonCCD images, see figure S3.

### 6.3.4 SIMION simulations

#### 6.3.4.1 Conical section electrodes

The cone, ellipsoidal, and cylindrical electrodes were simulated with an electrode potential of 3 kV, and an initial ion energy of 4.5 kV with an electrode, separated from the electrode exit, held at 0 V. The distance from the 0 V electrode to the electrode exit was 15 mm. The ion packet was placed at some distance in the electrode, but given a Gaussian distribution in the x and the y planes. The ions had masses centered around  $m/z$  250. Representative traces are shown in Figure 6.9. SIMION simulations results for each electrode are shown in figure 7. Note that, for each electrode type, the farther the emitter is from the electrode exit the narrower the ion packet becomes. It is also clear that the ions do not spread after exiting the electrode, indicating that atmospheric collisions serve to maintain collimation of the beam when traveling outside the radial confining field. Intriguingly, the loss of ions with emitter distance is not replicated here, indicating that some other physics is likely at play. Still, the results of the simulations show qualitative agreement with the experimental results for the focusing behavior of the different electrodes, although focusing differences between electrodes are not well captured. While only bare ions are considered in these

simulations it is likely that charged droplets from the emitter are also focused in the experiment, which could have an impact on the agreement of these results with experiment.

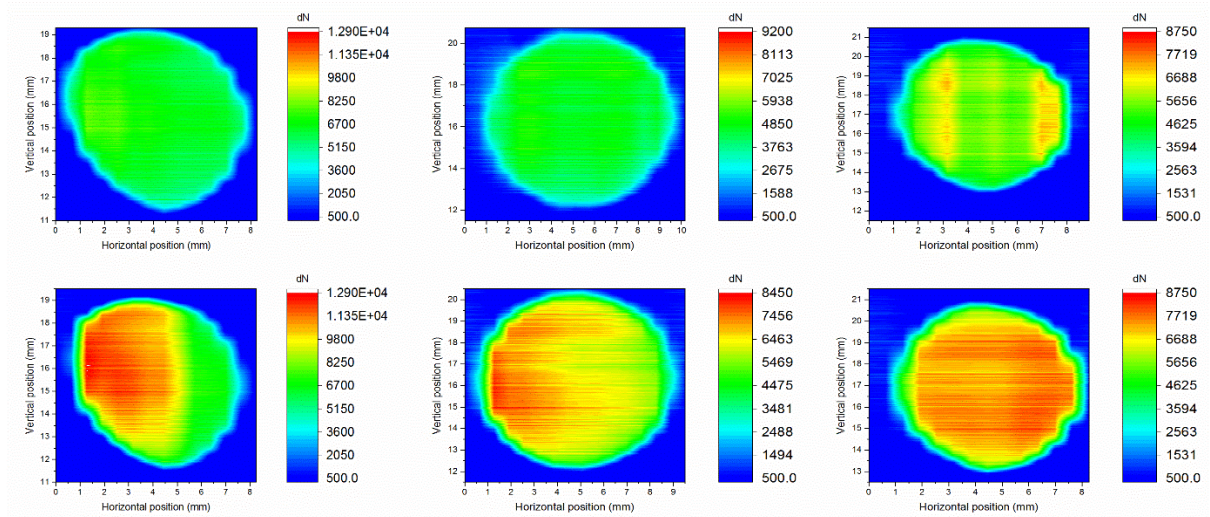


Figure 6.8 IonCCD images of ion beam focus through (Left) curved complex electrode, (Middle) chicane complex electrode, and (Top) straight complex electrode. Top images correspond to initial float voltage of 3 kV, while bottom corresponds to initial float voltage of 4 kV.

### 6.3.4.2 Apertures

Representative simulations of the 15 mm conductive aperture are shown in figure 6.10. The parameters for ion creation were similar to those for the conic section electrodes, except for initial kinetic energy, which was held at either 2 kV or 1.5 kV, taken to be the maximum possible kinetic energy of an ion produced from the emitter. The effect of kinetic energy on the SIMION simulations is shown in Figure 6.10 (A). The potential on the aperture was varied to match the experimental parameters which were probed. Here, it was found that modeling the nESI emitter was necessary to obtain the desired physics seen in the experiment. In all cases the ion behavior observed matched with the experimental data, indicating that the voltage difference between the emitter and aperture is the primary determinant of ion focusing, with smaller differences giving better focusing.

### 6.3.4.3 Complex electrodes

Simulations of the complex geometry electrodes are shown in figure 6.11. In these experiments the ion kinetic energy was held at 6 kV, while the electrode potentials were modeled after the 3 kV case experiments. The initial ion kinetic energy has little effect on the observed trajectories, as seen in figure 6.12. It is immediately apparent that the simulations match poorly with experimental data, although the straight electrode shows the best agreement. Specifically, the asymmetry of the ion packet is well reproduced. The focusing is grossly overestimated for the other electrodes, however. Note that the ion losses from the experiment are also not well reproduced.

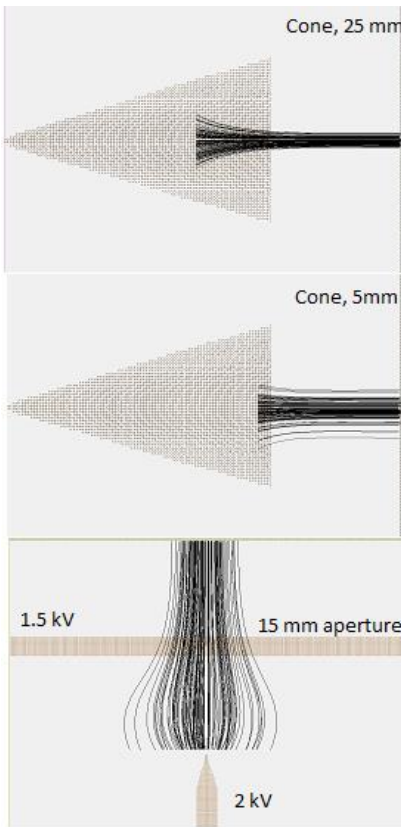


Figure 6.9 Additional SIMION simulation traces. Top: Cone (3 kV) potential, 25 mm emitter position SIMION trace. Middle: cone (3 kV) 5 mm emitter position SIMION trace. Bottom: Aperture (1.5 kV) with emitter (2 kV) SIMION trace. Parameters used for ion generation are as described in the experimental section.

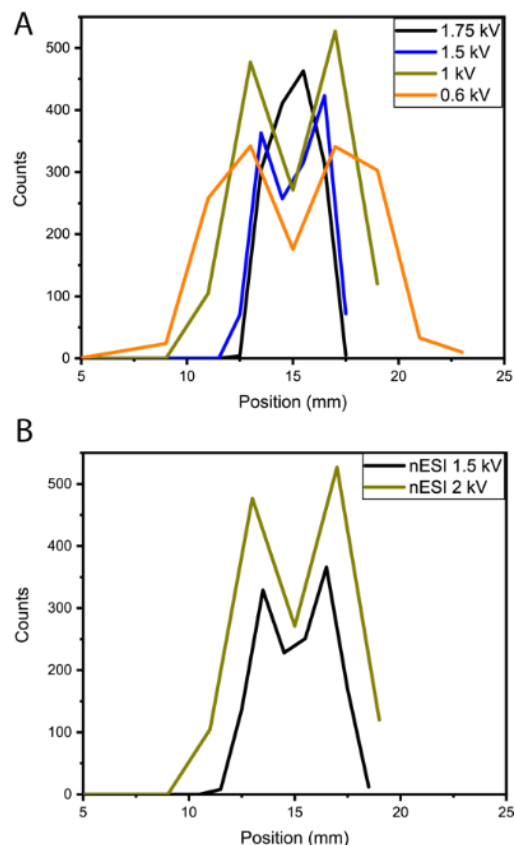


Figure 6.10 A. Profiles of simulations of an ion packet focus through a 15 mm aperture held at the indicated voltages using an emitter voltage of 2 kV. B. Simulations of ion packet focus through a 15 mm aperture held at 1 kV with the emitter held at the indicated voltage.

### 6.3.5 Rationalization of results: Focusing mechanism

From the differences between the experimental measurements and simulations, it is clear that the observed ion focusing and transport results from the interplay of a number of different variables and that these are not fully captured by the available simulations. Certain things however are clear: (i) In contrast to vacuum conditions, ions in the open air are subjected to collisional forces from background gas molecules. At standard temperature and pressure, an ion will undergo a collision on the order of  $10^{10}$  times per second with a background gas molecule. This results in fast momentum transfer from the ion to the neutral background molecules, which slows the ion (collisional cooling). Although the ions may have initial energies on the order of 1 keV, and

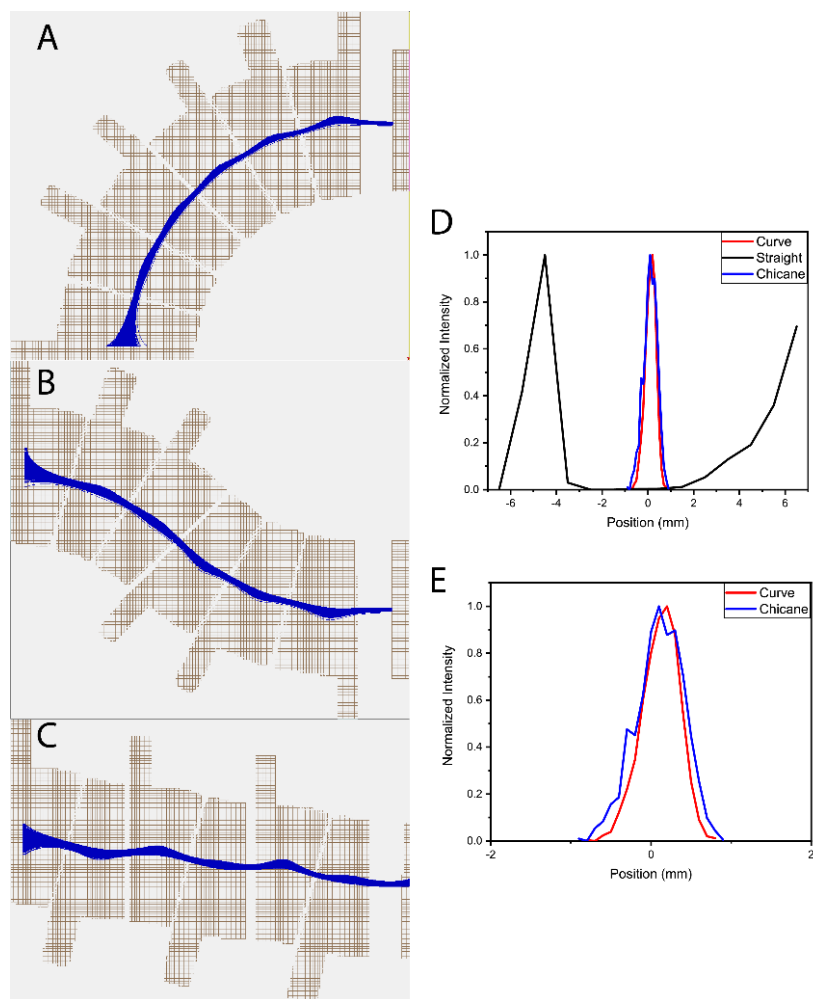


Figure 6.11 SIMION ion trajectories through (A) curved, (B) chicane, and (C) straight versions of complex electrodes. (D-E) profiles of the ion distributions for each electrode geometry, (E) shows up close distributions of the curved and chicane electrodes. In all cases, ions are generated from the left and move towards the right through the electrodes

molecules may have energies of only a few meV, the frequency of collisions is such that ion trajectories may be significantly altered (collisional broadening). (ii) A related process which will also influence focusing is the desolvation of ions as they travel in the open air or through a device. Ions are born from charged microdroplets which undergo evaporation more or less quickly depending on the solvent, to give bare ions. The shrinking droplets also will have less momentum, even at the same energy due to the reduction in mass, further influencing the collision dynamics. While this dynamic process cannot be modeled by SIMION, it should not be overlooked as a factor

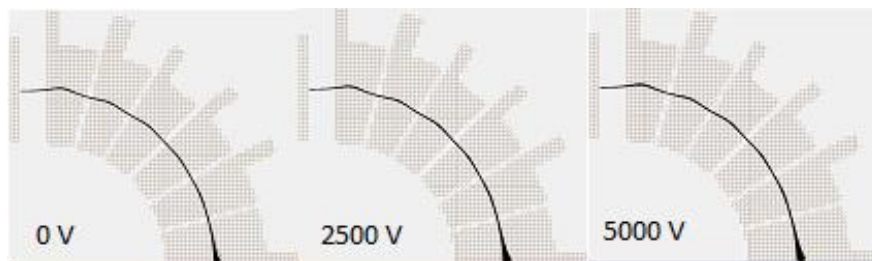


Figure 6.12 0 V (left), 2500 V (middle), and 5000 V (right) initial ion energy trajectories.

in the behavior observed here. (iii) The electric field plays a role, specifically, the field interacts with the ion cloud to change the ion position in space by repelling or attracting charged droplets and ions. For the apertures and conic section electrodes used here, the electric field is symmetric around the center of the device. Thus, ions are “channeled” to this region, which reorients their velocities resulting in collimation of the ion beam. This is best exemplified by the changing of the ion packet size with lower emitter voltage in the case of the 15 mm conductive aperture. The ion kinetic energy is greatly influenced by the electric potentials of the aperture and the nESI emitter, with the larger voltage difference giving rise to the highest energy ions. Lower kinetic energy means that the ions must go to an area with lower electric field to pass through the aperture, which explains, in part, the increased focus. (iv) This collimation is might be aided by the collisions of background gas molecules with the ion cloud, as this constrains the ions from spreading due to space charge between ions. The experimental fact is that a tight focus can be maintained over significant distance, even when ions have exited the electrode. In the case of the asymmetric electrodes, the ions still follow the path of the lowest electric field, although this results in the asymmetry observed in the ion cloud. The mass spectral results of the conic section electrodes, which showed increased signal from heavy ions at long distances, indicate that ion transmission is influenced by the electrodes. It is postulated that the increased energy of the ions as they leave the electrode gives higher kinetic energies compared to nESI alone, thus increasing the chance of transmission of such ions. It is also postulated that the coupling of the electric field and collision effects gives rise to focusing. The fact of focusing is evident from the experimental data and from some of the simulations, for example that shown in Figure 6.13 Here, a simulation of ion cloud trajectory is shown for ambient pressure and vacuum conditions. The ambient pressure scenario gives rise to ion transport through the device, while in vacuum the ions are relatively unaffected

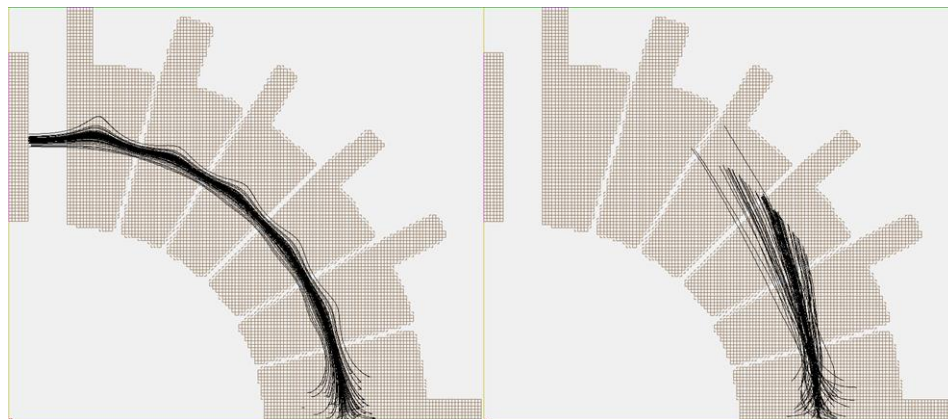


Figure 6.13 Simulations of ions traveling through the curved electrode in the presence of atmospheric gas (left) and in vacuum (right). The direction of ion travel is from the bottom right opening of the electrodes. Note that ions are not transmitted to the exit when collisions are not present.

by the changing electrode potentials and collide with the walls of the device instead of passing through. This implies that collisions result in a lowering of ion energy to match the changing electric field in the device. These observations suggest that high pressures, while requiring different device design considerations, should be viewed not as a hindrance to ion transport, but instead as a potentially useful force. It is also clear that the focusing effect is incompletely understood.

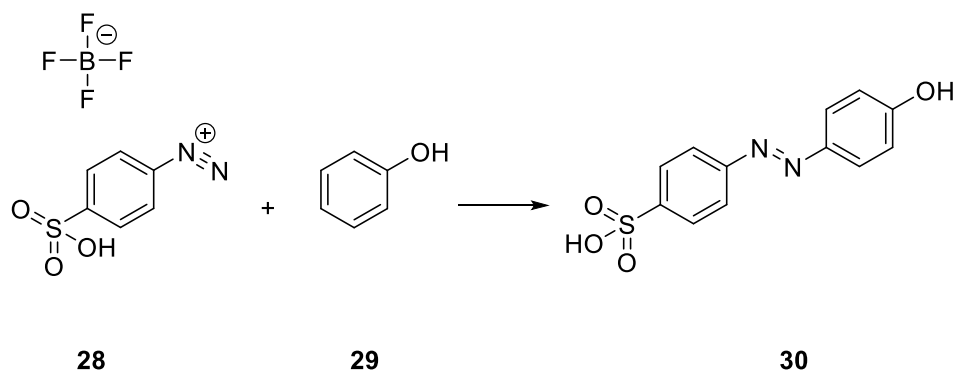
#### 6.4 Conclusions

In this study, focusing of nESI generated ions in air was achieved by using DC potentials on various designs of 3D-printed electrodes. The electric field plays a role in focusing and transmission of ions to the mass spectrometer, but collisions with the background gas (air in this case) are also crucial to the observed focusing. Mass spectral data shows that these devices are also capable of increasing the signal of high mass species at large distances relative to nESI alone, indicating improved ion transmission. The simplicity and ease of construction of these devices with 3D-printing is an additional advantage. Finally, simulations were performed to corroborate findings and optimize

## CHAPTER 7. FUTURE DIRECTIONS

### 7.1 Relating droplet size to reaction acceleration

Droplet microscopy experiments have been shown to be extremely useful in understanding the effect of various parameters such as distance and presence of a surfactant on droplet sizes. Extending the utility of the microscopy experiments to probe a fluorescent reaction can prove to be valuable in understanding reaction acceleration in various droplet sizes. Ideally, the fluorescence reaction that will be chosen, should have a low reaction rate in bulk solution. Additionally, it is imperative that the reagents and products possess an excitation wavelength that matches the available SIM wavelengths. Solubility in glycerol and good ionization are also important. Initial work involved studying a reaction between sulfobenzenediazonium tetrafluoroborate and phenol to produce a derivative of methyl orange (Scheme 7.1)



Scheme 7.1 Reaction between 4-sulfobenzenediazonium tetrafluoroborate and phenol to form a methyl orange derivative.

Initial fluorometry experiments have already been performed on the bulk reaction and the product's spectral characteristics have been shown to be compatible with the wavelengths of the SIM instrument. Future experiments may be designed to explore this reaction in different droplet sizes. One may alter droplet sizes by either changing spray distances or nESI tip sizes. Once the droplet sizes have been measured, the same image may be used to measure fluorescence by counting the pixels in the images and correlating reaction extent with droplet sizes. Other modifications may involve studying non-fluorescent reactions mixed with Rhodamine B and

studying the effect of reaction extent in various droplet sizes. This has already been demonstrated using the hydrazone reaction as a model. It would be useful to gather data on additional reactions to see if they follow the same. Additional experiments may involve explicitly studying the surfaces of droplets using Raman spectroscopy and understanding the role of mass transfer and diffusion in reaction acceleration.

## **7.2 Ion manipulation in air**

Work presented in this dissertation has shown that it is possible to manipulate ions in air using simple designs of 3D-printed electrodes. It has been observed that ions at ambient pressure can be focused to small spots using only electrostatic (DC) potentials, as opposed to RF potentials needed otherwise for focusing in the low-pressure regime. Future work could potentially involve understanding the behavior of charged species, including microdroplets and partially solvated ions in the open air. The ultimate goal of such a study would be to increase ion transmission from an electrospray source to the mass spectrometer. Multi-element setups may also be used to focus a beam of droplets in multiple stages. Findings from the experiments may be applied to sets of multiple nESI emitters, with the goal of merging several ion beams to increase total ion currents which has been one of the fundamental challenges of mass spectrometry.

## REFERENCES

1. Takats, Z.; Wiseman, J. M.; Gologan, B.; Cooks, R. G., Mass spectrometry sampling under ambient conditions with desorption electrospray ionization. *Science* **2004**, *306* (5695), 471-473.
2. Alberici, R. M.; Simas, R. C.; Sanvido, G. B.; Romao, W.; Lalli, P. M.; Benassi, M.; Cunha, I. B. S.; Eberlin, M. N., Ambient mass spectrometry: bringing MS into the "real world". *Anal Bioanal Chem* **2010**, *398* (1), 265-294.
3. Stopka, S. A.; Samarah, L. Z.; Shaw, J. B.; Liyu, A. V.; Velickovic, D.; Agtuca, B. J.; Kukolj, C.; Koppelaar, D. W.; Stacey, G.; Pasa-Tolic, L.; Anderton, C. R.; Vertes, A., Ambient Metabolic Profiling and Imaging of Biological Samples with Ultrahigh Molecular Resolution Using Laser Ablation Electrospray Ionization 21 Tesla FTICR Mass Spectrometry. *Anal Chem* **2019**, *91* (8), 5028-5035.
4. Wang, H.; Liu, J. J.; Cooks, R. G.; Ouyang, Z., Paper Spray for Direct Analysis of Complex Mixtures Using Mass Spectrometry. *Angew Chem Int Edit* **2010**, *49* (5), 877-880.
5. Girod, M.; Moyano, E.; Campbell, D. I.; Cooks, R. G., Accelerated bimolecular reactions in microdroplets studied by desorption electrospray ionization mass spectrometry. *Chem Sci* **2011**, *2* (3), 501-510.
6. Muller, T.; Badu-Tawiah, A.; Cooks, R. G., Accelerated Carbon-Carbon Bond-Forming Reactions in Preparative Electrospray. *Angew Chem Int Edit* **2012**, *51* (47), 11832-11835.
7. Yan, X.; Augusti, R.; Li, X.; Cooks, R. G., Chemical Reactivity Assessment Using Reactive Paper Spray Ionization Mass Spectrometry: The Katritzky Reaction. *Chempluschem* **2013**, *78* (9), 1142-1148.
8. Bain, R. M.; Pulliam, C. J.; Thery, F.; Cooks, R. G., Accelerated Chemical Reactions and Organic Synthesis in Leidenfrost Droplets. *Angew Chem Int Edit* **2016**, *55* (35), 10478-10482.
9. Wei, Z. W.; Wleklinski, M.; Ferreira, C.; Cooks, R. G., Reaction Acceleration in Thin Films with Continuous Product Deposition for Organic Synthesis. *Angew Chem Int Edit* **2017**, *56* (32), 9386-9390.
10. Yamashita, M.; Fenn, J. B., Electrospray Ion-Source - Another Variation on the Free-Jet Theme. *J Phys Chem-US* **1984**, *88* (20), 4451-4459.
11. Fenn, J. B.; Mann, M.; Meng, C. K.; Wong, S. F.; Whitehouse, C. M., Electrospray Ionization-Principles and Practice. *Mass Spectrom Rev* **1990**, *9* (1), 37-70.
12. Fenn, J. B.; Mann, M.; Meng, C. K.; Wong, S. F.; Whitehouse, C. M., Electrospray Ionization for Mass-Spectrometry of Large Biomolecules. *Science* **1989**, *246* (4926), 64-71.

13. Whitehouse, C. M.; Dreyer, R. N.; Yamashita, M.; Fenn, J. B., Electrospray Interface for Liquid Chromatographs and Mass Spectrometers. *Anal Chem* **1985**, *57* (3), 675-679.
14. Rayleigh, L., On The Instability Of Jets. **1878**, *s1-10* (1), 4-13.
15. Konermann, L.; Ahadi, E.; Rodriguez, A. D.; Vahidi, S., Unraveling the Mechanism of Electrospray Ionization. *Anal Chem* **2013**, *85* (1), 2-9.
16. Ahadi, E.; Konermann, L., Modeling the Behavior of Coarse-Grained Polymer Chains in Charged Water Droplets: Implications for the Mechanism of Electrospray Ionization. *J Phys Chem B* **2012**, *116* (1), 104-112.
17. Konermann, L.; Rodriguez, A. D.; Liu, J. J., On the Formation of Highly Charged Gaseous Ions from Unfolded Proteins by Electrospray Ionization. *Anal Chem* **2012**, *84* (15), 6798-6804.
18. Wilm, M. S.; Mann, M., Electrospray and Taylor-Cone Theory, Does Beam of Macromolecules at Last. *Int J Mass Spectrom* **1994**, *136* (2-3), 167-180.
19. Cody, R. B.; Laramee, J. A.; Durst, H. D., Versatile new ion source for the analysis of materials in open air under ambient conditions. *Anal Chem* **2005**, *77* (8), 2297-2302.
20. Liu, J. J.; Wang, H.; Manicke, N. E.; Lin, J. M.; Cooks, R. G.; Ouyang, Z., Development, Characterization, and Application of Paper Spray Ionization. *Anal Chem* **2010**, *82* (6), 2463-2471.
21. Chen, H. W.; Venter, A.; Cooks, R. G., Extractive electrospray ionization for direct analysis of undiluted urine, milk and other complex mixtures without sample preparation. *Chem Commun* **2006**, (19), 2042-2044.
22. Wleklinski, M.; Loren, B. P.; Ferreira, C. R.; Jaman, Z.; Avramova, L.; Sobreira, T. J. P.; Thompson, D. H.; Cooks, R. G., High throughput reaction screening using desorption electrospray ionization mass spectrometry. *Chem Sci* **2018**, *9* (6), 1647-1653.
23. Yan, X.; Cheng, H. Y.; Zare, R. N., Two-Phase Reactions in Microdroplets without the Use of Phase-Transfer Catalysts. *Angew Chem Int Edit* **2017**, *56* (13), 3562-3565.
24. Lee, J. K.; Banerjee, S.; Nam, H. G.; Zare, R. N., Acceleration of reaction in charged microdroplets. *Q Rev Biophys* **2015**, *48* (4), 437-444.
25. Hoffmann, T.; Bandur, R.; Marggraf, U.; Linscheid, M., Molecular composition of organic aerosols formed in the alpha-pinene/O<sub>3</sub> reaction: Implications for new particle formation processes. *J Geophys Res-Atmos* **1998**, *103* (D19), 25569-25578.
26. Kalberer, M.; Paulsen, D.; Sax, M.; Steinbacher, M.; Dommen, J.; Prevot, A. S. H.; Fisseha, R.; Weingartner, E.; Frankevich, V.; Zenobi, R.; Baltensperger, U., Identification of polymers as major components of atmospheric organic aerosols. *Science* **2004**, *303* (5664), 1659-1662.

27. Cooks, R. G.; Chen, H.; Eberlin, M. N.; Zheng, X.; Tao, W. A., Polar acetalization and transacetalization in the gas phase: The Eberlin reaction. *Chem Rev* **2006**, *106* (1), 188-211.
28. Falcone, C. E.; Jaman, Z.; Wleklinski, M.; Koswara, A.; Thompson, D. H.; Cooks, R. G., Reaction screening and optimization of continuous-flow atropine synthesis by preparative electrospray mass spectrometry. *Analyst* **2017**, *142* (15), 2836-2845.
29. Hollerbach, A.; Logsdon, D.; Iyer, K.; Li, A. Y.; Schaber, J. A.; Cooks, R. G., Sizing sub-diffraction limit electrosprayed droplets by structured illumination microscopy. *Analyst* **2018**, *143* (1), 232-240.
30. Espy, R. D.; Muliadi, A. R.; Ouyang, Z.; Cooks, R. G., Spray mechanism in paper spray ionization. *Int J Mass Spectrom* **2012**, *325*, 167-171.
31. Zhou, Z. P.; Yan, X.; Lai, Y. H.; Zare, R. N., Fluorescence Polarization Anisotropy in Microdroplets. *J Phys Chem Lett* **2018**, *9* (11), 2928-2932.
32. Bain, R. M.; Pulliam, C. J.; Ayrton, S. T.; Bain, K.; Cooks, R. G., Accelerated hydrazone formation in charged microdroplets. *Rapid Commun Mass Sp* **2016**, *30* (16), 1875-1878.
33. Yan, X.; Bain, R. M.; Cooks, R. G., Organic Reactions in Microdroplets: Reaction Acceleration Revealed by Mass Spectrometry. *Angew Chem Int Edit* **2016**, *55* (42), 12960-12972.
34. Mondal, S.; Acharya, S.; Biswas, R.; Bagchi, B.; Zare, R. N., Enhancement of reaction rate in small-sized droplets: A combined analytical and simulation study. *J Chem Phys* **2018**, *148* (24).
35. Page, J. S.; Kelly, R. T.; Tang, K.; Smith, R. D., Ionization and transmission efficiency in an electrospray ionization-mass spectrometry interface. *J Am Soc Mass Spectr* **2007**, *18* (9), 1582-1590.
36. Kelly, R. T.; Tolmachev, A. V.; Page, J. S.; Tang, K. Q.; Smith, R. D., The Ion Funnel: Theory, Implementations, and Applications. *Mass Spectrom Rev* **2010**, *29* (2), 294-312.
37. Chen, C. H.; Chen, T. C.; Zhou, X. Y.; Kline-Schoder, R.; Sorensen, P.; Cooks, R. G.; Ouyang, Z., Design of Portable Mass Spectrometers with Handheld Probes: Aspects of the Sampling and Miniature Pumping Systems. *J Am Soc Mass Spectr* **2015**, *26* (2), 240-247.
38. Baird, Z.; Wei, P.; Cooks, R. G., Ion creation, ion focusing, ion/molecule reactions, ion separation, and ion detection in the open air in a small plastic device. *Analyst* **2015**, *140* (3), 696-700.
39. Amsden, J. J.; Gehm, M. E.; Russell, Z. E.; Chen, E. X.; Di Dona, S. T.; Wolter, S. D.; Danell, R. M.; Kibelka, G.; Parker, C. B.; Stoner, B. R.; Brady, D. J.; Glass, J. T., Coded Apertures in Mass Spectrometry. *Annu Rev Anal Chem* **2017**, *10*, 141-156.

40. Adamo, A.; Beingsner, R. L.; Behnam, M.; Chen, J.; Jamison, T. F.; Jensen, K. F.; Monbaliu, J. C. M.; Myerson, A. S.; Revalor, E. M.; Snead, D. R.; Stelzer, T.; Weeranoppanant, N.; Wong, S. Y.; Zhang, P., On-demand continuous-flow production of pharmaceuticals in a compact, reconfigurable system. *Science* **2016**, *352* (6281), 61-67.
41. Bedard, A. C.; Longstreet, A. R.; Britton, J.; Wang, Y. R.; Moriguchi, H.; Hicklin, R. W.; Green, W. H.; Jamison, T. F., Minimizing E-factor in the continuous-flow synthesis of diazepam and atropine. *Bioorgan Med Chem* **2017**, *25* (23), 6233-6241.
42. Baumann, M.; Baxendale, I. R., The synthesis of active pharmaceutical ingredients (APIs) using continuous flow chemistry. *Beilstein J Org Chem* **2015**, *11*, 1194-1219.
43. Malet-Sanz, L.; Susanne, F., Continuous Flow Synthesis. A Pharma Perspective. *J Med Chem* **2012**, *55* (9), 4062-4098.
44. McQuade, D. T.; Seeberger, P. H., Applying Flow Chemistry: Methods, Materials, and Multistep Synthesis. *J Org Chem* **2013**, *78* (13), 6384-6389.
45. Chen, P., Electrospray ionization tandem mass spectrometry in high-throughput screening of homogeneous catalysts. *Angew Chem Int Edit* **2003**, *42* (25), 2832-2847.
46. Santos, L. S.; Rosso, G. B.; Pilli, R. A.; Eberlin, M. N., The mechanism of the stille reaction investigated by electrospray ionization mass spectrometry. *J Org Chem* **2007**, *72* (15), 5809-5812.
47. Huang, G. M.; Li, G. T.; Ducan, J.; Ouyang, Z.; Cooks, R. G., Synchronized Inductive Desorption Electrospray Ionization Mass Spectrometry. *Angew Chem Int Edit* **2011**, *50* (11), 2503-2506.
48. Banerjee, S.; Zare, R. N., Syntheses of Isoquinoline and Substituted Quinolines in Charged Microdroplets. *Angew Chem Int Edit* **2015**, *54* (49), 14795-14799.
49. Bain, R. M.; Pulliam, C. J.; Cooks, R. G., Accelerated Hantzsch electrospray synthesis with temporal control of reaction intermediates. *Chem Sci* **2015**, *6* (1), 397-401.
50. Bain, R. M.; Pulliam, C. J.; Raab, S. A.; Cooks, G., Chemical Synthesis Accelerated by Paper Spray: The Haloform Reaction. *J Chem Educ* **2016**, *93* (2), 340-344.
51. Wleklinski, M.; Falcone, C. E.; Loren, B. P.; Jaman, Z.; Iyer, K.; Ewan, H. S.; Hyun, S. H.; Thompson, D. H.; Cooks, R. G., Can Accelerated Reactions in Droplets Guide Chemistry at Scale? *Eur J Org Chem* **2016**, (33), 5480-5484.
52. Roughley, S. D.; Jordan, A. M., The Medicinal Chemist's Toolbox: An Analysis of Reactions Used in the Pursuit of Drug Candidates. *J Med Chem* **2011**, *54* (10), 3451-3479.

53. Maslanka, A.; Krzek, J.; Szlosarczyk, M.; Zmudzki, P.; Wach, K., Dependence of the kinetic and thermodynamic parameters on hydrophilic-lipophilic character of alprazolam, clonazepam, diazepam, doxepin and haloperidol in alkaline environment. *Int J Pharmaceut* **2013**, *455* (1-2), 104-112.
54. Paul, S. M.; Mytelka, D. S.; Dunwiddie, C. T.; Persinger, C. C.; Munos, B. H.; Lindborg, S. R.; Schacht, A. L., How to improve R&D productivity: the pharmaceutical industry's grand challenge. *Nat Rev Drug Discov* **2010**, *9* (3), 203-214.
55. Loren, B. P.; Wleklinski, M.; Koswara, A.; Yammine, K.; Hu, Y. Y.; Nagy, Z. K.; Thompson, D. H.; Cooks, R. G., Mass spectrometric directed system for the continuous-flow synthesis and purification of diphenhydramine. *Chem Sci* **2017**, *8* (6), 4363-4370.
56. Jin, S. H.; Lee, S. S.; Lee, B.; Jeong, S. G.; Peter, M.; Lee, C. S., Programmable Static Droplet Array for the Analysis of Cell-Cell Communication in a Confined Microenvironment. *Anal Chem* **2017**, *89* (18), 9722-9729.
57. Narayan, S.; Muldoon, J.; Finn, M. G.; Fokin, V. V.; Kolb, H. C.; Sharpless, K. B., "On water": Unique reactivity of organic compounds in aqueous suspension. *Angew Chem Int Edit* **2005**, *44* (21), 3275-3279.
58. Jones, G. O.; Liu, P.; Houk, K. N.; Buchwald, S. L., Computational Explorations of Mechanisms and Ligand-Directed Selectivities of Copper-Catalyzed Ullmann-Type Reactions. *J Am Chem Soc* **2010**, *132* (17), 6205-6213.
59. Giri, R.; Hartwig, J. F., Cu(I)-Amido Complexes in the Ullmann Reaction: Reactions of Cu(I)-Amido Complexes with Iodoarenes with and without Autocatalysis by CuI. *J Am Chem Soc* **2010**, *132* (45), 15860-15863.
60. Yu, H. Z.; Jiang, Y. Y.; Fu, Y.; Liu, L., Alternative Mechanistic Explanation for Ligand-Dependent Selectivities in Copper-Catalyzed N- and O-Arylation Reactions. *J Am Chem Soc* **2010**, *132* (51), 18078-18091.
61. Tye, J. W.; Weng, Z.; Johns, A. M.; Incarvito, C. D.; Hartwig, J. F., Copper complexes of anionic nitrogen ligands in the amidation and imidation of aryl halides. *J Am Chem Soc* **2008**, *130* (30), 9971-9983.
62. Hickman, A. J.; Sanford, M. S., High-valent organometallic copper and palladium in catalysis. *Nature* **2012**, *484* (7393), 177-185.
63. Creutz, S. E.; Lotito, K. J.; Fu, G. C.; Peters, J. C., Photoinduced Ullmann C-N Coupling: Demonstrating the Viability of a Radical Pathway. *Science* **2012**, *338* (6107), 647-651.
64. Ley, S. V.; Thomas, A. W., Modern synthetic methods for copper-mediated C(aryl)-O, C(aryl)-N, and C(aryl)-S bond formation. *Angew Chem Int Edit* **2003**, *42* (44), 5400-5449.
65. Beletskaya, I. P.; Cheprakov, A. V., Copper in cross-coupling reactions - The post-Ullmann chemistry. *Coord Chem Rev* **2004**, *248* (21-24), 2337-2364.

66. Monnier, F.; Taillefer, M., Catalytic C-C, C-N, and C-O Ullmann-Type Coupling Reactions. *Angew Chem Int Edit* **2009**, *48* (38), 6954-6971.
67. Fagan, P. J.; Hauptman, E.; Shapiro, R.; Casalnuovo, A., Using intelligent/random library screening to design focused libraries for the optimization of homogeneous catalysts: Ullmann ether formation. *J Am Chem Soc* **2000**, *122* (21), 5043-5051.
68. Wolter, M.; Nordmann, G.; Job, G. E.; Buchwald, S. L., Copper-catalyzed coupling of aryl iodides with aliphatic alcohols. *Org Lett* **2002**, *4* (6), 973-976.
69. Shafir, A.; Lichtor, P. A.; Buchwald, S. L., N- versus O-arylation of aminoalcohols: Orthogonal selectivity in copper-based catalysts. *J Am Chem Soc* **2007**, *129* (12), 3490-+.
70. Altman, R. A.; Shafir, A.; Choi, A.; Lichtor, P. A.; Buchwald, S. L., An improved cu-based catalyst system for the reactions of alcohols with aryl halides. *J Org Chem* **2008**, *73* (1), 284-286.
71. Maiti, D.; Buchwald, S. L., Orthogonal Cu- and Pd-Based Catalyst Systems for the O- and N-Arylation of Aminophenols. *J Am Chem Soc* **2009**, *131* (47), 17423-17429.
72. Schwarz, H.; Gonzalez-Navarrete, P.; Li, J. L.; Schlangen, M.; Sun, X. Y.; Weiske, T.; Zhou, S. D., Unexpected Mechanistic Variants in the Thermal Gas-Phase Activation of Methane. *Organometallics* **2017**, *36* (1), 8-17.
73. Bain, R. M.; Pulliam, C. J.; Yan, X.; Moore, K. F.; Muller, T.; Cooks, R. G., Mass Spectrometry in Organic Synthesis: Claisen-Schmidt Base-Catalyzed Condensation and Hammett Correlation of Substituent Effects. *J Chem Educ* **2014**, *91* (11), 1985-1989.
74. Lee, J. K.; Kim, S.; Nam, H. G.; Zare, R. N., Microdroplet fusion mass spectrometry for fast reaction kinetics. *P Natl Acad Sci USA* **2015**, *112* (13), 3898-3903.
75. Bain, R. M.; Sathyamoorthi, S.; Zare, R. N., "On-Droplet" Chemistry: The Cycloaddition of Diethyl Azodicarboxylate and Quadricyclane. *Angew Chem Int Edit* **2017**, *56* (47), 15083-15087.
76. Lai, Y. H.; Sathyamoorthi, S.; Bain, R. M.; Zare, R. N., Microdroplets Accelerate Ring Opening of Epoxides. *J Am Soc Mass Spectr* **2018**, *29* (5), 1036-1043.
77. Espy, R. D.; Wleklinski, M.; Yan, X.; Cooks, R. G., Beyond the flask: Reactions on the fly in ambient mass spectrometry. *Trac-Trend Anal Chem* **2014**, *57*, 135-146.
78. Lee, J. K.; Samanta, D.; Nam, H. G.; Zare, R. N., Spontaneous formation of gold nanostructures in aqueous microdroplets. *Nat Commun* **2018**, *9*.
79. Dobson, C. M.; Ellison, G. B.; Tuck, A. F.; Vaida, V., Atmospheric aerosols as prebiotic chemical reactors. *P Natl Acad Sci USA* **2000**, *97* (22), 11864-11868.

80. Crawford, E. A.; Esen, C.; Volmer, D. A., Real Time Monitoring of Containerless Microreactions in Acoustically Levitated Droplets via Ambient Ionization Mass Spectrometry. *Anal Chem* **2016**, *88* (17), 8396-8403.
81. Fallah-Araghi, A.; Meguellati, K.; Baret, J. C.; El Harrak, A.; Mangeat, T.; Karplus, M.; Ladame, S.; Marques, C. M.; Griffiths, A. D., Enhanced Chemical Synthesis at Soft Interfaces: A Universal Reaction-Adsorption Mechanism in Microcompartments. *Phys Rev Lett* **2014**, *112* (2).
82. Allen, H. C.; Casillas-Ituarte, N. N.; Sierra-Hernandez, M. R.; Chen, X. K.; Tang, C. Y., Shedding light on water structure at air-aqueous interfaces: ions, lipids, and hydration. *Phys Chem Chem Phys* **2009**, *11* (27), 5538-5549.
83. Liigand, P.; Heering, A.; Kaupmees, K.; Leito, I.; Girod, M.; Antoine, R.; Kruve, A., The Evolution of Electrospray Generated Droplets is Not Affected by Ionization Mode. *J Am Soc Mass Spectr* **2017**, *28* (10), 2124-2131.
84. Soleilhac, A.; Dagany, X.; Dugourd, P.; Girod, M.; Antoine, R., Correlating Droplet Size with Temperature Changes in Electrospray Source by Optical Methods. *Anal Chem* **2015**, *87* (16), 8210-8217.
85. Chen, Y. X.; Okur, H. I.; Lutgebaucks, C.; Roke, S., Zwitterionic and Charged Lipids Form Remarkably Different Structures on Nanoscale Oil Droplets in Aqueous Solution. *Langmuir* **2018**, *34* (3), 1042-1050.
86. Gopalakrishnan, S.; Liu, D. F.; Allen, H. C.; Kuo, M.; Shultz, M. J., Vibrational spectroscopic studies of aqueous interfaces: Salts, acids, bases, and nanodrops. *Chem Rev* **2006**, *106* (4), 1155-1175.
87. Mitropoulos, A., What is a surface excess? *Journal of Engineering Science and Technology Review* **2008**, *1*.
88. Lehanine, Z.; Badache, L., Effect of the Molecular Structure on the Adsorption Properties of Cationic Surfactants at the Air–Water Interface. *Journal of Surfactants and Detergents* **2016**, *19* (2), 289-295.
89. Tang, L.; Kebarle, P., Dependence of ion intensity in electrospray mass spectrometry on the concentration of the analytes in the electrosprayed solution. *Analytical Chemistry* **1993**, *65* (24), 3654-3668.
90. Tang, L.; Kebarle, P., Dependence of Ion Intensity in Electrospray Mass-Spectrometry on the Concentration of the Analytes in the Electrosprayed Solution. *Anal Chem* **1993**, *65* (24), 3654-3668.
91. Wang, C. Y.; Morgner, H., The dependence of surface tension on surface properties of ionic surfactant solution and the effects of counter-ions therein. *Phys Chem Chem Phys* **2014**, *16* (42), 23386-23393.

92. Nam, I.; Nam, H. G.; Zare, R. N., Abiotic synthesis of purine and pyrimidine ribonucleosides in aqueous microdroplets. *P Natl Acad Sci USA* **2018**, *115* (1), 36-40.
93. Badu-Tawiah, A. K.; Campbell, D. I.; Cooks, R. G., Accelerated C-N Bond Formation in Dropcast Thin Films on Ambient Surfaces. *J Am Soc Mass Spectr* **2012**, *23* (9), 1461-1468.
94. Baird, Z.; Peng, W. P.; Cooks, R. G., Ion transport and focal properties of an ellipsoidal electrode operated at atmospheric pressure. *Int J Mass Spectrom* **2012**, *330*, 277-284.
95. Li, A. Y.; Baird, Z.; Bag, S.; Sarkar, D.; Prabhath, A.; Pradeep, T.; Cooks, R. G., Using Ambient Ion Beams to Write Nanostructured Patterns for Surface Enhanced Raman Spectroscopy. *Angew Chem Int Edit* **2014**, *53* (46), 12528-12531.
96. Suzuki, A., Cross-Coupling Reactions Of Organoboranes: An Easy Way To Construct C-C Bonds (Nobel Lecture). *Angew Chem Int Edit* **2011**, *50* (30), 6722-6737.
97. Brow, D. G.; Bostrom, J., Analysis of Past and Present Synthetic Methodologies on Medicinal Chemistry: Where Have All the New Reactions Gone? *J Med Chem* **2016**, *59* (10), 4443-4458.
98. Miyaura, N.; Yamada, K.; Suzuki, A., New Stereospecific Cross-Coupling by the Palladium-Catalyzed Reaction of 1-Alkenylboranes with 1-Alkenyl or 1-Alkynyl Halides. *Tetrahedron Lett* **1979**, *20* (36), 3437-3440.
99. Miyaura, N.; Suzuki, A., Stereoselective Synthesis of Arylated (E)-Alkenes by the Reaction of Alk-1-Enylboranes with Aryl Halides in the Presence of Palladium Catalyst. *J Chem Soc Chem Comm* **1979**, (19), 866-867.
100. Han, F. S., Transition-metal-catalyzed Suzuki-Miyaura cross-coupling reactions: a remarkable advance from palladium to nickel catalysts. *Chem Soc Rev* **2013**, *42* (12), 5270-5298.
101. Yang, C. T.; Zhang, Z. Q.; Liu, Y. C.; Liu, L., Copper-Catalyzed Cross-Coupling Reaction of Organoboron Compounds with Primary Alkyl Halides and Pseudohalides. *Angew Chem Int Edit* **2011**, *50* (17), 3904-3907.
102. Negishi, E.; Baba, S., Novel Stereoselective Alkenyl-Aryl Coupling Via Nickel-Catalyzed Reaction of Alkenylalanes with Aryl Halides. *J Chem Soc Chem Comm* **1976**, (15), 596-597.
103. Heck, R. F., Arylation Methylation and Carboxyalkylation of Olefins by Group 8 Metal Derivatives. *J Am Chem Soc* **1968**, *90* (20), 5518-&.
104. Leadbeater, N. E.; Marco, M., Ligand-free palladium catalysis of the Suzuki reaction in water using microwave heating. *Org Lett* **2002**, *4* (17), 2973-2976.
105. Banerjee, S.; Gnanamani, E.; Yan, X.; Zare, R. N., Can all bulk-phase reactions be accelerated in microdroplets? *Analyst* **2017**, *142* (9), 1399-1402.

106. Augusti, R.; Chen, H.; Eberlin, L. S.; Nefliu, M.; Cooks, R. G., Atmospheric pressure Eberlin transacetalization reactions in the heterogeneous liquid/gas phase. *Int J Mass Spectrom* **2006**, *253* (3), 281-287.
107. Fedick, P. W.; Bain, R. M.; Bain, K.; Mehari, T. F.; Cooks, R. G., Accelerated tert-butylloxycarbonyl deprotection of amines in microdroplets produced by a pneumatic spray. *Int J Mass Spectrom* **2018**, *430*, 98-103.
108. Bain, R. M.; Ayrton, S. T.; Cooks, R. G., Fischer Indole Synthesis in the Gas Phase, the Solution Phase, and at the Electrospray Droplet Interface. *J Am Soc Mass Spectr* **2017**, *28* (7), 1359-1364.
109. Wei, Z. W.; Zhang, X. C.; Wang, J. Y.; Zhang, S. C.; Zhang, X. R.; Cooks, R. G., High yield accelerated reactions in nonvolatile microthin films: chemical derivatization for analysis of single-cell intracellular fluid. *Chem Sci* **2018**, *9* (40), 7779-7786.
110. Quere, D., Leidenfrost Dynamics. *Annu Rev Fluid Mech* **2013**, *45*, 197-215.
111. Fedick, P. W.; Bain, R. M.; Miao, S. S.; Pirro, V.; Cooks, R. G., State-of-the-art mass spectrometry for point-of-care and other applications: A hands-on intensive short course for undergraduate students. *Int J Mass Spectrom* **2017**, *417*, 22-28.
112. Ewan, H. S.; Iyer, K.; Hyun, S. H.; Wleklinski, M.; Cooks, R. G.; Thompson, D. H., Multistep Flow Synthesis of Diazepam Guided by Droplet-Accelerated Reaction Screening with Mechanistic Insights from Rapid Mass Spectrometry Analysis. *Org Process Res Dev* **2017**, *21* (10), 1566-1570.
113. Abdelaziz, R.; Disci-Zayed, D.; Hedayati, M. K.; Pohls, J. H.; Zillohu, A. U.; Erkartal, B.; Chakravadhanula, V. S. K.; Duppel, V.; Kienle, L.; Elbahri, M., Green chemistry and nanofabrication in a levitated Leidenfrost drop. *Nat Commun* **2013**, *4*.
114. Wei, H. R.; Vejerano, E. P.; Leng, W. N.; Huang, Q. S.; Willner, M. R.; Marr, L. C.; Vikesland, P. J., Aerosol microdroplets exhibit a stable pH gradient. *P Natl Acad Sci USA* **2018**, *115* (28), 7272-7277.
115. Kotha, S.; Lahiri, K.; Kashinath, D., Recent applications of the Suzuki-Miyaura cross-coupling reaction in organic synthesis. *Tetrahedron* **2002**, *58* (48), 9633-9695.
116. Fumagalli, L.; Esfandiar, A.; Fabregas, R.; Hu, S.; Ares, P.; Janardanan, A.; Yang, Q.; Radha, B.; Taniguchi, T.; Watanabe, K.; Gomila, G.; Novoselov, K. S.; Geim, A. K., Anomalously low dielectric constant of confined water. *Science* **2018**, *360* (6395), 1339-+.
117. Harris, G. A.; Galhena, A. S.; Fernandez, F. M., Ambient Sampling/Ionization Mass Spectrometry: Applications and Current Trends. *Anal Chem* **2011**, *83* (12), 4508-4538.
118. Cox, J. T.; Marginean, I.; Smith, R. D.; Tang, K. Q., On the Ionization and Ion Transmission Efficiencies of Different ESI-MS Interfaces. *J Am Soc Mass Spectr* **2015**, *26* (1), 55-62.

119. Cech, N. B.; Enke, C. G., Practical implications of some recent studies in electrospray ionization fundamentals. *Mass Spectrom Rev* **2001**, *20* (6), 362-387.
120. Janulyte, A.; Zerega, Y.; Andre, J.; Brkic, B.; Taylor, S., Performance assessment of a portable mass spectrometer using a linear ion trap operated in non-scanning mode. *Rapid Commun Mass Sp* **2016**, *30* (22), 2407-2415.
121. Badu-Tawiah, A. K.; Wu, C. P.; Cooks, R. G., Ambient Ion Soft Landing. *Anal Chem* **2011**, *83* (7), 2648-2654.
122. Saf, R.; Goriup, M.; Steindl, T.; Hamedinger, T. E.; Sandholzer, D.; Hayn, G., Thin organic films by atmospheric-pressure ion deposition. *Nat Mater* **2004**, *3* (5), 323-329.
123. Li, A. Y.; Luo, Q. J.; Park, S. J.; Cooks, R. G., Synthesis and Catalytic Reactions of Nanoparticles formed by Electrospray Ionization of Coinage Metals. *Angew Chem Int Edit* **2014**, *53* (12), 3147-3150.
124. Foo, C.; Lim, H. N.; Mahdi, M. A.; HaniffWahid, M.; Huang, N. M., Three-Dimensional Printed Electrode and Its Novel Applications in Electronic Devices. *Sci Rep-Uk* **2018**, *8*.
125. Hadjar, O.; Schlatholter, T.; Davila, S.; Catledge, S. A.; Kuhn, K.; Kassin, S.; Kibelka, G.; Cameron, C.; Verbeck, G. F., IonCCD Detector for Miniature Sector-Field Mass Spectrometer: Investigation of Peak Shape and Detector Surface Artifacts Induced by keV Ion Detection. *J Am Soc Mass Spectr* **2011**, *22* (10), 1872-1884.
126. Appelhans, A. D.; Dahl, D. A., SIMION ion optics simulations at atmospheric pressure. *Int J Mass Spectrom* **2005**, *244* (1), 1-14.

## VITA

Kiran Iyer was born and raised in Mumbai, India. She attended Bombay College of Pharmacy where she obtained her bachelor's degree in pharmacy following which she moved to Vellore India to pursue a master's degree in medicinal chemistry. During her time as a master's student, she had the opportunity to intern at Piramal Life Sciences Ltd where she worked in the process chemistry group to optimize synthetic routes for anti-mycobacterial molecules. Following her internship, she secured a full-time position in the same company as a computational chemist where she worked closely with synthetic medicinal chemists to design drugs for inflammation and diabetes.

She moved to Atlanta, GA in 2011 and worked for The Coca Cola Company in the Analytical Research and Development group. It was here that Kiran gained exposure to mass spectrometry. After spending three years working with various mass spectrometers and applications, Kiran decided to pursue graduate school in 2015 and enrolled in Purdue University. Kiran joined the research lab of Dr. R. Graham Cooks and worked on studying chemical reactions in microdroplets generated by various ionization sources. Additionally, she also worked on instrumentation projects that involved the use of 3D-printing to fabricate electrodes to focus and manipulate ions in air. During her time in the Cooks' research group, Kiran published 7 papers.

Kiran also did a summer internship at Agilent Technologies at Santa Clara, CA under Dr. Shane Tichy. The internship mainly focused on optimizing detectors and sources for triple quadrupole mass spectrometers using liquid chromatography.

Kiran is a member of the American Chemical Society and the American Society for Mass Spectrometry. She also served the chemistry department as the Analytical division representative and Co-chair on the Graduate Student Advisory Board.

## PUBLICATIONS

1. Wleklinski, M., Falcone, C. E., Loren, B. P., Jaman, Z., Iyer, K., Ewan, H. S., Hyun, S.-H., Thompson, D. H. and Cooks, R. G. (2016), Can Accelerated Reactions in Droplets Guide Chemistry at Scale? *Eur. J. Org. Chem.*, 2016: 5480–5484.
2. Iyer, K.†, Ewan, H.S,† Hyun, S.-H, Wleklinski, M., Cooks, R. G., Thompson, D. H.(2017), Multistep Flow Synthesis of Diazepam Guided by Droplet-Accelerated Reaction Screening with Mechanistic Insights from Rapid Mass Spectrometry Analysis. *Org. Process Res. Dev.* 2017, 21, 1566-1570
3. Hollerbach, A., Logsdon, D, Iyer, K., Li, A, Schaber, A.J, Cooks, R.G. (2018), Sizing sub-diffraction limit electrosprayed droplets by structured illumination microscopy. *Analyst*, 2018, 143, 232
4. Iyer, K., Yi, J., Bogdan, A., Talaty, N., Djuric, S. W., Cooks, R. G. (2018), Accelerated multi-reagent copper catalyzed coupling reactions in micro droplets and thin films. *React. Chem. Eng.*, 2018, 3, 206
5. Marsh, M. B, Iyer,K., Cooks, R.G. (2019) Reaction acceleration in electrospray droplets: size, distance and surfactant effects, *J. Am. Soc. Mass Spectrom.* (2019) 30: 2144. <https://doi.org/10.1007/s13361-019-02287-3>
6. Iyer,K., Fedick, P., Wei, Z., Avramova, A., Cooks, R.G. (2019) Screening and acceleration of Suzuki cross coupling reaction in desorption electrospray ionization and Leidenfrost droplets. *J. Am. Soc. Mass Spectrom.* (2019) 30: 2144. <https://doi.org/10.1007/s13361-019-02287-3>
7. Iyer,K., Marsh, M.B., Capek, G.O., Schrader, R.L., Tichy, S., Cooks, R.G. (2019) Ion Manipulation in open air using 3D-printed electrodes. *J. Am. Soc. Mass Spectrom.* (2019). <https://doi.org/10.1007/s13361-019-02307-2>



Cite this: *React. Chem. Eng.*, 2018, 3, 206

## Accelerated multi-reagent copper catalysed coupling reactions in micro droplets and thin films†

Kiran Iyer,<sup>a</sup> Jing Yi,<sup>a</sup> Andrew Bogdan,<sup>b</sup> Nari Talaty,<sup>b</sup> Stevan W. Djuric<sup>b</sup> and R. Graham Cooks<sup>id</sup>\*<sup>a</sup>

Received 9th January 2018,  
Accepted 8th February 2018

DOI: 10.1039/c8re00002f

rsc.li/reaction-engineering

Electrospray (ES) and paper spray (PS) mass spectrometry were used to create confined liquid volumes in which accelerated air and water sensitive, heterogeneous, copper catalysed C–O and C–N coupling reactions occur. Significant reaction acceleration was observed compared to the bulk reaction which required elevated temperatures and time for completion. Macroscopic amounts of product (mg scale) were prepared using offline ES within minutes. The trends in reactivity observed for several reagents matched those of the bulk reactions making droplet accelerated reactions good mimics of the bulk chemistry.

### Introduction

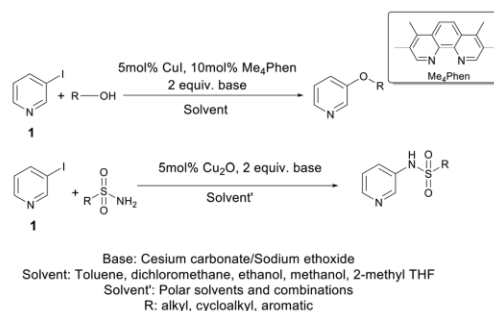
Acceleration of chemical reactions is a valuable tool in the chemical industry for decreasing reaction time, enhancing overall process efficiency and throughput, and reducing costs.<sup>1,2</sup> Recently, microdroplets, generated by electrospray ionization (ESI), have been shown to represent media in which many reactions are strongly accelerated.<sup>3,4</sup> Rate acceleration has been attributed to the reduced activation energy associated with partially desolvated reagents at the interfaces,<sup>3a</sup> in confined volume systems the increased surface area-to-volume ratios can make interfacial reactivity the dominant feature. Changes in pH and reagent concentration upon solvent evaporation also affect reaction rates. A study by Lee *et al.* has described the development of a droplet array platform that can aid in the control of concentration in a single droplet.<sup>5</sup> In addition to ESI, other ambient ionization methods that can be used to generate microdroplets include paper spray (PS) and atmospheric-pressure chemical ionization (APCI). In this study, we report the acceleration of two coupling reactions (Scheme 1) using ES and PS. Subsequent scale-up and product collection in the 20–50 mg scale using ES is also demonstrated for both reactions.

Coupling of C–N, C–O, C–S and C–C bonds is widely used in organic synthesis. Earlier studies have shown that these reactions typically require catalytic conditions and stoichiometric amounts of metals such as copper salts or palladium as catalysts.<sup>6,7</sup> Copper is lighter and cheaper than palladium and is hence the preferred catalyst for these couplings.<sup>8,9</sup> Much effort

has been devoted to using catalytic copper under milder conditions of pressure and temperature.<sup>10</sup> In the present study, we report significant acceleration of both types of coupling reactions, with product being detected almost immediately in the droplets that are generated by spraying. By contrast, the corresponding bulk reactions took 24–30 hours to complete. To test the generality of the findings, several experimental setups were used to generate microdroplets for reaction acceleration. All reagents were handled under nitrogen but the reaction solution was simply sprayed under ambient conditions.

### C–O coupling

First, we explored the C–O coupling reaction between 3-iodopyridine and various alcohols. The base used for the C–O coupling reaction was cesium carbonate and the solvent was toluene. Online MS using ES (Fig. 1a) and PS



**Scheme 1** C–O coupling and C–N coupling using 3-iodopyridine with an alcohol or sulfonamide as reagents.

<sup>a</sup> Department of Chemistry, Purdue University, 560 Oval Drive, West Lafayette, IN 47907, USA. E-mail: cooks@purdue.edu

<sup>b</sup> AbbVie Inc., 1 N. Waukegan Rd, North Chicago, IL 60064, USA

† Electronic supplementary information (ESI) available. See DOI: 10.1039/c8re00002f

(Fig. 1b) showed product a minute after beginning to spray the reaction mixture when using ethanol as the coupling partner (Fig. 2a). It is to be noted that the first minute is used in stabilizing the spray from the positively pressurized reaction vessel before adding the 3-iodopyridine to the reaction flask. The accelerated reactions occur in the sprayed droplets and/or the thin film deposited on the paper substrate. In contrast, the bulk reaction does not show any product formation when analyzed using nano-electrospray ionization (nESI); in fact the bulk reaction required close to 30 hours and 80–130 °C for completion. The spray volumes and voltages used in nESI are smaller than those used in ESI and the short distance over which nESI droplets travel does not allow for acceleration. The time difference (30 h vs. 1 min) corresponds to an acceleration factor of several orders of magnitude in droplets when compared to the bulk reaction. Formation of product was confirmed by recording MS/MS when selecting the ions,  $m/z$  124, corresponding to the protonated ether. Sodium ethoxide was chosen as a base for this reaction since it showed greater conversion efficiency than cesium carbonate which has been used in previously reported studies.<sup>10d</sup> Cesium carbonate also posed solubility problems which was overcome by using sodium ethoxide. Sodium ethoxide was hence chosen for scale up over cesium carbonate. PS was also explored for reaction acceleration. PS is also an ambient ionization technique like ES in which reagents are dropped onto a piece of triangular paper. As the solvent evaporates, a thin film is formed on the paper and when a potential is applied, a spray is generated from the tip of the paper. Although acceleration was observed, PS is not amenable to scale up since the paper does not maintain its integrity for long periods of spray duration. Hence PS was not explored for offline collection and scale up but was instead used as an additional analytical method to demonstrate reaction acceleration. The setup for ES scale up is shown in Fig. 1c. A grounded scintillation vial (20 ml) was used as the collecting surface. The scintillation vial was cooled in dry ice during collection to minimize loss of the volatile product. The collected product was rinsed with deuterated chloroform and characterized by NMR (ESI,† Fig. S2). Quantitation was performed by adding an internal standard (1,3,5-

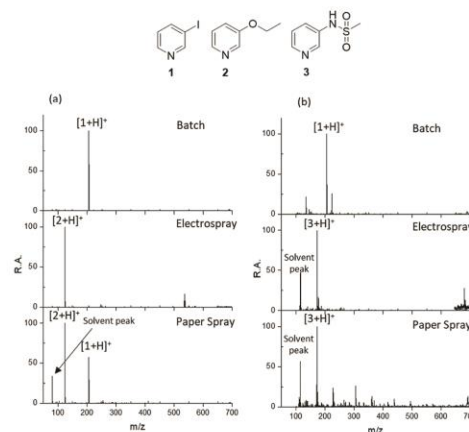


Fig. 2 Mass spectra for C–O coupling (a) and C–N coupling (b) – comparison of bulk/batch mode (2 min), electrospray (2 min) and paper spray (2 min).

trinitrobenzene) to the rinse. The production rate was found to be 55 mg/35 minutes and the yield was a modest 45%. Further multiplexing should improve efficiency.

In addition to ethanol, other reagents were explored for reaction acceleration. The MS conversions (product ion abundances vs. total of products and reagents) of these substrates are reported in Table 1. The trend observed with the different reagents agrees with the trends seen in bulk reactions. Primary alcohols show higher yields when compared to secondary and tertiary alcohols due to steric effects. Hence accelerated reactions using ES can also be used as predictors of successful route in route scouting as a yes/no tool for these types of coupling reactions. This application is one of the more important ways of employing the acceleration effect as previously demonstrated by Wlekinski *et al.*<sup>4</sup>

## C–N coupling

We explored C–N coupling using 3-iodopyridine and various sulfonamides. Online MS using ES (Fig. 1a) shows product

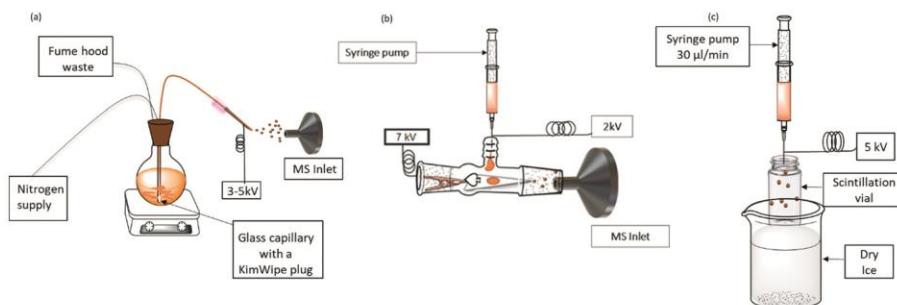


Fig. 1 Apparatus for (a) electrospray, (b) paper spray and (c) scale up (C–O coupling only).

**Table 1** Substrate scope – relative abundance (RA) yields of different substrates used for C–O and C–N coupling using 3-iodopyridine

Alcohol (C–O coupling)	Product ion	R.A. yields <sup>a</sup>	Sulfonamide (C–N coupling)	Product ion	R.A. yields <sup>a</sup>
Ethanol	$[M + H]^+$	100	Methanesulfonamide	$[M + H]^+$	100
1-Hexanol	$[M + H]^+$	96	Ethanesulfonamide	$[M]^+$	63
Cyclohexanol	$[M + H]^+$	17	Cyclopropylsulfonamide	$[M]^+$	50
1-Butanol	$[M + H]^+$	100	<i>t</i> -Butylsulfonamide	$[M]^+$	20
<i>t</i> -Butanol	$[M + H]^+$	0	Benzenesulfonamide	$[M]^+$	66

<sup>a</sup> Relative abundance (RA) yields reported in Table 1 are apparent yields given by the ratio of the mass spectrometry signals for the products relative to the starting materials (also known as the conversion ratio) in the micro droplets relative to the bulk. This is related to but not identical to the ratio of the rate constants for the two media.

formation within the first minute of spraying the reaction mixture (Fig. 2b). Again, the first minute or so is used for spray stabilization and to prime the lines. Product formation was confirmed by performing an MS/MS scan (ESI<sub>1</sub><sup>†</sup> Fig. S3). The ES setup for the reaction was similar to that used in the C–O coupling reactions. Cesium carbonate was initially used as the base for the reaction. However, these spectra were dominated by cesium peaks. Different bases and solvent systems were therefore explored (ESI<sub>1</sub><sup>†</sup> Table S1) and potassium hydroxide was chosen as a suitable base for this reaction since it showed better MS conversion. The best solvent system was tetrahydrofuran: water in a 3 : 1 (v/v) ratio. Reaction acceleration was observed with PS as well, but ES was chosen as the preferred method of scale up for the reasons stated before. The apparatus for the scale up was the same as that used in the ether formation ES experiments. However, for scale up, multiple fused silica lines were used to spray the reaction mixture onto the glass wool which was used as the collection surface. The product was collected, rinsed with deuterated solvent and then confirmed by <sup>1</sup>H NMR (ESI<sub>1</sub><sup>†</sup> Fig. S4). Different reagents were explored for C–N coupling as well. Those studied included sulfonamides such as ethanesulfonamide, cyclopropylsulfonamide, *tert*-butylsulfonamide and benzenesulfonamide. Interestingly, we observed a  $[M + H]^+$  peak with methanesulfonamide, but observed the radical cation  $[M]^+$  in the case of the other sulfonamide substrates. Also interesting was the fact that the ions corresponding to the  $[M]^+$  signals did not undergo fragmentation under any conditions, at high collision energies the ion signal disappeared presumably due to charge exchange. The MS conversions of the different substrates are listed in Table 1. We performed an additional bulk reaction using ethanesulfonamide to verify our findings with reference to the  $[M]^+$  ion. The bulk reaction mixture (at the end of 30 hours) was sprayed using nESI and the high-resolution MS showed the formation of the  $[M]^+$  ion, (ESI<sub>1</sub><sup>†</sup> Fig. S5) thus confirming that the ES generated product is indeed the desired product. These ancillary observations prompted us to explore different pyridines to confirm if the trend existed across *o*-, *m*- and *p*-substituted iodopyridines. Using the ESI setup as described before, we performed the reaction with 2,3 and 4-iodopyridine with methanesulfonamide and ethanesulfonamide. The trend observed is the same as seen with 3-iodopyridine. Methanesulfonamide forms the  $[M + H]^+$  ion while ethanesulfonamide forms the radical cation  $[M]^+$  ion. (ESI<sub>1</sub><sup>†</sup> Fig. S6 and S7).

## Conclusions

In summary, we have demonstrated the acceleration of two air and water sensitive coupling reactions using droplets generated in ES. We have also shown the acceleration of a heterogeneous reaction by modifying the ESI setup to include online filtration. A third finding, confirming earlier data,<sup>4</sup> is that by doing a substrate scope experiment, it is possible to use accelerated reactions as a predictor for bulk reactions. Finally, we have demonstrated scale up to the 10's of mg of representative examples of these reactions. This form of preparative MS is clearly a valuable tool for the synthesis of small quantities of product. Multiplexing these systems should aid in the synthesis of larger quantities of product in a short amount of time.

## Conflicts of interest

There are no conflicts of interest to declare.

## Acknowledgements

This work was supported by AbbVie Inc. and in part upon work supported by the U.S. Department of Energy, Office of Science, Office of Basic Energy Sciences, Separations and Analysis Program, under Award Number DE-FG02-06ER15807.

## Notes and references

- M. Girod, E. Moyano, D. I. Campbell and R. G. Cooks, *Chem. Sci.*, 2011, 2, 501.
- S. M. Paul, D. S. Mytelka, C. T. Dunwiddie, C. C. Persinger, B. H. Munos, S. R. Lindborg and A. L. Schacht, *Nat. Rev. Drug Discovery*, 2010, 9(3), 203–214.
- (a) X. Yan, R. M. Bain and R. G. Cooks, *Angew. Chem., Int. Ed.*, 2016, 55, 12960–12972; (b) X. Yan, H. Cheng and R. N. Zare, *Angew. Chem., Int. Ed.*, 2017, 56, 3562–3565; (c) R. M. Bain, C. J. Pulliam and R. G. Cooks, *Chem. Sci.*, 2015, 6, 397–401; (d) S. Banerjee and R. N. Zare, *Angew. Chem., Int. Ed.*, 2015, 54, 14795–14799.
- (a) M. Wleklinski, C. E. Falcone, B. P. Loren, Z. Jaman, K. Iyer, H. S. Ewan, S. H. Hyun, D. H. Thompson and R. G. Cooks, *Eur. J. Org. Chem.*, 2016, 33, 5480–5484; (b) C. E. Falcone, B. P. Loren, Z. Jaman, M. Wleklinski, D. H. Thompson and R. G. Cooks, *Analyst*, 2017, 142, 2836–2845;

- (c) B. P. Loren, M. Wlekinski, A. Koswara, K. Yammine, Y. Hu, Z. K. Nagy, D. H. Thompson and R. G. Cooks, *Chem. Sci.*, 2017, 8, 4363–4370.
- 5 S. H. Jin, S. S. Lee, B. Lee, S.-G. Jeong, M. Peter and C.-S. Lee, *Anal. Chem.*, 2017, 89, 9722–9729.
- 6 S. Narayan, J. Muldoon, M. G. Finn, V. V. Fokin, H. C. Kolb and K. B. Sharpless, *Angew. Chem., Int. Ed.*, 2005, 44, 3275–3279.
- 7 (a) G. O. Jones, P. Liu, K. N. Houk and S. L. Buchwald, *J. Am. Chem. Soc.*, 2010, 132, 6205–6213; (b) R. Giri and J. F. Hartwig, *J. Am. Chem. Soc.*, 2010, 132, 15860–15863; (c) H.-Z. Yu, Y.-Y. Jiang, Y. Fu and L. Liu, *J. Am. Chem. Soc.*, 2010, 132, 18078–18091; (d) J. W. Tye, Z. Weng, R. Giri and J. F. Hartwig, *Angew. Chem., Int. Ed.*, 2010, 49, 2185–2189; (e) A. J. Hickman and M. S. Sanford, *Nature*, 2012, 484, 177–185.
- 8 (a) S. E. Creutz, K. J. Lotito, G. C. Fu and J. C. Peters, *Science*, 2012, 338, 647–651; (b) J. W. Tye, Z. Weng, A. M. Johns, C. D. Incarvito and J. F. Hartwig, *J. Am. Chem. Soc.*, 2008, 130, 9971–9983.
- 9 (a) S. V. Ley and A. W. Thomas, *Angew. Chem., Int. Ed.*, 2003, 42, 5400–5449; (b) I. P. Beletskaya and A. V. Cheprakov, *Coord. Chem. Rev.*, 2004, 2337–2364; (c) F. Monnier and M. Taillefer, *Angew. Chem., Int. Ed.*, 2009, 48, 6954–6971.
- 10 (a) P. J. Fagan, E. Hauptman, R. Shapiro and A. Casalnuovo, *J. Am. Chem. Soc.*, 2000, 122, 5043–5051; (b) M. Wolter, G. Nordmann, G. E. Job and S. L. Buchwald, *Org. Lett.*, 2002, 4, 973–976; (c) A. Shafir, P. A. Lichtor and S. L. Buchwald, *J. Am. Chem. Soc.*, 2007, 129, 3490–3491; (d) R. A. Altman, A. Shafir, A. Choi, P. A. Lichtor and S. L. Buchwald, *J. Organomet. Chem.*, 2008, 73, 284–286; (e) D. Maiti and S. L. Buchwald, *J. Am. Chem. Soc.*, 2009, 131, 17423–17429.

# Multistep Flow Synthesis of Diazepam Guided by Droplet-Accelerated Reaction Screening with Mechanistic Insights from Rapid Mass Spectrometry Analysis

H. Samuel Ewan,<sup>†</sup> Kiran Iyer,<sup>†</sup> Seok-Hee Hyun, Michael Wlekinski, R. Graham Cooks,\*<sup>‡</sup> and David H. Thompson\*<sup>‡</sup>

Department of Chemistry, Purdue University, West Lafayette, Indiana 47907, United States

**S** Supporting Information

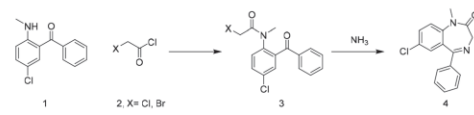
**ABSTRACT:** Electrospray and Leidenfrost droplet accelerated reactions were used as a predictive tool for estimating the outcome of microfluidic synthesis as demonstrated by Wlekinski et al. Rapid analysis by electrospray-mass spectrometry (ESI-MS) also provided immediate feedback on reaction outcomes in flow reactions. Significant reaction acceleration was observed in electrospray relative to the corresponding bulk reaction. This rapid reaction screening and analysis method has allowed for the detection of previously unreported outcomes in the reaction between 5-chloro-2-(methylamino)benzophenone and haloacetyl chloride (halo = Cl or Br) in the continuous synthesis of diazepam. In our current study, a more detailed extension of the previous work, we report acceleration factors that are solvent dependent; additional byproducts that were observed on the microfluidic scale that were absent in the droplet reactions. Gaining insight from this combined droplet and microfluidic screening/rapid ESI-MS analysis approach, we have helped guide the synthesis of diazepam and showcased the potential of this method as a reaction optimization and discovery tool. Informed by these new insights, diazepam was synthesized in a high-yield two-step continuous flow process.

## 1. INTRODUCTION

The potential for the efficient synthesis of active pharmaceutical ingredients (APIs) through continuous flow chemistry continues to draw interest from a broad range of disciplines throughout academia and industry.<sup>1–5</sup> Mass spectrometry (MS) has proven to be a useful tool in reaction monitoring as it allows monitoring of the kinetics and outcome of a reaction.<sup>6</sup> MS also helps in identifying reactive intermediates and hence in understanding the mechanistic details of a chemical reaction.<sup>7</sup> Additionally, MS can be used to study chemical reactions in droplets.<sup>8</sup> Previous studies have shown that most chemical reactions are accelerated in microdroplets formed by electrospray ionization (ESI) relative to the corresponding bulk reactions.<sup>9,10</sup> This acceleration is due, in part, to solvent evaporation and its effect on reagent concentration at the interface.<sup>11</sup> This rapid method of reaction screening can be useful in guiding microfluidic reactions and in scale up. An alternative way of generating microdroplets for studying chemical reactions is by employing the Leidenfrost effect. This effect occurs when a solution is dropped onto a heated surface such as a glass Petri dish which is held at a temperature higher than the boiling point of the solvent used. As the droplet approaches the heated surface, the solvent begins to evaporate, and a layer of insulating vapor is formed around the droplet. This prevents rapid evaporation of the solvent and causes the droplet to levitate.<sup>12</sup> Although the droplets that are formed by this technique are larger than ESI droplets, they have some of the same properties; therefore, reactions in these droplets can also be a useful tool in guiding microfluidic transformations.

In the present study, we use the synthesis of diazepam (Scheme 1) as a model system to showcase how the droplet

**Scheme 1. Proposed Pathway for the Continuous Synthesis of Diazepam**



screening demonstrated by Wlekinski et al.<sup>13</sup> guided the continuous synthesis of diazepam. Since a key step in this pathway involves N-acylation, these observations may have a more general bearing on N-acylation reactions in the synthesis of common bioactive molecules.<sup>14</sup> Although microdroplet conditions do not always directly translate into microfluidic scale conditions, this method can serve as a rapid yes/no prediction tool for the likelihood of a productive microfluidic reaction. Flow chemistry systems, coupled with online monitoring by ESI-MS, enable rapid screening of reaction conditions with real-time feedback. Not only does this allow for facile and efficient synthesis of APIs, but it also brings an opportunity for new insights into reaction pathways and byproduct formation. Diazepam may be obtained in two synthetic steps, starting from the N-acylation reaction of 5-chloro-2-(methylamino)benzophenone **1** with 2-haloacetyl chloride **2** giving amide **3**. Subsequent treatment with ammonia

Received: June 22, 2017

Published: August 22, 2017

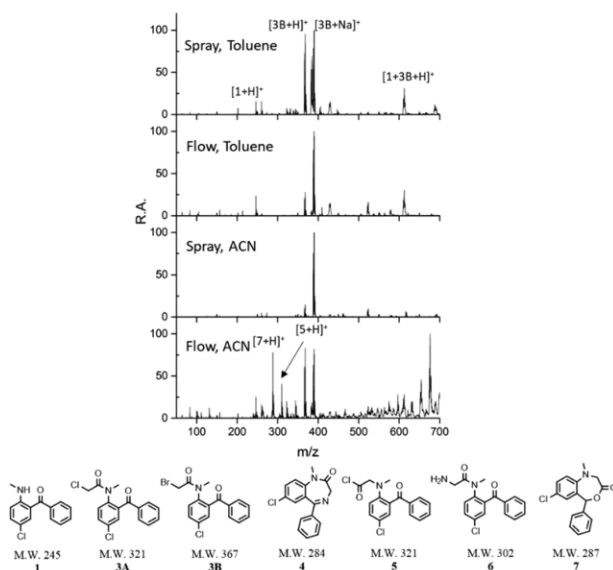


**Figure 1.** N-Acylation screen. Synthesis of **3** in using bromoacetyl chloride—comparison of spray and flow in toluene and acetonitrile.

then results in cyclization, giving diazepam **4** (Scheme 1). For each reaction screened in droplets or examined in flow reaction systems, the outcome was immediately ascertained by ESI-MS analysis.

## 2. RESULTS AND DISCUSSION

**2.1. N-Acylation Reaction Screen.** Reaction screening began with examination of the N-acylation step in ESI droplets, Leidenfrost droplets, bulk, and flow reaction systems. Initial ESI spray (offline) reaction screening across several solvents [dimethylacetamide (DMA), tetrahydrofuran (THF), dimethylformamide (DMF), acetonitrile (ACN), *N*-methylpyrrolidone (NMP), and toluene] revealed significant acceleration in ACN ( $\sim 35\times$ ) and toluene ( $\sim 100\times$ ) relative to a 30 min screen of the reaction in bulk at the same initial concentrations (Figure 1, Figure S1, Table 1). Although the spray experiment was performed in different solvents, the final extraction before analysis was done in ACN for all experiments.

**Table 1.** Accelerations Factors for the N-Acylation Reaction in the Synthesis of Diazepam

solvent	starting material	acceleration factor <sup>a</sup>	
		ESI spray	Leidenfrost
acetonitrile	chloroacetyl chloride	35	25
	bromoacetyl chloride	29	24
toluene	chloroacetyl chloride	97	14
	bromoacetyl chloride	38	34

<sup>a</sup>Acceleration factors reported in Table 1 are apparent acceleration factors given by the ratio of the mass spectrometry signals for the products relative to the starting materials (i.e., the conversion ratio) in the micro droplets relative to the bulk. This is not the same as the ratio of the rate constants for the two media.

The screening of flow reaction conditions for the first step also began with a solvent screen. NMP and DMF performed poorly, giving limited conversion and significant impurities. N-Acylation occurred rapidly and with good conversion in toluene, whereas in ACN, the formation of side products (**5**, **7**) arising from the  $S_N2$  reaction pathway was observed (Figure 1).<sup>13</sup> In addition to solvents, temperatures and residence times were varied (Table S3). With increasing temperature, in most cases, conversion was poorer due to increasingly prevalent side reactions. By exchanging chloroacetyl chloride for bromoacetyl chloride, we obtained evidence of an alternative reaction pathway (previously reported by Wleklinski et al.).<sup>13</sup> The molecular weight of the expected product of this N-acylation reaction using bromoacetyl bromide is 367; however, we saw an additional peak at  $m/z$  322. This corresponds to a loss of bromine rather than chlorine, as expected from N-acylation. A mixture of the  $S_N2$  and N-acylation products (from the flow experiment) was isolated by column chromatography, and though they could not readily be separated from one another, NMR analysis showed two distinct sets of peaks at 3.7 and 3.9 ppm, corresponding to the methylene protons of the N-acylation and  $S_N2$  products, respectively (Figure 2, Figure S2). Guided by these observations regarding the mechanism of the reaction where one solvent favored the more desired pathway and products, we determined that toluene was the optimal solvent for the continuous synthesis of diazepam.

In addition to this  $S_N2$  product, we also observed a peak at  $m/z$  288 in our flow experiments, consistent with ring closure to produce a seven-membered lactone. We propose that this  $m/z$  288 compound (mol. wt. 287) is a result of an initial  $S_N2$  reaction, followed by nucleophilic attack by the carbonyl on the acyl chloride to form the seven-membered ring. <sup>1</sup>H and <sup>13</sup>CNMR analysis confirmed this proposed structure (Figures S3 and S4, respectively). This result suggests that the selection

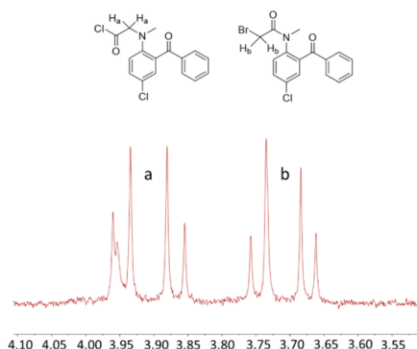


**Figure 2.** Methylene proton  $^1\text{H}$  NMR signals of the  $\text{S}_{\text{N}}2$  and N-acylation product mixture.

of reaction solvent and halide can be used to exert control over the reaction outcome in a microfluidic system. It is noteworthy that these alternative outcomes were observed in the microfluidic experiment but were absent in the corresponding droplet experiments. We believe that this is due to the high temperature and pressure conditions accessible in microfluidic reactions, but absent in droplet reactions, making alternative reaction pathways with higher energy requirements more likely.

**2.2. Cyclization Reaction Screen.** Previous screening of the cyclization reaction space revealed that a greater concentration of ammonia was required to form diazepam in Leidenfrost droplets (Figure 3). Reaction acceleration was observed in these droplet reactions, and they corroborated the

microfluidic screen. A microfluidic screen of the second step from the N-acylation product **3A**, prepared previously, was carried out prior to attempting both steps in continuous flow. The solvent screen was limited by the low solubility of the chloro version of the intermediate (previously prepared in batch). For each solvent, varying temperatures and residence times were screened. The material was insoluble at a target concentration of  $250\ \mu\text{M}$  in ACN and toluene but dissolved well in NMP at this concentration. Fortunately, a good conversion to diazepam was observed in NMP (Table S3). Another interesting observation when studying this step was the appearance of a peak at  $m/z$  303. We anticipated that this might represent a substitution of nitrogen at the methyl position. Due to the appearance of this peak in the MS at lower temperatures and residence times, and disappearance at higher temperatures, we also believed that it might be an intermediate in the diazepam synthesis. LC-MS analysis revealed that, despite the previous MS observation, the quantity of this  $m/z$  303 material remained relatively constant throughout the temperature and residence time screen, even as the quantity of diazepam steadily increased. This could be in part due to high ionization efficiency of the  $m/z$  303 material drowning out the signal from other compounds present in the reaction mixture. This  $m/z$  303 material (**6**) is believed to be a previously reported hydrolysis product of diazepam.<sup>15</sup>

**2.3. Continuous Diazepam Synthesis.** On the basis of these observations, we were able to develop a more complete understanding of the possible outcomes of each synthetic step of our synthetic route to diazepam. These possible reaction pathways are summarized in Scheme 2. Guided by this knowledge from our screening, we next attempted to optimize the synthesis of diazepam in two continuous steps. We used a two-chip reactor system to allow for finer control of

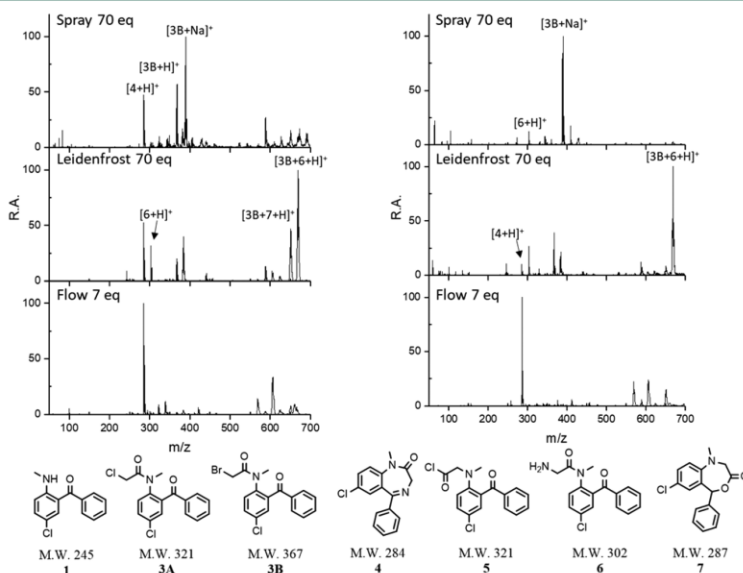
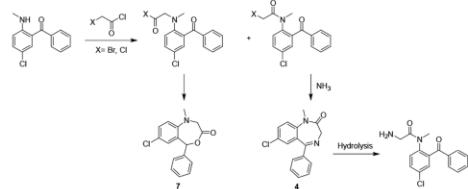


**Figure 3.** Cyclization reaction screen. Synthesis of diazepam, comparing ACN (left) and toluene (right) solvents in spray, Leidenfrost, and flow reactions using bromoacetyl chloride.

**Scheme 2. Reaction Pathway to Diazepam and Its Byproducts Formed during Continuous Flow Reaction**



temperature and residence time in each chip. The first chip combined 5-chloro-2-(methylamino)benzophenone and haloacetyl chloride in a 1:2 ratio, respectively (Figure 4, R1 and R2),

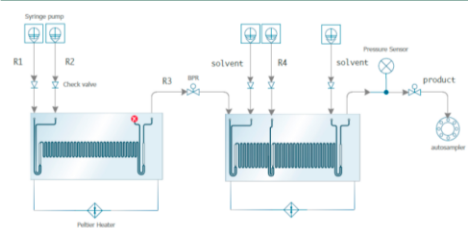


**Figure 4.** Reactor schematic for continuous diazepam synthesis.

before dilution of the resultant N-acylation product mixture (R3) with methanol and subsequent addition of ammonia/methanol (R4) in a 7-fold excess in the second chip.

Solvent screening was again limited by solubility, particularly upon addition of ammonia/methanol in the second step. To alleviate this problem, a dilution step after the first reaction step was incorporated to improve solubility. Good solubility was achieved using toluene for the first step and diluting 1:4 with methanol or NMP. The use of ACN in the first step and for dilution was also effective. As in the previous flow reaction screens, we varied temperature and residence time, as well as the selection of bromo- vs chloroacetyl chloride (Table S4). The results of this screen seemed to corroborate our previous observations, with bromoacetyl chloride resulting in some  $S_N2$  product, particularly in ACN. Furthermore, the overall conversion from the intermediate to diazepam was higher when bromoacetyl chloride was used.

Yields for each reaction were determined using a quantitative ESI-MS/MS method. The optimum result was achieved using bromoacetyl chloride in the toluene/methanol solvent system, which yielded diazepam in 100% yield, based on our ESI-MS quantitation method. This was also the optimal solvent system in Leidenfrost and spray microdroplets (Table S1).

### 3. CONCLUSIONS

This study, using the diazepam synthesis as a model reaction, demonstrates the ability of MS analysis and droplet reactions to guide microfluidic synthesis. MS can be used not only as an analytical tool but can also serve as a quick way to predict reactivity and guide microscale synthesis. The use of spray and Leidenfrost droplet reactions as a screening step to guide the larger scale microfluidic screening proved a useful tool in predicting the overall outcome of a reaction. While some

nuances observed in flow reactions were not observed in droplet experiments, these experiments still consistently provided a yes/no indication of the viability of a reaction. Further, we have demonstrated the continuous synthesis of diazepam in two steps in a microfluidic flow reactor. Our synthesis features the use of a mixed solvent system, as well as two microfluidic chips in sequence, allowing for optimized temperature control at each step. Additionally, we have identified previously unknown reaction pathways. These results showcase the possibility for microfluidic synthesis coupled with rapid ESI-MS analysis to identify previously unknown reaction pathways and optimize continuous synthesis of APIs.

## 4. EXPERIMENTAL SECTION

**4.1. Reagents.** Reagents were purchased from Sigma-Aldrich and used without further purification.

**4.2. NMR Analysis.** NMR samples were prepared by microscale  $SiO_2$  column chromatography. Samples were analyzed using a Bruker AV-III-500-HD NMR spectrometer.

**4.3. Mass Spectrometry.** A mass spectral analysis of reaction products was performed using an LTQ ion trap mass spectrometer (Thermo Fisher Scientific, San Jose, CA) with nanoESI (nESI) ionization. All product samples (spray, Leidenfrost, or flow reactions) were diluted 1:100 into ACN before analysis, unless otherwise noted. The distance between the tip of the spray emitter and ion transfer capillary to the MS was kept constant at ca. 1 mm. Experiments were performed using borosilicate glass pulled to a ca. 1–3  $\mu m$  aperture. A spray voltage of either positive or negative 2.0 kV was used for all analyses. Positive-ion mode was used for all chemical analyses, unless otherwise noted. Product ion (MS/MS) spectra were recorded using collision-induced dissociation (CID) with a normalized collision energy of 25 (manufacturer's unit).

**4.4. Quantitative MS Analysis.** An MS based calibration was made from mixtures of 0,  $1 \times 10^{-7}$ ,  $1 \times 10^{-6}$ ,  $2.5 \times 10^{-6}$ , and  $8 \times 10^{-6}$  M diazepam with  $3.88 \times 10^{-6}$  M diazepam-D3. Each point was measured with nESI in triplicate, and the calibration is based on the diazepam to diazepam-D3 ratio. Crude reaction samples were quantified by first diluting an appropriate amount ( $\times 10\,000$  typically) and then adding the same amount of internal standard. Each crude sample was diluted in duplicate and analyzed by nESI.

**4.5. ESI Experiments.** These experiments were performed by spraying the reaction mixture directly onto glass wool and then extracting the sprayed residue with ACN. The extract was diluted 1:100 then analyzed by MS. A home-built electrospray ionization source was used. Reagents 1 and 2 were premixed at concentrations of 100 mM and 200 mM, respectively, and loaded into a syringe. Offline spray was carried out at a flow rate of 10  $\mu L/min$ , 100 psi  $N_2$  sheath gas, and 5 kV voltage. The total spray time was 10 min. After MS analysis, the washed material was drawn back into the syringe and mixed with ammonia in methanol and then electrosprayed to synthesize diazepam.

**4.6. Leidenfrost Droplet Experiments.** This experiment was carried out on a hot plate with a heat setting of 540  $^{\circ}C$  (although the droplet temperature was much lower). Reagents 1 and 2 were premixed and loaded into a Pasteur pipet. The reaction mixture was then dropped onto a glass Petri dish that was placed on the hot plate. The reaction mixture was added in aliquots over a time period of about 2 min. After 2 min, the mixture was collected from the surface using a Pasteur pipet and then analyzed by MS after diluting 1:2.

**4.7. Microfluidic Experiments.** All microfluidic reactions were carried out using a Chemtrix Labtrix S1 system, equipped with 3223 or 3224 reactor chips.

**4.8. *N*-(2-Benzoyl-4-chlorophenyl)-2-halo-*N*-methylacetamide (3).** Solutions (100 mM) of 5-halo-2-(methylamino)benzophenone (1 equiv) and of haloacetyl chloride (1 equiv) in toluene, ACN, DMF, or NMP were prepared. In the DMF reaction screen, 500 mM solutions were used; in the NMP reaction screens, 250 mM solutions of benzophenone and 500 mM (2 equiv) chloroacetyl chloride were used. A syringe was loaded with each of these two solutions and positioned on the first two inlets of a 10  $\mu$ L Labtrix 3223 chip. A third syringe was loaded with toluene and positioned on the third port of the same chip as a diluent. The reaction was flowed with 30, 60, and 180 s residence times at temperatures of 50, 100, and 150 °C. Samples were collected and immediately analyzed by ESI-MS (1  $\mu$ L of each sample was diluted with 99  $\mu$ L of ACN, then loaded into a glass electrospray tip for analysis). Samples were saved and stored at -20 °C.

**4.9. Diazepam (4) from *N*-(2-Benzoyl-4-chlorophenyl)-2-chloro-*N*-methylacetamide (3A).** A 250 mM solution of *N*-(2-benzoyl-4-chlorophenyl)-2-chloro-*N*-methylacetamide (1 equiv) was prepared. Syringes were loaded with the prepared solution and with 7 N ammonia in methanol (7 equiv) and positioned on the first two inlets of a 10  $\mu$ L Labtrix 3223 chip. A third syringe was loaded with NMP and positioned on the third port of the same chip as a diluent. The reaction was flowed with 30, 60, and 180 s residence times at temperatures of 50, 100, and 150 °C. Samples were collected and immediately analyzed by ESI-MS (1  $\mu$ L of each sample was diluted with 99  $\mu$ L of ACN, then loaded into a glass electrospray tip for analysis). Samples were saved and stored at -20 °C.

**4.10. Diazepam (4) from 5-Halo-2-(methylamino)-benzophenone (1).** Solutions (100 mM) of 5-halo-2-(methylamino)benzophenone (1 equiv) and 200 mM haloacetyl chloride (2 equiv) in toluene or ACN were prepared. Syringes were loaded with the prepared solutions and with 7 N ammonia in methanol (7 equiv). The syringes containing 5-halo-2-(methylamino)-benzophenone and haloacetyl chloride were positioned on the first two inlets of a 10  $\mu$ L Labtrix 3223 chip. The mixture was flowed into a second 15  $\mu$ L Labtrix 3224 chip through the first inlet. A syringe containing toluene, NMP, or ACN was positioned at the second inlet of the 3224 chip to dilute the reaction by 1:4. The syringe containing 7 N ammonia in methanol was positioned at the third inlet of the 3224 chip. A final syringe containing toluene, NMP, or ACN was positioned at the final inlet of the 3224 chip, flowing at a low flow rate of solvent to help avoid fouling at the outlet. The reaction was flowed with residence times of 1 + 0.32 s and 2 + 0.62 s (chip 1 + chip 2) and temperatures of 75 °C in chip 1 and 100, 110, 120, or 140 °C in the second chip. Samples were collected and immediately analyzed by ESI-MS (1  $\mu$ L of each sample was diluted with 99  $\mu$ L of ACN, then loaded into a glass electrospray tip for analysis). Samples were saved and stored at -20 °C.

**4.11. Batch Synthesis of *N*-(2-Benzoyl-4-chlorophenyl)-2-chloro-*N*-methylacetamide (3A).** Chloroacetyl chloride (0.39 mL, 4.9 mmol, 1 EQ) was added to a solution of 5-chloro-2-(methylamino)benzophenone (1.2 g, 4.9 mmol) in 100 mL NMP (50 mM). The reaction was heated to 90 °C for 40 min. The solution was then concentrated in vacuo, and the

product was isolated via SiO<sub>2</sub> column chromatography in 68% yield. The structure was confirmed by <sup>1</sup>H NMR (Figure S5).

## ■ ASSOCIATED CONTENT

### Supporting Information

The Supporting Information is available free of charge on the ACS Publications website at DOI: 10.1021/acs.oprd.7b00218.

Structure index, Figures S1–S5, Tables S1–S4 (PDF)

## ■ AUTHOR INFORMATION

### Corresponding Authors

\*E-mail: davethom@purdue.edu.

\*E-mail: cooks@purdue.edu.

### ORCID

R. Graham Cooks: 0000-0002-9581-9603

David H. Thompson: 0000-0002-0746-1526

### Author Contributions

<sup>†</sup>H.S.E. and K.I. contributed equally.

### Notes

The authors declare no competing financial interest.

## ■ ACKNOWLEDGMENTS

This work was supported by the Defense Advanced Projects Agency of the United States of America and the National Science Foundation (CHE-1307264).

## ■ REFERENCES

- (1) Adamo, A.; Beingsner, R. L.; Behnam, M.; Chen, J.; Jamison, T. F.; Jensen, K. F.; Monbaliu, J. M.; Myerson, A. S.; Revalor, E. M.; Snead, D. R.; Stelzer, T.; Weeranoppanant, N.; Wong, S. Y.; Zhang, P. *Science* **2016**, *352* (6281), 61–67.
- (2) Bédard, A.; Longstreet, A. R.; Britton, J.; Wang, Y.; Moriguchi, H.; Hicklin, R. W.; Green, W. H.; Jamison, T. F. *Bioorg. Med. Chem.* **2017**, *10.1016/j.bmc.2017.02.002*.
- (3) Baumann, M.; Baxendale, I. R. *Beilstein J. Org. Chem.* **2015**, *11*, 1194–1219.
- (4) Malet-Sanz, L.; Susanne, F. *J. Med. Chem.* **2012**, *55*, 4062–4098.
- (5) McQuade, D. T.; Seeburger, P. H. *J. Org. Chem.* **2013**, *78*, 6384–6389.
- (6) Chen, P. *Angew. Chem., Int. Ed.* **2003**, *42*, 2832–2847.
- (7) Santos, L. S.; Rosso, G. B.; Pilli, R. A.; Eberlin, M. N. *J. Org. Chem.* **2007**, *72*, 5809–5812.
- (8) Huang, G.; Li, G.; Ducan, J.; Ouyang, Z.; Cooks, R. G. *Angew. Chem., Int. Ed.* **2011**, *50*, 2503–2506.
- (9) Banerjee, S.; Zare, R. N. *Angew. Chem., Int. Ed.* **2015**, *54*, 14795–14799.
- (10) Yan, X.; Bain, R. M.; Cooks, R. G. *Angew. Chem., Int. Ed.* **2016**, *55*, 12960.
- (11) Bain, R. M.; Pulliam, C. J.; Cooks, R. G. *Chem. Sci.* **2015**, *6*, 397–401.
- (12) Bain, R. M.; Pulliam, C. J.; Thery, F.; Cooks, R. G. *Angew. Chem., Int. Ed.* **2016**, *55*, 10478–10482.
- (13) Wlekinski, M.; Falcone, C. E.; Loren, B. P.; Jaman, Z.; Iyer, K.; Ewan, H. S.; Hyun, S. H.; Thompson, D. T.; Cooks, R. G. *Eur. J. Org. Chem.* **2016**, *33*, 5480–5484.
- (14) Roughley, S. D.; Jordan, A. M. *J. Med. Chem.* **2011**, *54*, 3451–3479.
- (15) Maslanka, A.; Krzek, J.; Szlosarczyk, M.; Zmudzki, P.; Wach, K. *Int. J. Pharm.* **2013**, *455*, 104–112.

## Mass Spectrometry

# Can Accelerated Reactions in Droplets Guide Chemistry at Scale?

Michael Wlekinski,<sup>[a]</sup> Caitlin E. Falcone,<sup>[a]</sup> Bradley P. Loren,<sup>[a]</sup> Zinia Jaman,<sup>[a]</sup> Kiran Iyer,<sup>[a]</sup> H. Samuel Ewan,<sup>[a]</sup> Seok-Hee Hyun,<sup>[a]</sup> David H. Thompson,<sup>\*,[a]</sup> and R. Graham Cooks<sup>\*,[a]</sup>

**Abstract:** Mass spectrometry (MS) is used to monitor chemical reactions in droplets. In almost all cases, such reactions are accelerated relative to the corresponding reactions in bulk, even after correction for concentration effects, and they serve to predict the likely success of scaled-up reactions performed in microfluidic systems. The particular chemical targets used in these test studies are diazepam, atropine and diphenhydramine. In addition to a yes/no prediction of whether scaled-up reaction is possible, in some cases valuable information was obtained that helped in optimization of reaction con-

ditions, minimization of by-products, and choice of catalyst. In a variant on the spray-based charged droplet experiment, the Leidenfrost effect was used to generate larger, uncharged droplets and the same reactions were studied in this medium. These reactions were also accelerated but to smaller extents than in microdroplets, and they gave results that correspond even more closely to microfluidics data. The fact that MS was also used for online reaction monitoring in the microfluidic systems further enhances the potential role of MS in exploratory organic synthesis.

## Introduction

This study is part of a larger project, the overall goal of which is to develop an automated scalable and continuous synthesis system. A key objective is to test possible synthetic pathways quickly on a small scale seeking a go/no-go result. We “spot-test” particular routes using a chemical pruning step, which employs reaction acceleration in droplets with independent mass spectrometric analysis. A simple yes/no answer to product or (in multistep reactions) intermediate formation is sought using the charged droplet reactor. We use electrospray (ESI) for both synthesis and analysis with careful control of parameters to avoid unwanted reaction during analysis.<sup>[1]</sup>

Charged microdroplets are produced by ESI. It is known that reaction rates increase as the solvent evaporates because of changes in concentration, pH, surface/volume ratios, and interfacial effects.<sup>[1b,1c,2]</sup> The acceleration factors can be remarkably large.<sup>[3]</sup> A recent review covers the topic of accelerated reactions in droplets, including evidence that partial solvation of reagents at interfaces contributes to the orders of magnitude reaction rate acceleration that can be seen.<sup>[1a]</sup> The hypothesis investigated here is that the accelerated reactions that occur in droplets might assist in rapidly evaluating reactivity in microfluidic systems.

A second method of producing droplets is based on the Leidenfrost effect.<sup>[4]</sup> It has recently been shown that accelerated

organic reactions occur in Leidenfrost droplets.<sup>[5]</sup> These droplets differ from ESI-based droplets in that they are (i) larger, (ii) net-neutral, and (iii) involve elevated temperatures. The difference in droplet size means that larger amounts of reagent can be studied, but the surface/volume ratio is greatly decreased. The measured reaction acceleration factors for three previously studied Leidenfrost reactions, hydrazone formation, Katritzky pyrylium → pyridinium conversion and Claisen–Schmidt condensation, are about an order of magnitude.<sup>[5]</sup>

Note that we do not expect to be able to transfer optimized conditions exactly from the droplet scale to the microfluidics scale, in part because of uncertainty about the origins of acceleration effects in the two systems. We do expect that these optimized conditions will represent a starting point for efficient optimization of the conditions in the microfluidics reactor. We also expect that information on reaction intermediates and mechanisms might be acquired from the study of droplet reactions. This information is already being obtained in experiments in which the degree of desolvation of the initial droplets is varied by changing the distance that the droplets travel before analysis.<sup>[1b]</sup> Information obtained from the droplet reactor on experimental parameters including solvent, catalyst, pH, etc. is also readily acquired, and we examine how transferable this information is in optimizing the microfluidics reactor.

The identification of suitable pathways to target molecules is just one step towards an online, automated flow-through synthesizer, for which the groundwork has been laid by several groups. Notable are the mol-scale, end-to-end, continuous manufacturing pilot plant developed by MIT/Novartis,<sup>[6]</sup> the refrigerator-sized, reconfigurable, on-demand synthesizer of pharmaceuticals of MIT,<sup>[7]</sup> the nanomol-scale robotic high-throughput synthesizer of Merck,<sup>[8]</sup> and the automated synthesis labo-

[a] Department of Chemistry, Purdue University  
560 Oval Drive, West Lafayette, IN 47907, USA  
E-mail: davethom@purdue.edu  
cooks@purdue.edu  
http://aston.chem.purdue.edu

Supporting information and ORCID(s) from the author(s) for this article are available on the WWW under <http://dx.doi.org/10.1002/ejoc.201601270>.

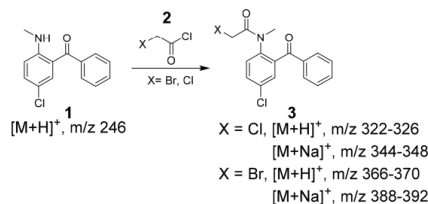
ratory of Eli Lilly.<sup>[9]</sup> The mol-scale MIT synthesizer was used to produce aliskiren hemifumarate in tablet form, from a complex intermediate in a continuous fashion.<sup>[6]</sup> The Merck nanomol system was used to screen 1500 reactions per day to identify potential candidate reactions for large-scale syntheses. The Lilly system combined automated synthesis with analysis performed remotely controlled in real-time, to produce products on a gram-scale.

The main question underlying this study is whether droplet reactions may be used to predict chemical reactivity in flow chemistry systems, in particular in microfluidics. The mechanism for acceleration observed in microdroplets is certainly different from that in microfluidics in that evaporation is not significant in microfluidics; however, interfacial effects may still play an important role, especially in droplet microfluidics.<sup>[10]</sup> The speed of data acquisition in droplets makes this approach attractive. Note that false negatives (predict no reaction, but reaction can be observed) is not expected to be a serious problem, because there are usually many available routes to test. On the other hand, a false positive result will lead to wasted effort in seeking an analogous flow reaction. Note, too, that use of droplets for a simple yes/no regarding occurrence of reaction represents only one level of enquiry, even though it is the most important one. As will be seen in the results now to be discussed, information on reaction conditions is also obtained, although the quality of this information remains to be evaluated further by studying more cases.

## Results and Discussion

The charged-droplet- and microfluidic-based synthesis of amide **3**, generated by *N*-acylation of **1** with the 2-haloacetyl chloride **2**, was examined due to its importance as a synthetic step in the pathway to diazepam (Scheme 1). An electrospray droplet reactor was used to evaluate potential solvents for the *N*-acylation reaction using chloroacetyl chloride. Offline charged-droplet reactions were performed using a mixture of **1** and **2** (X = Cl) in various solvents, and conversion to product as analyzed by ESI MS was compared to a 30 min batch reaction (Figure S1). Before analysis, samples are quenched in order to ensure no further reaction by diluting the collected product into the solvent used in the prior step. The results indicate that there is significant acceleration of the reaction when the solvent is DMF, ACN, or toluene. Acceleration in microdroplets is associated with evaporation and is proposed to be due, in part, to intrinsic rate acceleration at the interface.<sup>[2c]</sup> These initial results encouraged a more extensive reaction screening, where the effect of the chosen 2-haloacetyl chloride (Cl or Br) and the solvent (ACN, toluene) was investigated using a droplet reactor. Interestingly, the droplet reactor data indicated nearly complete conversion of starting materials to product for both the chloro and bromo starting materials in acetonitrile (Figure 1) and in toluene (Figure S2). Starting material **1** is observed at  $m/z = 246$ , and product **3** appears in either its protonated (X = Cl:  $m/z = 322-326$ ; X = Br:  $m/z = 366-370$ ) or sodiated (X = Cl:  $m/z = 344-348$ ; X = Br:  $m/z = 388-392$ ) form. A small amount of  $S_N2$  product ( $m/z = 322$ ) was observed for bromoacetyl chlor-

ide in ACN but not in toluene. In the case of the chloro starting material (**2**), the  $S_N2$  and acylation products have identical molecular formulae and are not differentiable; however, the presence of only small amounts of the  $S_N2$  product using the bromo starting material, provides evidence that the chloro compound reacts mainly to form the desired acylation product.



Scheme 1. Reaction of **1** and **2** (X = Cl, Br) to form amide **3**.

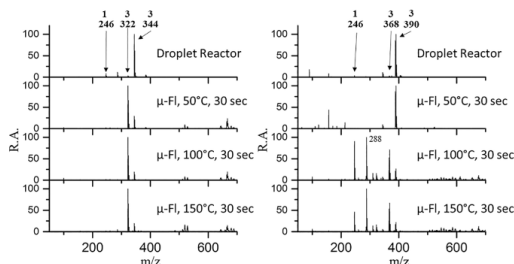


Figure 1. Synthesis of **3** in ACN using (a) chloroacetyl chloride and (b) bromoacetyl chloride in a droplet reactor and in microfluidics ( $\mu$ -Fl).

Flow experiments were performed using the same concentrations as in the droplet reactor while screening the effect of temperature for a fixed residence time of 30 s. High conversion to **3** was observed with chloroacetyl chloride in both solvents at 50 °C. More interestingly, a major difference was observed with bromoacetyl chloride in ACN, wherein a major amount of  $S_N2$  reaction product was observed, especially at higher temperatures (100 and 150 °C). The presence of a by-product (ion  $m/z = 288$ ) arising from the initial  $S_N2$  reaction product was confirmed by NMR spectroscopy and MS/MS (data not shown). The droplet reactor predicted formation of the desired intermediate, which was observed in flow. However, under higher-temperature conditions in flow, the proportion of  $S_N2$  product increased. This difference can be explained by the fact that evaporative cooling occurs during flight in the droplet reaction at room temperature, thus reducing the reaction temperature.<sup>[11]</sup> Nonetheless, the droplet reaction demonstrated reaction feasibility and showed that specific solvents (ACN, toluene) are better than others, a fact reiterated under microfluidic conditions for this transformation.

The ability of droplet reactivity to guide chemistry at scale was investigated for another important drug, diphenhydramine. The flow-based synthesis of diphenhydramine was demonstrated by the reaction of 2-(dimethylamino)ethanol (DMAE) with chlorodiphenylmethane.<sup>[12]</sup> This synthesis featured 100 % atom economy; however, chlorodiphenylmethane is an expen-

sive starting material, which motivated an effort to develop a more cost-effective process by replacing chlorodiphenylmethane using a commodity starting material, benzhydrol (**4**). To synthesize diphenhydramine (**5**), benzhydrol (**4**) was converted into the corresponding mesyl ester, which was subsequently treated with DMAE to produce **5** (Scheme 2). The droplet-reactor synthesis of **5** was demonstrated by performing two sequential charged-droplet reactions in either a toluene or acetonitrile solvent system. First benzhydrol and mesyl chloride were sprayed to produce the mesyl ester. This material was recovered and redissolved before introduction of the second reagent, DMAE (20 equiv.) and repetition of the spray process (Figure 2). The MS analysis of the two-step spray product indicated that ACN is overall a better solvent for the synthesis of diphenhydramine, (**5**) ( $m/z = 256$ ) than toluene. Unreacted DMAE ( $m/z = 90$ ), mesylated DMAE ( $m/z = 168$ ), and a dimer of DMAE with methanesulfonic acid ( $m/z = 275$ ) were observed with the charged microdroplets. A similar trend was observed in flow (Figures S3 and S4), where optimized conditions gave diphen-



Scheme 2. Mesylation of **4** followed by reaction with 2-(dimethylamino)-ethanol (DMAE) to form diphenhydramine (**5**).

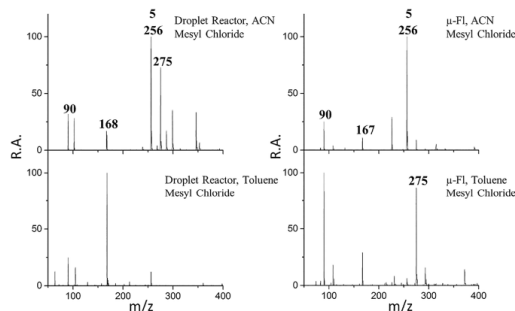
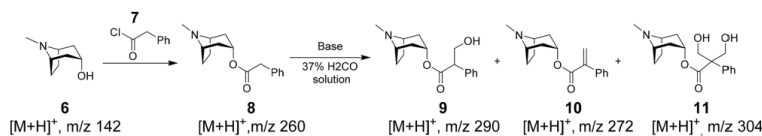


Figure 2. Charged-microdroplet (a, c) and microfluidic (b, d) reaction telescoping for the diphenhydramine synthesis in two solvents (ACN, toluene).



Scheme 3. Esterification reaction of **6** with **7** to synthesize **8** followed by base-catalyzed aldol condensation with formaldehyde to synthesize atropine (**9**).

hydramine in 35 % and <1 % yield in ACN and toluene, respectively, using 1 equiv. of 2-(dimethylamino)ethanol. Good agreement is observed between the charged droplet reactor and flow in this synthesis.

The charged-droplet and microfluidic synthesis of atropine also was achieved by telescoping two reaction steps. The intermediate ester **8** (Scheme 3) was prepared from the commercially available starting materials tropine (**6**) and phenylacetyl chloride (**7**). The intermediate **8** was used without further purification for the aldol condensation reaction to produce the final product, atropine. The first step was optimized for solvent and reactant stoichiometry. The droplet reactor indicated *N,N*-dimethylacetamide (DMA) as the best solvent, and this was confirmed in microfluidics (data not shown). Using the unpurified intermediate ester **8** ( $m/z = 260$ ), a base screen with the droplet reactor determined the effectiveness of three bases in synthesizing atropine (**9**) ( $m/z = 290$ ). Each base was successful in the droplet reactor, producing significant amounts of atropine (and byproducts), with 1,5-diazabicyclo[4.3.0]dec-5-ene being the most effective (Figure 3 and Figure S5). In flow, each base produced atropine (and byproducts) with 1,5-diazabicyclo[4.3.0]dec-5-ene again being the most efficient. There is also some agreement between flow and charged droplets on the type and extent of byproduct formation. For example, using 1,5-diazabicyclo[4.3.0]dec-5-ene, atropine and its dehydration product **10** ( $m/z = 272$ ) are observed. However, with MeOK the same type of byproducts could be observed, but their proportions were quite different (Scheme 3). The major byproduct in flow, **11** (characterized by  $m/z = 304$ ) is barely formed in charged droplets. One possible reason for this difference is that formaldehyde with its high vapor pressure escapes the droplets rapidly obviating formation of this byproduct. Finally, good agreement between the two methods was observed with NaOH, where the  $\alpha,\beta$ -unsaturated product **10** ( $m/z = 272$ ) is the major byproduct for both droplet reactor and microfluidics. Thus, for the synthesis of atropine, the charged-droplet reactor was useful in guiding the choice of solvent and base.

The occurrence of accelerated organic reactions in Leidenfrost droplets<sup>[5]</sup> is at least in part a surface property (partial solvation of reagent molecules at the surface reduces activation energies). Consistent with this and the smaller surface/volume ratios of Leidenfrost droplets, acceleration factors are smaller than in electrosprayed microdroplets. However, the larger droplets (0.5 mL volume) mean that conditions in the Leidenfrost droplets are closer to those in microfluidic solutions and in bulk, so the predictive power of Leidenfrost droplet reactions might be even greater than that of electrospray-generated droplets.

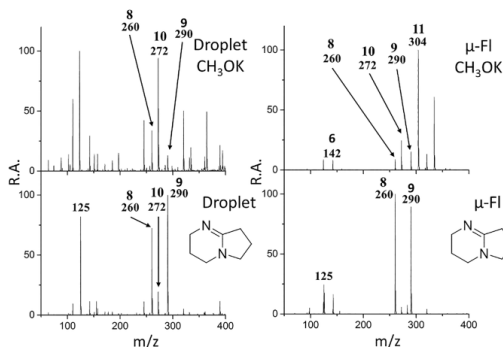


Figure 3. Charged-microdroplet (a, c) and microfluidic (b, d) reaction telescoping for the atropine synthesis using potassium methoxide or 1,5-diazabicyclo[4.3.0]dec-5-ene.

The lack of a formal charge also strengthens the expected analogy with scaled-up chemistry.

This expectation is met when one considers data for the first step of the diazepam synthesis using bromoacetyl chloride and chloroacetyl chloride. First, consider the mass spectra recorded for charged droplets in ACN and in toluene vs. those for Leidenfrost droplets in the same two solvents (Figure 4 and Figure S6). The assignment of  $m/z$  values is the same as in Figure 1 and Scheme 1. The conversion in the Leidenfrost experiment is not as great (more starting material seen) as in the charged-droplet reactions, but both methods give almost exclusively the desired acylation intermediate as opposed to the  $S_N2$  product. There is not a large difference in the results for ACN vs. toluene as solvent, except that the conversion is slightly higher in ACN. If we now consider the difference between microfluidic flow and Leidenfrost droplet data, we find remarkable similarities. Microfluidic synthesis at 50 °C results primarily in the desired acylation product as is the case in the Leidenfrost droplets. One difference is in the formation of a minor species seen at  $m/z = 260$  in the Leidenfrost case.

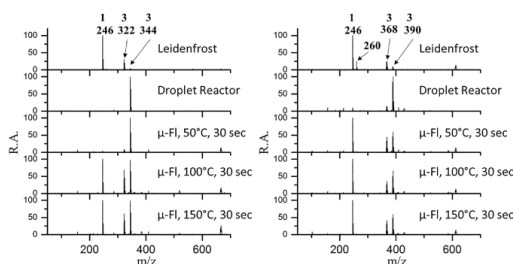


Figure 4. Synthesis of **3** (in two forms) in toluene using chloroacetyl chloride (a) and bromoacetyl chloride (b) in Leidenfrost, charged-microdroplets and microfluidics.

The ion  $m/z = 260$  is believed to be due to a ring-closure product resulting from acylation. The uncharged Leidenfrost droplets closely mirror the chemistry in microfluidics, except when the temperature in the microfluidics reaction is greatly

elevated. Under these circumstances different byproducts are generated as  $S_N2$  becomes more competitive.

The complete synthesis of diazepam in Leidenfrost droplets was demonstrated by adding 7 or 70 equiv. of  $NH_3$  to intermediate **3** (not isolated) in a telescoped reaction. The chloro intermediate was unable to produce diazepam in quantity. However, the bromo intermediate produced diazepam (confirmed by MS/MS) in agreement with a reported flow synthesis.<sup>[7]</sup>

## Conclusions

This study provides evidence for the importance of MS, not only in the traditional sense as an analytical method, but as a fast, predictive means to perform small-scale continuous synthesis. The data encourage the use of spray ionization as a method of screening for successful reaction pathways in flow reactions. At a secondary level, we find some parallels in the favored catalysts, solvents, mol ratios of reagents, and other operating conditions. However, little is known of droplet reaction mechanisms (an important topic in its own right), so extrapolation from conditions that favor reactions in nanodroplets to microfluidic chemistry may not be simple or universal. Nevertheless, as we show in this study, a useful guide to the global aspects of flow chemistry is obtained in these cases.

Limitations in further extending this approach to reaction screening (and to online reaction monitoring) are to be found in the size, cost and complexity of commercial mass spectrometers, many of the features of which are unnecessary for this type of study. What is needed for the purposes described here is a small, portable, unit-resolution, low mass/charge range (to  $m/z = 1000$ ) instrument, which has ambient ionization and tandem mass spectrometry capabilities. A recent review of miniature MS instruments<sup>[13]</sup> describes a few systems of this type.

## Experimental Section

**Droplet-Reactor Experiments:** These experiments used electrospray ionization (ESI) by spraying the reaction mixture either directly into the MS (Figure 5a) or onto a collection surface (Figure 5b) before taking up the residue in solvent and performing ESI-MS product analysis. Figure 5 illustrates these two options, which are distinguished by the fact that (a) is virtually instantaneous (10–15 s), while (b) can take a few minutes, but (b) is more versatile in that

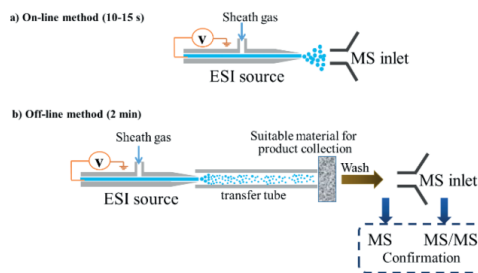


Figure 5. Methods used to perform microdroplet reactions, based on ESI either (a) with online product analysis by MS or (b) with sprayed droplet deposition and subsequent offline MS product analysis.

the reaction and analysis occur in separate steps, more product is formed, and the procedure allows temperature and other conditions to be varied and optimized. In both cases, the primary question being asked is whether the desired reaction occurs or not. Products, byproducts and residual reagents were identified from mass spectra recorded at unit resolution, while tandem mass spectrometry (MS/MS) was used to confirm identifications.

**Offline-Droplet Reactor:** Offline-droplet experiments were performed using a homebuilt electrospray ionization source. In the cases of atropine and diazepam, the reagents were premixed and subjected to offline electrospray at 10  $\mu\text{L}/\text{min}$  with +5 kV voltage and 100 psi  $\text{N}_2$ . For diphenhydramine, reagents were mixed inline using a mixing tee and offline electrospray was performed under the same conditions. After the electrospray deposition was complete, the reaction product was rinsed from the collection surface and then analyzed by nanoESI. Samples were diluted at least 100-fold before analysis in order to quench the reaction and ensure no further reaction could occur during the analysis step. For two-step reactions, the washed material was drawn back into a syringe and mixed with the second-step reagent and then electrosprayed, collected, and washed as before.

**Leidenfrost-Droplet Experiments:** Reactions in Leidenfrost droplets<sup>[5]</sup> differ in that these are (i) larger, (ii) net-neutral, and (iii) involve elevated temperatures. Reaction mixtures were added in aliquots over a 2 min period to maintain a constant droplet volume (Figure S7). The droplet (ca. 2 mm diameter) was levitated in a petri dish atop a heater with a surface temperature of 400–500 °C (CARE). Reactions occurred at temperatures close to, but below, the boiling point of the solvent.<sup>[14]</sup>

**Mass Spectrometry:** Mass spectral analysis of reaction products was performed using an LTQ ion trap mass spectrometer (Thermo Fisher Scientific, San Jose, CA) with nanoESI ionization. All product samples (spray, Leidenfrost, or flow reactions) were diluted 1:100 into acetonitrile before analysis, unless otherwise noted. The distance between the tip of the spray emitter and ion transfer capillary to the MS was kept constant at ca. 1 mm. Experiments were performed using borosilicate glass pulled to a ca. 1–3  $\mu\text{m}$  aperture. A spray voltage of either positive or negative 2.0 kV was used for all analyses. Positive-ion mode was used for all chemical analyses, unless otherwise noted. Product ion (MS/MS) spectra were recorded using collision-induced dissociation (CID) with a normalized collision energy of 25 (manufacturer's unit).

**Synthesis of Diazepam Precursor:** Reactions were performed with 100 mM 5-chloro-2-(methylamino)benzophenone and 100 mM 2-haloacetyl chloride (halo = Cl, Br) dissolved in either toluene or acetonitrile. Solutions were either mixed prior to use (droplet reactor, Leidenfrost) or mixed online (microfluidics) to give a final reaction concentration of 50 mM. Other conditions were explored as indicated in the results section.

**Diphenhydramine:** Reactions were performed in a two-step manner. First, 500 mM benzhydrol was mixed with 500 mM mesyl chloride, then in the second step 20 equiv. of 2-(dimethylamino)ethanol was used in the droplet reactor, while 1 equiv. was used for microfluidics. Other conditions were explored as indicated in the Results section.

**Atropine:** The atropine intermediate was first synthesized by allowing 1 M phenylacetyl chloride to react with 1 M atropine dissolved in DMA. For the second step, 7 equiv. of base in DMA and 7 equiv. of formaldehyde in  $\text{H}_2\text{O}$  were used. Other conditions were explored as indicated in the Results section.

**Microfluidics:** Microfluidic reactions were performed using a Labtrix S1 system from Chemtrix, Ltd. The Labtrix S1 system is comprised of syringe pumps to deliver reagents, microfluidic chips, a Peltier element, back-pressure regulator, and a collection carousel. For the synthesis of diphenhydramine a homebuilt Peltier-controlled system coupled with the Chemtrix microfluidic platform was used to allow for multi-step reactions to be performed with control over the temperature of each step.

**Chemicals and Reagents:** All chemicals were purchased from Sigma Aldrich and used without further purification.

## Acknowledgments

Support is acknowledged from the Department of Defense: Defense Advanced Research Projects Agency (award no. W911NF-16-2-0020).

**Keywords:** Kinetics · Mass spectrometry · Reaction acceleration · Flow chemistry · Leidenfrost effect

- a) X. Yan, R. M. Bain, R. G. Cooks, *Angew. Chem. Int. Ed.* **2016**, *55*, 12960–12972; *Angew. Chem.* **2016**, *128*, 13152–13156; b) R. M. Bain, C. J. Pulliam, R. G. Cooks, *Chem. Sci.* **2015**, *6*, 397–401; c) R. M. Bain, C. J. Pulliam, S. T. Ayrton, K. Bain, R. G. Cooks, *Rapid Commun. Mass Spectrom.* **2016**, *30*, 1875–1878.
- a) J. K. Lee, S. Kim, H. G. Nam, R. N. Zare, *Proc. Natl. Acad. Sci. USA* **2015**, *112*, 3898–3903; b) R. M. Bain, C. J. Pulliam, S. A. Raab, R. G. Cooks, *J. Chem. Educ.* **2016**, *93*, 340–344; c) Y. Li, X. Yan, R. G. Cooks, *Angew. Chem. Int. Ed.* **2016**, *55*, 3433–3437; *Angew. Chem.* **2016**, *128*, 3494.
- S. Banerjee, R. N. Zare, *Angew. Chem. Int. Ed.* **2015**, *54*, 14795–14799; *Angew. Chem.* **2015**, *127*, 15008.
- C. Josserand, S. T. Thoroddsen, *Annual Rev. Fluid Mechanics* **2016**, *48*, 365–391.
- R. M. Bain, C. J. Pulliam, F. Thery, R. G. Cooks, *Angew. Chem. Int. Ed.* **2016**, *55*, 10478–10482; *Angew. Chem.* **2016**, *128*, 10634–10638.
- S. Mascia, P. L. Heider, H. Zhang, R. Lakerveld, B. Benyahia, P. I. Barton, R. D. Braatz, C. L. Cooney, J. M. B. Evans, T. F. Jamison, K. F. Jensen, A. S. Myerson, B. L. Trout, *Angew. Chem. Int. Ed.* **2013**, *52*, 12359–12363; *Angew. Chem.* **2013**, *125*, 12585.
- A. Adamo, R. L. Beingsner, M. Behnam, J. Chen, T. F. Jamison, K. F. Jensen, J.-C. M. Monbaliu, A. S. Myerson, E. M. Revalor, D. R. Snead, T. Stelzer, N. Weeranoppanant, S. Y. Wong, P. Zhang, *Science* **2016**, *352*, 61–67.
- A. Buitrago Santanilla, E. L. Regalado, T. Pereira, M. Shevlin, K. Bateman, L.-C. Campeau, J. Schneeweis, S. Berritt, Z.-C. Shi, P. Nantermet, Y. Liu, R. Helmy, C. J. Welch, P. Vachal, I. W. Davies, T. Cernak, S. D. Dreher, *Science* **2015**, *347*, 49–53.
- A. G. Godfrey, T. Masquelin, H. Hemmerle, *Drug Discovery Today* **2013**, *18*, 795–802.
- a) H. Song, D. L. Chen, R. F. Ismagilov, *Angew. Chem. Int. Ed.* **2006**, *45*, 7336–7356; *Angew. Chem.* **2006**, *118*, 7494; b) K. Jähnisch, V. Hessel, H. Löwe, M. Baerns, *Angew. Chem. Int. Ed.* **2004**, *43*, 406–446; *Angew. Chem.* **2004**, *116*, 410.
- S. C. Gibson, C. S. Feigerle, K. D. Cook, *Anal. Chem.* **2014**, *86*, 464–472.
- D. R. Snead, T. F. Jamison, *Chem. Sci.* **2013**, *4*, 2822–2827.
- D. T. Snyder, C. J. Pulliam, Z. Ouyang, R. G. Cooks, *Anal. Chem.* **2016**, *88*, 2–29.
- R. Abdelaziz, D. Disci-Zayed, M. K. Hedayati, J.-H. Pöhls, A. U. Zillohu, B. Erkartal, V. S. K. Chakravadhanula, V. Duppel, L. Kienle, M. Elbahri, *Nat. Commun.* **2013**, *4*, 2400.

Received: October 10, 2016  
Published Online: November 3, 2016